

ENERGY TRANSFER AND EXCITON DYNAMICS
IN PHOTOSYNTHETIC PIGMENT-PROTEIN COMPLEXES

by

ADAM KELL

B.S., Truman State University, 2010

AN ABSTRACT OF A DISSERTATION

submitted in partial fulfillment of the requirements for the degree

DOCTOR OF PHILOSOPHY

Department of Chemistry
College of Arts and Sciences

KANSAS STATE UNIVERSITY
Manhattan, Kansas

2016

Abstract

The structure-function relationships of natural pigment-protein complexes are of great interest, as the electronic properties of the pigments are tuned by the protein environment to achieve high quantum yields and photon utilization. Determination of electronic structure and exciton dynamics in protein complexes is complicated by static disorder and uncertainties in the properties of system-bath coupling. The latter is described by the phonon profile (or spectral density), whose shape can only be reliably measured experimentally for the lowest energy state. Low-temperature, laser-based spectroscopies are applied towards model pigment-protein complexes, i.e., the Fenna-Matthews-Olson (FMO) and water-soluble chlorophyll-binding (WSCP) complexes, in order to study system-bath coupling and energy transfer pathways. Site-selective techniques, e.g., hole burning (HB) and fluorescence line narrowing, are utilized to overcome static disorder and reveal details on homogeneous broadening. In addition, excitonic calculations with non-Markovian lineshapes provide information on electronic structure and exciton dynamics. A new lognormal functional form of the spectral density is recommended which appropriately defines electron-phonon parameters, i.e., Huang-Rhys factor and reorganization energy. Absorbance and fluorescence spectral shifts and HB spectra reveal that samples of FMO may contain a subpopulation of destabilized proteins with modified HB efficiencies. Simulations of spectra corresponding to intact proteins indicate that the entire trimer has to be taken into account in order to properly describe fluorescence and HB spectra. The redshifted fluorescence spectrum of WSCP is described by uncorrelated energy transfer as opposed to previous models of excited state protein relaxation. Also, based on nonconservative HB spectra measured for WSCP, a mechanism of electron transfer between chlorophylls and aromatic amino acids is proposed.

ENERGY TRANSFER AND EXCITON DYNAMICS
IN PHOTOSYNTHETIC PIGMENT-PROTEIN COMPLEXES

by

ADAM KELL

B.S., Truman State University, 2010

A DISSERTATION

submitted in partial fulfillment of the requirements for the degree

DOCTOR OF PHILOSOPHY

Department of Chemistry
College of Arts and Sciences

KANSAS STATE UNIVERSITY
Manhattan, Kansas

2016

Approved by:

Major Professor
Ryszard Jankowiak

Copyright

ADAM KELL

2016

Abstract

The structure-function relationships of natural pigment-protein complexes are of great interest, as the electronic properties of the pigments are tuned by the protein environment to achieve high quantum yields and photon utilization. Determination of electronic structure and exciton dynamics in protein complexes is complicated by static disorder and uncertainties in the properties of system-bath coupling. The latter is described by the phonon profile (or spectral density), whose shape can only be reliably measured experimentally for the lowest energy state. Low-temperature, laser-based spectroscopies are applied towards model pigment-protein complexes, i.e., the Fenna-Matthews-Olson (FMO) and water-soluble chlorophyll-binding (WSCP) complexes, in order to study system-bath coupling and energy transfer pathways. Site-selective techniques, e.g., hole burning (HB) and fluorescence line narrowing, are utilized to overcome static disorder and reveal details on homogeneous broadening. In addition, excitonic calculations with non-Markovian lineshapes provide information on electronic structure and exciton dynamics. A new lognormal functional form of the spectral density is recommended which appropriately defines electron-phonon parameters, i.e., Huang-Rhys factor and reorganization energy. Absorbance and fluorescence spectral shifts and HB spectra reveal that samples of FMO may contain a subpopulation of destabilized proteins with modified HB efficiencies. Simulations of spectra corresponding to intact proteins indicate that the entire trimer has to be taken into account in order to properly describe fluorescence and HB spectra. The redshifted fluorescence spectrum of WSCP is described by uncorrelated energy transfer as opposed to previous models of excited state protein relaxation. Also, based on nonconservative HB spectra measured for WSCP, a mechanism of electron transfer between chlorophylls and aromatic amino acids is proposed.

Table of Contents

List of Figures	ix
List of Tables	xii
List of Abbreviations	xiii
Acknowledgements	xiv
Dedication	xv
Preface	xvi
Chapter 1 – Introduction	1
1.1. Photosynthesis	1
1.1.1. Photosystem of Green Sulfur Bacteria	2
1.1.2. The Water-Soluble Chlorophyll-Binding Protein of Higher Plants	4
1.2. Exciton Theory and Excitation Energy Transfer	6
1.2.1. Frenkel Excitons	7
1.2.2. Electron-Phonon Coupling	9
1.2.3. Redfield and Förster Theories	11
1.3. Laser-Based Spectroscopies	15
1.3.1. Dynamic and Static Disorder	16
1.3.2. Hole Burning and Fluorescence Line Narrowing	18
1.4. Organization of Dissertation	24
Chapter 2 – On the Shape of the Phonon Spectral Density in Photosynthetic Complexes	26
2.1. Introduction	28
2.2. Results and Discussion	31
2.2.1. Gaussian-Lorentzian	31
2.2.2. B777	31
2.2.3. Brownian Oscillator	33
2.2.4 Ohmic	34
2.2.5. Lognormal	34
2.2.6. Application to Photosynthetic Antenna Complexes	35
2.3. Concluding Remarks	42

Chapter 3 – On Destabilization of the Fenna-Matthews-Olson Complex of <i>Chlorobaculum tepidum</i>	45
3.1. Introduction.....	47
3.2. Materials and Methods.....	48
3.3. Results and Discussion	49
3.3.1. Absorption and Hole Burned Spectra	49
3.3.2. Reorganization and Site Energies	56
3.4. Conclusions.....	59
Chapter 4 – On the Controversial Nature of the 825 nm Exciton Band in the FMO Protein Complex.....	61
4.1. Introduction.....	63
4.2. Results and Discussion	65
4.3. Conclusions.....	75
Chapter 5 – Effect of Spectral Density Shapes on the Excitonic Structure and Dynamics of the Fenna-Matthews-Olson Trimer from <i>Chlorobaculum tepidum</i>	77
5.1. Introduction.....	79
5.2. Theory	80
5.3. Results and Discussion	82
5.4. Conclusions.....	92
Chapter 6 – New Insight into the Water-Soluble Chlorophyll-Binding Protein from <i>Lepidium virginicum</i>	94
6.1. Introduction.....	96
6.2. Materials and Methods.....	99
6.3. Results.....	101
6.3.1. Room- and Low-Temperature Optical Spectra.....	101
6.3.2. Nonresonant and Resonant Hole-Burned Spectra.....	103
6.3.3. On the Nature of Nonresonant Holes.....	105
6.4. Discussion.....	107
6.4.1. Interdimer Uncorrelated Excitation Energy Transfer	107
6.4.2. Electron Exchange	110
6.5. Concluding Remarks.....	113

Chapter 7 – Conclusions	115
References	118
Appendix A – Supporting Information for “On the Shape of the Phonon Spectral Density in Photosynthetic Complexes”	140
A.1. Definitions.....	140
A.2. Often Used Spectral Densities	141
Appendix B – Supporting Information for “Effect of Spectral Density Shapes on the Excitonic Structure and Dynamics of the Fenna-Matthews-Olson Trimer from <i>Chlorobaculum</i> <i>tepidum</i> ”	144
B.1. Qualitative Fits to Literature Data.....	144
B.2. Different Models of Static and Dynamic Disorder	146
B.3. Simulations of Optical Spectra Using Several Literature Hamiltonians.....	149
Appendix C – Supporting Information for “New Insight into the Water-Soluble Chlorophyll- Binding Protein from <i>Lepidium virginicum</i> ”	158

List of Figures

Figure 1.1 Model of excitation energy and electron transfer in photosynthesis	1
Figure 1.2 Schematic structural model for the photosystem of GSB	3
Figure 1.3 FMO X-ray structure	4
Figure 1.4 LvWSCP X-ray structure	6
Figure 1.5 Energy level diagrams and single-site fluorescence spectra for weak and strong el-ph coupling	10
Figure 1.6 Schematic representation of static disorder	17
Figure 1.7 Diagram of experimental setup for low-temperature absorption and HB measurements	20
Figure 1.8 Energy level diagram illustrating the phonon-assisted tunneling mechanism of NPHB	21
Figure 1.9 Representative preburn, postburn and HB spectra for an inhomogeneously broadened absorption band	23
Figure 2.1 Experimental FMO Δ FLN spectrum and single-site spectra calculated with G-L, lognormal, B777, OBO and Ohmic functions	36
Figure 2.2 Experimental FMO Δ FLN spectrum, and single-site spectra calculated with lognormal and modified B777 functions	37
Figure 2.3 $J(\omega)$ curves obtained using the G-L, lognormal and B777 functions for CP29. Experimental CP29 Δ FLN spectrum, and single-site spectra calculated with lognormal and B777 functions	38
Figure 2.4 Experimental Chl <i>a</i> - and Chl <i>b</i> -WSCP Δ FLN spectra and single-site spectra calculated with lognormal and B777 functions	39
Figure 2.5 Ohmic-type functions compared to FMO lognormal function	40
Figure 2.6 Ohmic and OBO functions compared to FMO lognormal function	41
Figure 3.1 Absorption, emission and nonresonant HB spectra for two FMO samples and comparison of 825 nm absorption band positions of various samples	50
Figure 3.2 Absorption and fluence-dependent, nonresonant HB spectra for two FMO samples ..	53
Figure 3.3 Percent hole-depth plotted as a function of fluence for various FMO samples	54

Figure 3.4 Deconvolution of FMO absorption and nonresonant HB spectra into contributions from intact and destabilized complexes.....	55
Figure 3.5 Absorption and emission spectra for two FMO samples displaying a conserved Stokes shift	56
Figure 3.6 Experimental FMO Δ FLN spectrum and single-site spectra calculated with lognormal spectral density	58
Figure 4.1 Structure of the FMO trimer showing the orientation of BChl <i>a</i> pigments, and resonant hole-burned spectra burned into the 825 nm absorption band	65
Figure 4.2 Experimental FMO absorption, emission and nonresonant HB spectra compared to Redfield simulations for a monomer and trimer.....	69
Figure 4.3 Contributions of BChl <i>a</i> 3 and 4 to absorption and nonresonant hole-burned spectra.....	73
Figure 4.4 Distributions of Förster transfer times for pigments contributing to sub-bands 2 and 3	75
Figure 5.1 5 K experimental and simulated absorption, emission and nonresonant HB spectra for the FMO trimer	83
Figure 5.2 Calculated BChl <i>a</i> spectral contributions to absorption.....	87
Figure 5.3 Absorption of neutral and oxidized FMO	88
Figure 5.4 Time-dependent exciton occupation probabilities.....	90
Figure 5.5 Experimental and simulated temperature-dependent FMO absorption.....	91
Figure 5.6 Energy levels of BChl <i>a</i> sites and exciton states compared to the 5 K fluorescence spectrum of the chlorosome–baseplate system.....	92
Figure 6.1 Overall structure and geometry of Chl dimers of the tetrameric LvWSCP	97
Figure 6.2 Room-temperature absorption spectra of LvWSCP and CaWSCP.....	102
Figure 6.3 Room- and low-temperature optical spectra of LvWSCP.....	103
Figure 6.4 Nonresonant HB spectra and ZPH action spectrum.....	104
Figure 6.5 Resonant HB spectra	105
Figure 6.6 UV region absorption and HB spectra, and orientations of aromatic amino acids in Chl binding pocket.....	107
Figure 6.7 Modeled low-energy absorption and fluorescence spectra for LvWSCP assuming uncorrelated EET between Chl dimers	110

Figure 6.8 Modeled absorption, and persistent and transient HB spectra assuming a mechanism of electron exchange	112
Figure B.1 6 K experimental and simulated T-S, CD and LD spectra for the FMO trimer.....	145
Figure B.2 20 K experimental and simulated DADS for the FMO trimer	146
Figure B.3 Simulated 5 K optical spectra and occupation probabilities of the FMO trimer assuming site-dependent static disorder	147
Figure B.4 Simulated 5 K optical spectra and temperature-dependent absorption of the FMO trimer assuming site-dependent S	148
Figure B.5 5 K spectra simulated with a Modified Redfield/Förster theory Hamiltonian	151
Figure B.6 5 K spectra simulated with a Redfield theory Hamiltonian.....	154
Figure B.7 5 K spectra simulated with a Hamiltonian determined from 3DES measurements...	155

List of Tables

Table 2.1 Lognormal distribution parameters used to fit Δ FLN spectra for Chl <i>a</i> - and Chl <i>b</i> -CaWSCP	39
Table 4.1 Hamiltonian for reduced structural model of FMO from <i>C. tepidum</i>	68
Table 5.1 Frenkel Hamiltonian for the FMO trimer in the site representation	85
Table 5.2 Contribution numbers from a simultaneous fit of optical spectra	86
Table 5.3 Rate constant matrix	89
Table A.1 General expressions for different curve characteristics for both $J(\tilde{\nu})$ and $C''(\tilde{\nu})$ of spectral density functions	143
Table B.1 Hamiltonian for the FMO monomer from simple exciton theory	150
Table B.2 Hamiltonian for the FMO monomer from modified Redfield/Förster theory.....	150
Table B.3 Hamiltonian for the FMO trimer from Redfield theory	153
Table B.4 Hamiltonian for the FMO monomer from 3DES	155
Table B.5 Comparison of FMO site energies from various Hamiltonians	156
Table B.6 Comparison of experimental and calculated exciton energies for the FMO monomer and trimer.....	157
Table C.1 Gene sequence of LvWSCP in vector used for overexpression and synthetic gene sequence.....	158

List of Abbreviations

2DES	two-dimensional electronic spectroscopy	HB	hole burning
3DES	three-dimensional electronic spectroscopy	LvWSCP	<i>Lepidium virginicum</i> water-soluble chlorophyll protein
BChl	bacteriochlorophyll	NPHB	nonphotochemical hole burning
CaWSCP	cauliflower water-soluble chlorophyll protein	OBO	overdamped Brownian oscillator
Chl	chlorophyll	PHB	photochemical hole burning
CS	charge separation	PSB	phonon sideband
CT	charge transfer	PSBH	phonon sideband hole
DADS	decay associated difference spectra	PSI	Photosystem I
ΔFLN	difference fluorescence line narrowing	PSII	Photosystem II
EET	excitation energy transfer	RC	reaction center
el-ph	electron-phonon	SDF	site distribution function
ET	electron transfer	T-S	triplet minus singlet
FLN	fluorescence line narrowing	TrEsp	transitions from electrostatic potentials
FMO	Fenna-Matthews-Olson	Trp	tryptophan
FWHM	full-width at half-maximum	WSCP	water-soluble chlorophyll protein
G-L	Gaussian-Lorentzian	ZPH	zero-phonon hole
GSB	green sulfur bacteria	ZPL	zero-phonon line

Acknowledgements

First and foremost I am indebted to my advisor Prof. Ryszard Jankowiak. His guidance and support provided many wonderful opportunities and experiences during my graduate studies. I am also very grateful that he and Majka were such gracious hosts over the years, always providing interesting and engaging conversations anytime we visited their home.

I must thank members of my Graduate Committee, Profs. Viktor Chikan, Daniel Higgins, Robert Szoszkiewicz and Michal Zolkiewski for their valuable time and input. Special thanks is given to Prof. Caterina Scoglio as the Committee Chairperson.

For many lessons on experimentation, especially working with the lasers, I thank former group members Drs. Khem Acharya, Jinhai Chen, Ximao Feng, Chen Lin and Bhanu Neupane. Their patience and understanding is greatly appreciated. Thanks to current group members Mahboobe Jassas and Kevin Robben for being great to work with.

There are many members of the Chemistry Department who I would like to acknowledge: Prof. Eric Mattaa for constant encouragement and support; the ladies in the office for answering questions and organizing department functions; Earline Dikeman and Michael Hinton for valuable feedback and guidance in teaching undergraduate labs; Tobe Eggers, Jim Hodgson, Ron Jackson, and Dr. Leila Maurmann not just for technical support but also friendly encouragement and conversations over the years.

Finally, support from all my family will never be forgotten, especially my wife Kylie for her amazing attitude while taking care of both a fifth-year graduate student and a newborn son.

Dedication

To Kylie and Daniel

Preface

The research presented in this dissertation was performed in the Department of Chemistry, Kansas State University (KSU), from May 2011 to May 2016. Chapters 3–5 were collaboration between KSU and Washington University in St. Louis (St. Louis, MO) and Chapter 6 with the Weizmann Institute of Science (Rehovot, Israel)/Migal–Galilee Research Institute (Kiryat Shmona, Israel), where both institutions provided samples for the experimental measurements.

Chapter 1

Introduction

1.1. Photosynthesis

Photosynthesis is a vital process for life in which solar energy is converted into chemical potential through the synthesis of ATP and NADPH.¹ Photosynthesis occurs in plants, bacteria and algae within photosystems which consist of membrane-bound pigment-protein complexes working in concert.¹⁻³ The main steps of photosynthesis are:¹ (1) light harvesting and energy transfer; (2) electron transfer (ET); (3) charge separation (CS); and (4) product synthesis. The first step occurs in light-harvesting (or antenna) complexes while reaction centers (RCs) are responsible for steps 2 and 3. After absorption of a photon, the large network of antenna complexes work to efficiently direct excitation energy towards the RC; as depicted pictorially in Figure 1.1.

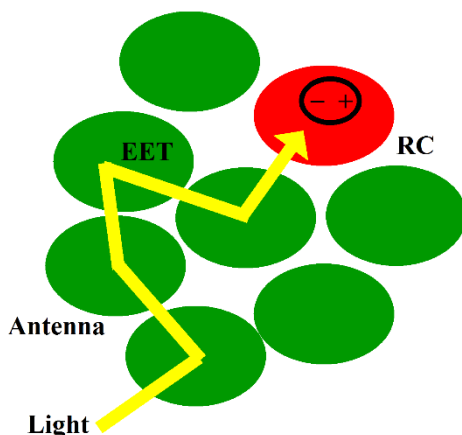


Figure 1.1 Model of excitation energy and ET processes occurring in a hypothetical photosystem. Green represents antenna complexes while red indicates a RC, where CS occurs (depicted by the + and - charges). The yellow line corresponds to the EET pathway followed after the initial photon absorption.

Higher plants, cyanobacteria and algae perform photosynthesis under aerobic (oxygenic) conditions, where water is the reductant.^{1,4-6} After absorption of a photon by Photosystem II (PSII), water is split into molecular oxygen and protons; the latter is used to create a pH gradient across the membrane.⁵ The pH gradient drives protons through ATP synthase, reducing ADP to form ATP.¹ A second, concerted, step occurs when Photosystem I (PSI) absorbs a photon which drives the reduction of NADP⁺ to NADPH.⁶ PSI and PSII contain type-I and type-II RCs, respectively, distinguishing between the molecules used as terminal electron acceptors. That is, type-I RCs contain iron-sulfur clusters^{6,7} while type-II utilize quinone molecules.⁵

Interestingly, long-lived chlorophyll (Chl) excited states (i.e., the triplet state, ³Chl) can photosensitize highly-reactive singlet oxygen, leading to degradation.⁸ Singlet oxygen production is more prevalent under high light intensity. Various mechanisms of photoprotection exist with so-called nonphotochemical quenching among the most widely-studied.⁹ In contrast to aerobic photosynthesis, anaerobic photosynthetic bacteria¹⁰ utilize other reducing agents other than water as electron sources, such as hydrogen sulfide.¹ Examples include green sulfur bacteria (GSB) and purple bacteria, which contain type-I and type-II RCs, respectively. GSB can be found in oxygen-free, low-light environments, which are rich in sulfur, such as the Black Sea¹¹ or volcanic vents.¹²

1.1.1. Photosystem of Green Sulfur Bacteria

GSB contain a unique photosystem that varies from plants, algae and other types of bacteria. Figure 1.2 shows the structural organization of the photosystem of GSB. The main light-harvesting component is the large chlorosome,¹³⁻¹⁶ which can contain hundreds of thousands of pigments.^{13,17} While there is an extensive number of chlorosome membrane proteins,^{14,18-20} the optical properties of chlorosomes are dominated by pigment-pigment interactions^{21,22} with only the CsmA protein binding bacteriochlorophyll (BChl) molecules.^{23,24} A paracrystalline layer of

BChl *a*-CsmA (the so-called baseplate)^{25,26} resides at the bottom of the chlorosome and transfers energy between the chlorosome and water-soluble Fenna-Matthews-Olson (FMO) protein.²⁷⁻²⁹ FMO connects the chlorosome to the cytoplasmic membrane-bound RC (type-I)^{30,31} and facilitates excitation energy transfer (EET) to the RC from the light-harvesting chlorosome.

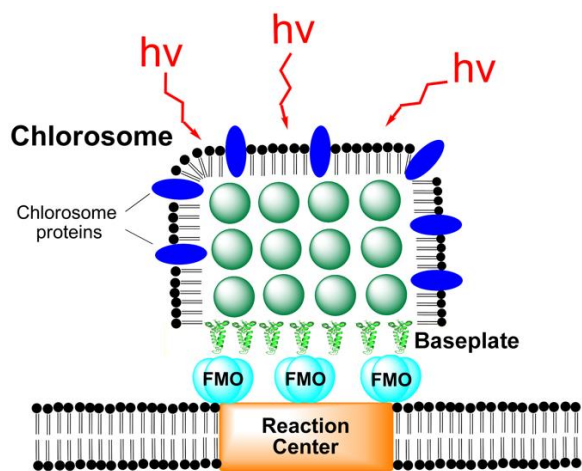


Figure 1.2 Schematic structural model for the photosystem of GSB.^{26,32}

FMO was the first pigment-protein complex to have the X-ray structure solved³³ and since then has continued to be a well-studied complex.²⁹ X-ray structures are available for several species of GSB: *Prosthecochloris (Pr.) aestuarii*,³³⁻³⁵ *Chlorobaculum (C.) tepidum*³⁵⁻³⁷ and *Pelodictyon (Pl.) phaeum*.^{38,39} Figure 1.3 shows the X-ray structure of FMO from *Pr. aestuarii* (PDB ID: 3EOJ).³⁵ The structure of FMO is homologous among GSB and consists of a homotrimer (C₃-symmetry) binding BChl *a* inside a series of β sheets. While the initial findings determined seven BChl *a* per protein monomer, an eighth BChl *a* at the monomer interface was resolved from the structure of a FMO sample crystallized while isolating the RC.³⁷ Since then BChl *a* 8 has been identified by both X-ray crystallography^{35,38,39} and mass spectrometry data⁴⁰ (although with varying occupancy).

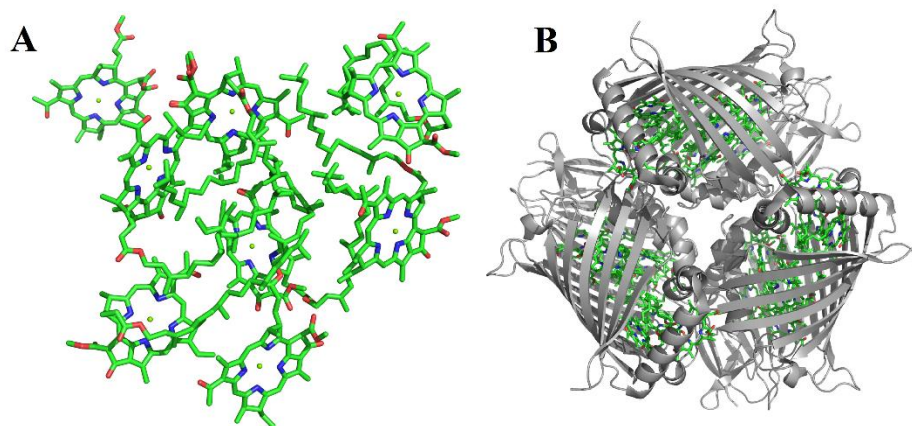


Figure 1.3 FMO X-ray structure.³⁵ Frame A: arrangement of BChl *a* pigments within a monomer (side view). Frame B: FMO trimer with the protein (grey) in cartoon representation (top view).

Due to its relatively small size compared to other light harvesting complexes and well-characterized structure, FMO has been well-studied as a model system for structure-based simulations of optical spectra and exciton dynamics.^{29,41} This interest is increased by the presence of quantum beats observed in pump-probe spectra at low temperature⁴² and coherent cross peak oscillations in two-dimensional maps at low⁴³ and room⁴⁴ temperatures. As photosynthetic antenna complexes display very efficient EET, it has been suggested that quantum effects (like those observed in FMO) play an important role in achieving high quantum efficiency.^{43,45}

1.1.2. The Water-Soluble Chlorophyll-Binding Protein of Higher Plants

Water-soluble Chl-binding proteins (WSCP) are small (~20 kDa) proteins⁴⁶ found in higher plants that preferentially oligomerize to tetramers.^{47,48} WSCP has been isolated from *Chenopodium album*,⁴⁹ *Brassica*,⁵⁰ *Raphanus*,^{51–53} and *Lepidium virginicum*.^{54–56} WSCPs are classified according to photophysical and Chl binding properties. Class I proteins exhibit photoconversion of their absorption spectrum upon illumination with visible light while class II proteins do not.⁴⁶ In general, the function of WSCPs in vivo is not known; however, it has been suggested that class II WSCPs can act as a Chl (or Chl degradation product) carrier,^{57,58} display trypsin inhibitor activity⁵⁹ (i.e.,

contain the Kunitz trypsin inhibitor motif), provide temporary Chl storage and shielding from molecular oxygen,⁶⁰ or even participate in herbivore resistance.⁶¹

Additionally, class II WSCPs are divided into subclasses of proteins with a higher Chl *a/b* binding ratio than total leaf extract (class IIa) and a lower Chl *a/b* binding ratio than total leaf extract (class IIb).^{62,63} The only known class IIb complex is from *Lepidium virginicum* (LvWSCP). Most commonly studied are the class IIa WSCPs from *Brassicaceae* plants, such as cauliflower (CaWSCP).^{46,64} While various WSCPs have been crystallized,^{47,48,51,54,65,66} the only structures determined by X-ray crystallography are for LvWSCP⁴⁷ (see Figure 1.4) and, very recently, CaWSCP.⁶⁷ While it has been proposed in the literature that class IIb WSCPs bind fewer than four Chls per protein tetramer;^{57,68,69} recent spectroscopic evidence points towards a uniform one-to-one binding ratio between Chls and protein monomer,^{70,71} consistent with the crystal structure of LvWSCP.⁴⁷ Thus, Chls bound by class II WSCPs are arranged as two open sandwich dimers related by pseudo C₂-symmetry.⁴⁷ The small complex size and known structure make WSCP, like FMO, an ideal model system for the studying of exciton interactions and energy transfer.

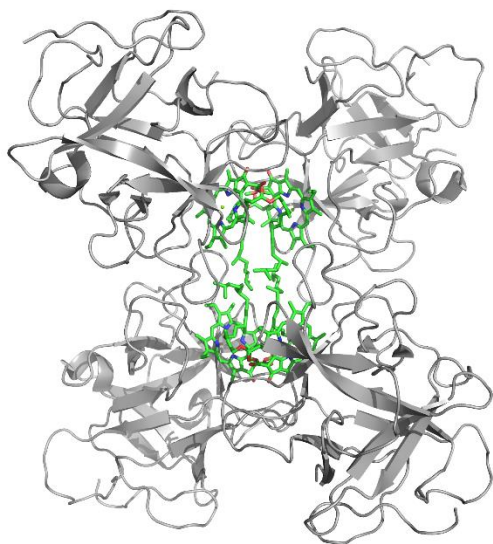


Figure 1.4 LvWSCP X-ray structure.⁴⁷ Chl *a* in green with protein (grey) in cartoon representation.

1.2. Exciton Theory and Excitation Energy Transfer

When photons are absorbed by a molecular aggregate (e.g., closely spaced Chls within a protein matrix) the resulting excitation creates an electron-hole pair, which can be delocalized over several sites.^{72,73} Such an electron-hole pair is a quasiparticle termed an exciton.⁷⁴ Various excitons can be described based upon the electron-hole distance: Wannier-Mott, charge transfer (CT) and Frenkel (zero-radius) excitons.^{41,75} Wannier-Mott excitons have a large electron-hole separation compared to the constituent size and are often found in crystals with covalent or ionic bonding present,^{73,76} while CT excitons are important for photosynthetic RCs.^{77,78} Generally for light harvesting antennas only Frenkel (zero-radius) excitons are considered, as the interactions between molecules are weak and no chemical reactions or ET are assumed to occur upon excitation.^{41,75} However, it has been suggested that in the light harvesting complexes of purple bacteria, self-trapped excitons are required to explain the redshifted fluorescence spectra.⁷⁹⁻⁸¹ Such trapping can occur due to deformations of the surrounding matrix.⁷⁵

1.2.1. Frenkel Excitons

Given a molecular aggregate with weak intermolecular interactions, composite wave functions can be constructed from unperturbed monomer wave functions (Heitler-London approximation);^{41,73,82}

$$|0\rangle = \prod_m \psi_m^0 \quad (1.1a)$$

$$|m\rangle = \psi_m^1 \prod_{n \neq m} \psi_n^0 \quad (1.1b)$$

where eqs 1.1a–b represent the ground and single-exciton states, respectively. That is, $|m\rangle$ represents the state of the aggregate when molecule m is in its excited electronic state and all other molecules are in the ground state.^{41,75} While important for time-resolved optical spectroscopy due to large pulse powers, double-exciton states (and higher orders) will not be considered in the following sections.

In the site basis, the Frenkel Hamiltonian can be expressed as

$$\hat{H}_S = \sum_{m,n} \varepsilon_m \hat{A}_m^\dagger \hat{A}_m + V_{mn} \hat{A}_m^\dagger \hat{A}_n \quad (1.2)$$

where \hat{A}_m^\dagger and \hat{A}_m are the creation and annihilation operators for an excited electronic state localized on site m , ε_m is the vertical transition energy of site m (site energy), and V_{mn} is the interaction potential between sites m and n . Diagonalization of eq 1.2 produces a set of stationary single-exciton states which are eigenvectors of the Frenkel Hamiltonian.^{74,75,82}

$$\hat{H}_S |M\rangle = E_M |M\rangle \quad (1.3a)$$

$$|M\rangle = \sum_m c_{mM} |m\rangle \quad (1.3b)$$

with E_M the eigenvalue (vertical transition energy) corresponding to state M and c_{mM} the eigenvector coefficient of site m to state M . More physically meaningful are the occupation numbers given by $|c_{mM}|^2$, which give the contribution of site m to state M .^{74,82} As the exciton states are linear combinations of local states in the site basis, likewise, the state transition dipoles are linear combinations of the site dipoles:

$$\vec{\mu}_M = \sum_m c_{mM} \vec{\mu}_m \quad (1.4)$$

Note that the dipole strength of a transition can be determined spectroscopically as^{83,84}

$$|\vec{\mu}|^2 = \frac{3hcn}{8\pi^3} \int_{\Delta\tilde{\nu}} \frac{\sigma(\tilde{\nu})}{\tilde{\nu}} d\tilde{\nu} \quad (1.5)$$

with $\Delta\tilde{\nu}$ running over the wavenumber range of the transition and $\sigma(\tilde{\nu})$ corresponding to the absorption cross section (cm^2).

The electronic potential term V in eq 1.2 is dominated by electrostatic interactions,⁴¹ which for two molecules m and n is described by

$$V_{mn} = \frac{1}{hc} \int_{-\infty}^{\infty} \int_{-\infty}^{\infty} \frac{\rho_m(\vec{r}_1) \rho_n(\vec{r}_2)}{|\vec{r}_1 - \vec{r}_2|} d\vec{r}_1 d\vec{r}_2 \quad (1.6)$$

h is Planck's constant (erg s), c is the speed of light in vacuum (cm s^{-1}), $\rho_m(\vec{r})$ is the charge distribution of pigment h (statC cm^{-1}) and V_{mn} has units of wavenumbers (cm^{-1}). For finding the interaction potential between Chls, several methods can be employed,^{85,86} e.g., the point dipole approximation. In this work, the transitions from electrostatic potentials (TrEsp) method is used, for which eq 1.6 is rewritten as^{85,87}

$$V_{mn} = \frac{1}{hc} \sum_{i,j} \frac{q_i(1,0) q_j(1,0)}{|\vec{r}_i - \vec{r}_j|} \quad (1.7)$$

with the indices i and j running over the nuclei of pigments m and n respectively, transition charges $q(1,0)$ of the $S_0 \rightarrow S_1$ transition and \vec{r}_i the nuclear position of $q_i(1,0)$. The charges are determined for various pigments using time-dependent density functional theory^{87–89} and are scaled to yield the appropriate vacuum dipole moments.

1.2.2. Electron-Phonon Coupling

In model calculations, the protein is treated as a phonon bath. The bath Hamiltonian is described as a collection of harmonic oscillators:

$$\hat{H}_b = \sum_{m,i} \tilde{\nu}_{mi} \left(\hat{a}_{mi}^\dagger \hat{a}_{mi} + \frac{1}{2} \right) \quad (1.8)$$

where $\tilde{\nu}_{mi}$ is the wavenumber of mode i for site i , and \hat{a}_{mi}^\dagger and \hat{a}_{mi} are the creation and annihilation operators of mode i .⁹⁰ The system-bath (linear electron-phonon (el-ph)) coupling can be described as

$$\hat{H}_{s-b} = - \sum_{m,i} \frac{\tilde{\nu}_{mi} d_{mi} (\hat{a}_{mi}^\dagger + \hat{a}_{mi})}{2} \hat{A}_m^\dagger \hat{A}_m \quad (1.9)$$

with d_{mi} equal to the displacement of the electronic excited state minimum along the normal mode reaction coordinate with respect to the ground electronic. Combining eq 1.2 with eqs 1.8 and 1.9 gives the total Hamiltonian (with respect to the ground state) as

$$\begin{aligned} \hat{H}_{tot} = \sum_{m,n,i} \left(\varepsilon_m - \frac{\tilde{\nu}_i d_{mi} (\hat{a}_{mi}^\dagger + \hat{a}_{mi})}{2} \right) \hat{A}_m^\dagger \hat{A}_m + V_{mn} \hat{A}_m^\dagger \hat{A}_n \\ + \tilde{\nu}_{mi} \left(\hat{a}_{mi}^\dagger \hat{a}_{mi} + \frac{1}{2} \right) \end{aligned} \quad (1.10)$$

The intensity distribution of phonon modes is given by the spectral density (phonon profile)

$$J_m(\tilde{\nu}) = \sum_i s_{mi} \delta(\tilde{\nu} - \tilde{\nu}_i) \quad (1.11)$$

with the dimensionless Huang-Rhys factor⁹¹ (s) of mode i for site m equal to $d_{mi}^2/4$. s is related to the Franck-Condon factors⁹²⁻⁹⁴

$$FC_{RP} = |\langle 1, R | 0, P \rangle|^2 = e^{-s} s^{R-P} \frac{P!}{R!} \left[L_P^{(R-P)}(s) \right]^2 \quad (1.12)$$

where $L_P^{(R-P)}(s)$ are the generalized Laguerre polynomials⁹⁵ and the subscript indicates a change from the P^{th} vibrational level in the ground electronic state to the R^{th} vibrational level in the excited state. For low-temperature considerations only the terms with $P = 0$ are relevant. Figure 1.5 shows the effects of el-ph coupling on the single-site fluorescence. Note that under the Franck-Condon approximation, fluorescence and absorbance lineshapes are mirror images about the zero-phonon line (ZPL). In practice, $J(\tilde{\nu})$ can be treated as a continuous function whose shape depends on the system under study. However, the functional form used to describe the phonon spectral density is critical in properly simulating optical spectra (see Chapter 2 for more details).

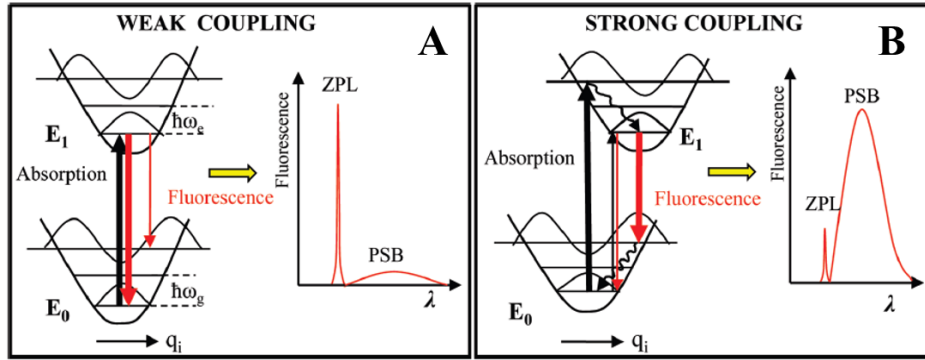


Figure 1.5 Energy level diagrams and single-site fluorescence spectra for weak (frame A) and strong (frame B) el-ph coupling. The thickness of an arrow is proportional to the Franck-Condon factor of that transition.⁹⁶

The temperature dependence of phonons is described by the Bose-Einstein distribution⁹⁷

$$n(\tilde{\nu}; T) = \frac{1}{e^{\tilde{\nu}/kT} - 1} \quad (1.13)$$

where k is the Boltzmann constant ($\text{cm}^{-1} \text{K}^{-1}$) and T is absolute temperature (K). Along with eq 1.11, we can now define a temperature-dependent phonon spectral density as

$$J(\tilde{\nu}; T) = (1 + n(\tilde{\nu}; T))J(\tilde{\nu}) + n(-\tilde{\nu}; T)J(-\tilde{\nu}). \quad (1.14)$$

$J(\tilde{\nu})$ is defined such that it is zero for $\tilde{\nu} \leq 0$, thus the second term on the right hand side is only nonzero for negative wavenumbers (representing phonon annihilation events). From eqs 1.13 and 1.14, one can see that $J(\tilde{\nu}; 0) = J(\tilde{\nu})$. The spectral density determines two important physical parameters, the total Huang-Rhys factor S and the optical reorganization energy E_λ ^{98,99}

$$S(T) = \int_{-\infty}^{\infty} J(\tilde{\nu}; T) d\tilde{\nu} \quad (1.15a)$$

$$E_\lambda = \int_{-\infty}^{\infty} \tilde{\nu} J(\tilde{\nu}; T) d\tilde{\nu} = \int_0^{\infty} \tilde{\nu} J(\tilde{\nu}) d\tilde{\nu} \quad (1.15b)$$

S is the average number of phonons coupled to an electronic transition and E_λ is the average energy needed to reorganize the nuclei after excitation. The spectral density is the key input parameter in Redfield theory and directly determines the shape of the phonon sideband (PSB), rate of exciton relaxation (which results in lifetime broadening of transitions), and (0,0)-transition energy shift due to E_λ .

1.2.3. Redfield and Förster Theories

Multilevel Redfield theory is a second-order perturbative method that applies a Markovian approximation to describe energy relaxation in the limit of strong dipole-dipole coupling.^{100,101} To simulate various optical spectra, this work employs a non-Markovian density matrix approach⁹⁹ for lineshape calculations which utilizes a Redfield-like rate equation to describe relaxation between exciton states. Often this non-Markovian approach is referred to simply as Redfield theory. The isotropic absorption cross-section and fluorescence probability can be given as^{102,103}

$$\sigma(\tilde{\nu}) = \frac{8\pi^3\tilde{\nu}}{3hc} \left\langle \sum_M |\vec{\mu}_M|^2 D_M(\tilde{\nu}) \right\rangle_{dis} \quad (1.16a)$$

$$F(\tilde{\nu}) = \frac{64\pi^4\tilde{\nu}^3}{3h^2c} \left\langle \sum_M \frac{e^{-E_M/kT}}{\sum_N e^{-E_N/kT}} |\vec{\mu}_M|^2 D'_M(\tilde{\nu}) \right\rangle_{dis} \quad (1.16b)$$

where $D_M(\tilde{\nu})$ is the lineshape function for exciton state M and $\langle \dots \rangle_{dis}$ indicates averaging over diagonal disorder (i.e., site energies). Similarly, the linear (LD) and circular dichroism (CD), expressed as absorption cross-section difference spectra, can be described by

$$\Delta\sigma_{LD}(\tilde{\nu}) = \sigma_{\parallel}(\tilde{\nu}) - \sigma_{\perp}(\tilde{\nu}) = \frac{4\pi^3\tilde{\nu}}{hc} \left\langle \sum_M (|\vec{\mu}_M|^2 - 3(\vec{\mu}_M \cdot \vec{n})^2) D_M(\tilde{\nu}) \right\rangle_{dis} \quad (1.17)$$

and

$$\Delta\sigma_{CD}(\tilde{\nu}) = \sigma_L(\tilde{\nu}) - \sigma_R(\tilde{\nu}) = \frac{32\pi^3\tilde{\nu}}{3hc} \left\langle \sum_M r_M D_M(\tilde{\nu}) \right\rangle_{dis} \quad (1.18)$$

respectively.^{99,104} The intensity of LD spectra depends on the orientation angle between the transition dipole and the membrane normal (\vec{n}).^{41,104} For eq 1.18, the dipole strength $|\vec{\mu}_M|^2$ is replaced by the excitonic rotational strength,

$$r_M = \frac{\pi}{2} \sum_{m,n} c_{mM} c_{nM} (\epsilon_m \vec{R}_m - \epsilon_n \vec{R}_n) \cdot (\vec{\mu}_m \times \vec{\mu}_n) \quad (1.19)$$

(note that intrinsic rotational strength and electric-magnetic coupling have been neglected).¹⁰⁵ eq 1.19 indicates that the excitonic CD spectrum (when corrected for linear frequency scaling) is conserved. Therefore, the experimentally determined r (eq 1.20) should vanish.

$$r = \frac{3hcn}{32\pi^3} \int_{\Delta\tilde{\nu}} \frac{\Delta\sigma_{CD}(\tilde{\nu})}{\tilde{\nu}} d\tilde{\nu} \quad (1.20)$$

In practice, the intrinsic contribution can be measured and subtracted from the measured CD to create a conserved spectrum.⁴¹ For example, $r = -8.7 \cdot 10^{-4}$ and $-7.4 \times 10^{-4} \text{ D}^2$ for Chl a at room temperature in ether¹⁰⁶ and at 1.7 K in protein (WSCP),¹⁰⁷ respectively.

In the simplest approximation, $D_M(\tilde{\nu})$ is a Dirac delta function centered at the exciton transition energy (so-called stick spectra).^{41,102} However, while static disorder is easily included by convolving the stick spectra with the site distribution function (SDF), this approach neglects dynamic disorder. A more accurate lineshape function, which accounts for both diagonal and off-diagonal exciton-vibration coupling, is derived from the reduced density matrix as⁹⁹

$$D_M^{(\prime)}(\tilde{\nu}) = e^{-\gamma_{MM}S(T)} \int_{-\infty}^{\infty} e^{\pm 2\pi i(\tilde{\nu}-\tilde{\nu}_M)\tau + \gamma_{MM}G(\tau) + \pi\Gamma_M|\tau|} d\tau \quad (1.21)$$

where + and - refer to $D_M(\tilde{\nu})$ (absorption) and $D_M'(\tilde{\nu})$ (fluorescence), respectively.

The main component of eq 1.21 is the temporal function $G(\tau)$, which corresponds to the inverse Fourier transform of the spectral density (including both phonon and intramolecular vibrational modes)^{99,108}

$$G(\tau) = \int_{-\infty}^{\infty} e^{-2\pi i\tilde{\nu}\tau} [J(\tilde{\nu}; T) + J_{vib}(\tilde{\nu}; T)] d\tilde{\nu} \quad (1.22)$$

Under the secular approximation γ_{MM} , which describes delocalization and a suppression of the el-ph coupling strength, is given as⁹⁹

$$\gamma_{MN} = \sum_{m,n} c_{mM} c_{mN} c_{nM} c_{nN} e^{-R_{mn}/R_c} \quad (1.23)$$

where R_c is the correlation radius of protein vibrations. In the limit of completely correlated fluctuations no exciton relaxation occurs; conversely, when fluctuations are completely uncorrelated the exciton relaxation rates are maximized.^{99,108} While R_c can be set to zero, a value of 5 Å has been proposed based on simulations of pump-probe spectra of the PSII RC¹⁰⁹ and a value of less than 10 Å has been hypothesized for the FMO complex.¹⁰⁸ Coupling to the environment also determines the amount of energy the system requires to reorganize the atomic nuclei after excitation. $\tilde{\nu}_M$ is the energy associated with the (0,0)-transition of state M ⁹⁹

$$\tilde{\nu}_M = E_M + \sum_N \gamma_{MN} \mathfrak{p} \int_{-\infty}^{\infty} \frac{\tilde{\nu}^2 J(\tilde{\nu}; T)}{E_{MN} - \tilde{\nu}} d\tilde{\nu} \quad (1.24a)$$

$$E_{MN} = E_M - E_N \quad (1.24b)$$

The first term on the right hand side of eq 1.24a is the eigenvalue from eq 1.3a and the second term describes the energy shift due to el-ph coupling (where \mathfrak{p} corresponds to the Cauchy principle part of the integral). The dominate term in the sum is for $N = M$ (diagonal exciton-vibration coupling) and is equivalent to $-\gamma_{MM} E_\lambda$ (eq 1.15b). The broadening term in eq 1.21 (Γ_M) produces finite width for the Lorentzian ZPL and depends on the rates of exciton relaxation⁹⁹

$$\Gamma_M = \sum_N k_{MN} \quad (1.25a)$$

$$k_{MN} = 2\pi \gamma_{MN} E_{MN}^2 J(E_{MN}; T) \quad (1.25b)$$

Equation 1.25b is similar to the standard Redfield rate equation^{108,110} and describes exciton relaxation as an exchange of energy between the system and bath due to off-diagonal coupling.

The corresponding exciton lifetime is given by

$$\tau_M = \frac{2}{\Gamma_M} \quad (1.26)$$

In the weak-coupling limit (when electronic coupling is much smaller than E_λ) the Redfield rate equation given by eq 1.25b is no longer applicable and the Förster rate equation must be used^{111,112}

$$k_{mn} = 2\pi |V_{mn}|^2 \int_{-\infty}^{\infty} D'_m(\tilde{\nu}) D_n(\tilde{\nu}) d\tilde{\nu} \quad (1.27)$$

In the Förster case, energy transfer is determined by the spectral overlap of the fluorescence lineshape of m with the absorption lineshape of n . As written, eq 1.27 describes radiationless energy transfer between excited states localized on individual pigments.^{72,111,112} Many natural pigment-protein complexes fall within the intermediate regime between strong and weak

coupling;¹¹³ exhibiting domains of strongly-coupled pigments which are weakly interacting with other domains of strongly-coupled pigments. In generalized Förster theory,^{114,115} the standard Förster rate equation (eq 1.27) is applied to delocalized exciton states in order to describe interdomain EET. That is,

$$k_{MaNb} = 2\pi|V_{MaNb}|^2 \int_{-\infty}^{\infty} D'_{Ma}(\tilde{\nu})D_{Nb}(\tilde{\nu})d\tilde{\nu} \quad (1.28)$$

where Ma indicates exciton state M in domain a . The exciton lineshapes and intradomain relaxation are treated by Redfield theory as given by eqs 1.21–1.26, with exciton delocalization restricted over only those pigments within the domain. In practice, this restriction is accomplished by setting interdomain coupling constants (V) in eq 1.2 to 0.^{115,116} However, the interdomain electronic coupling constants are used to calculate interdomain exciton coupling as

$$V_{MaNb} = \sum_{ma,nb} c_{maMa}c_{nbNb}V_{manb} \quad (1.29)$$

with, for example, ma indicating pigment m located within domain a . As seen by eq 1.28, interdomain EET is proportional to the exciton coupling between domains. The total rate of energy transfer from domain a to domain b depends on the thermally-weighted interdomain EET rates^{114,115}

$$k_{ab} = \sum_{Ma,Nb} \frac{e^{E_{Ma}/kT}}{\sum_{Ka} e^{E_{Ka}/kT}} k_{MaNb} \quad (1.30)$$

1.3. Laser-Based Spectroscopies

A principal method in which to investigate photophysical properties in photosynthetic systems is laser-based spectroscopy. Measurements can be carried out in both the frequency and time domains. With the development of pulsed lasers, ps and fs processes can be studied by photon echo,¹¹⁷ pump-probe,^{118,119} and two-dimensional electronic spectroscopy (2DES).^{120,121} As noted

in section 1.1.1, time-domain spectra have revealed interesting ultrafast coherent effects in FMO on a timescale of hundreds of femtoseconds.⁴²⁻⁴⁴ The excitation source in time-domain spectroscopies have a broad bandwidth in frequency due to the Mandelstam-Tamm inequality¹²²

$$\Delta E \Delta t \geq \frac{\hbar}{4\pi} \quad (1.31)$$

which relates the standard deviation in energy of a quantum system to its time-dependence over the interval Δt .

Complimentary to time-domain techniques are frequency-domain spectroscopies,^{96,123-125} which utilize continuous wave lasers with narrow bandwidth (quasimonochromatic) as opposed to pulsed excitation sources. In frequency-domain measurements, a small subpopulation within the disordered sample is probed and provides information on lineshapes and dynamics. Another method of overcoming energetic disorder is single complex spectroscopy,^{126,127} where very low concentrated samples allow for a single complex to be probed. Data for ensemble measurements can then be assembled by collecting statistical information for many complexes. Below only the frequency-domain techniques utilized in this work are covered in more detail.

1.3.1. Dynamic and Static Disorder

The lineshapes (i.e., PSB and lifetime broadening) discussed in section 1.2.3 pertain to dynamic (homogeneous) disorder.^{128,129} This type of disorder results from relaxation processes which occur on timescales shorter than the lifetime of the electronic excited state and describe shifts of the potential energy surface along the reaction coordinates of normal modes. For the linear el-ph approximation, the ZPL is a delta peak and only gains finite linewidth (Γ_{hom}) due to exciton relaxation caused by off-diagonal exciton-vibration coupling.⁹⁹ However, dephasing caused by quadratic el-ph coupling gives rise to the temperature dependence of Γ_{hom} ,^{96,128,130} although its contribution is negligible at low temperatures compared to lifetime broadening.⁹⁶

In addition to the dynamic disorder, slow (compared to the excited state lifetime) variations of the local environment leads to static (inhomogeneous) disorder which affects the transition energy of ZPLs.^{96,128,129} For a perfect crystal, all sites have identical environments and no static disorder exists, but sites in a glass matrix (amorphous solid) will experience shifts away from the average energy due to local interactions.⁹⁶ Figure 1.6 shows hypothetical pigments in a disordered matrix and the resulting effect on the transition energies. For photosynthetic systems, the pigments are often shielded from the surrounding glass matrix by the protein, with disorder among local protein binding sites contributing to shifts in transition energies. Static disorder is assumed to be normally distributed^{71,96,131} about the average energy with a full-width at half-maximum (FWHM) designated Γ_{inh} . The energy distribution is referred to as the SDF.⁹⁶ Unlike the dynamic disorder which is temperature-dependent (see eq 1.14), Γ_{inh} is not considered to depend on temperature;¹³³ although thermally-activated protein motion can lead to changes in the SDF.¹³⁴

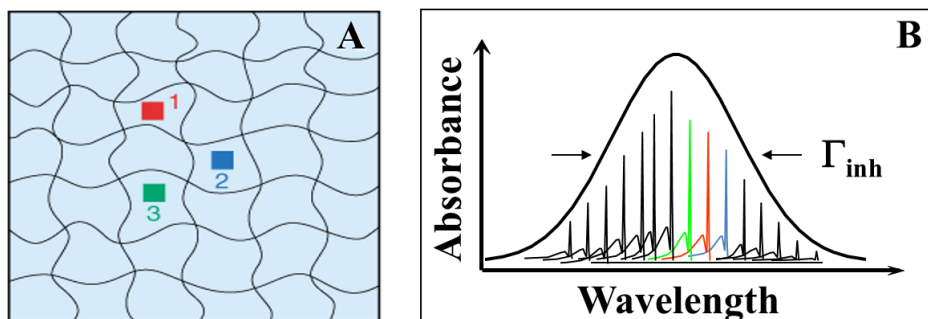


Figure 1.6 Frame A: schematic representation of several sites in different local environments. Frame B: representative distribution of transition energies showing how the ZPLs are normally distributed with a FWHM of Γ_{inh} .⁹⁶

A non-specific view of static disorder is often taken, with Γ_{inh} being elucidated from fits of simulated spectra. However, HB (vide infra) and single complex spectroscopies can provide direct experimental measurements of disorder.^{126,127} An example of a more microscopic treatment of disorder is the dichotomous model,^{75,135} where thermally-weighted protein conformations are

assumed to shift pigment site energies between two distributions. While models for structure-based calculations of site energies have been proposed,^{85,108,136} in general it is difficult to predict ε and Γ_{inh} based on only the protein environment. However, it is known that, for example, hydrogen bonding can redshift site energies of Chls and BChls by ~ 60 and ~ 100 cm^{-1} , respectively.¹³⁷ The static disorder and SDF mentioned so far applies to excited states localized on individual pigments. For exciton states, the extent of delocalization suppresses disorder due to exchange narrowing;¹³⁸ with the resulting width given by

$$\text{FWHM}_M = \sqrt{\sum_m |c_{mM}|^4 \Gamma_m^2} \quad (1.32)$$

where Γ_m represents Γ_{inh} of site m (assuming site-dependent Γ_{inh}).

1.3.2. Hole Burning and Fluorescence Line Narrowing

Two of the most common site-selective, frequency-domain spectroscopies are fluorescence line narrowing (FLN)^{41,96,129,139} and spectral hole burning (HB).^{96,123,124,129,140,141} FLN and HB experiments are carried out under liquid helium temperatures (~ 5 K) in order to decrease the contribution from the PSB and resolve the ZPL. For an ensemble of molecules in a disordered matrix, only those molecules which absorb resonant with the laser frequency will be excited and subsequently fluoresce. If the bandwidth of the laser is sufficiently narrow and scattered laser light is reduced (e.g., by creating a transparent glass matrix upon cooling), then the ZPL width is given by⁹⁶

$$\Gamma_{ZPL} = 2\Gamma_{hom} = \frac{1}{\pi c T_1} + \frac{2}{\pi c T_2^*} \quad (1.33)$$

where T_1 is the natural lifetime (in this case, the fluorescence lifetime) and T_2^* is the pure dephasing time. Scattered light In terms of the lineshape function and SDF, the FLN spectrum is given by

$$FLN(\tilde{\nu}) = \int_{-\infty}^{\infty} D'(\tilde{\nu} - \Omega)D(\tilde{\nu}_B - \Omega)N(\Omega)d\Omega \quad (1.34)$$

with $\tilde{\nu}_B$ the laser frequency and $N(\Omega)$ representing the SDF. As noted above, only those sites resonant with the laser will emit; as the $D(\tilde{\nu}_B - \Omega)$ term is the absorption lineshape shifted so that the ZPL is at the laser frequency. This term describes the probability of exciting a molecule by its ZPL or PSB.^{96,141-143}

HB concerns changes in the absorption spectrum of a sample after laser excitation. A HB spectrum is the difference between absorption spectra after (postburn) and before (preburn) excitation, respectively.^{96,124} A diagram of the experimental setup is shown in Figure 1.7, where the absorption spectra are measured by means of a Fourier transform infrared spectrometer (FTIR). The sample (S) is secured on a holder inside of the liquid helium cryostat (C), which is positioned within the beam path of the FTIR. A tungsten bulb (W) is used as a white light source for the probe. Characteristic of interferometers, the probe encounters a beam splitter (BS) which sends parts the signal to either a stationary or movable mirror. The probe beams are reflected back towards BS and interrogate the sample. The resultant is detected by a photodiode (PD) and the preburn absorption recorded. For the burning step, W is turned off and the laser shutter is opened. Laser intensity is controlled by a stabilizer and neutral density filter (ND). The laser burns (excites) the sample for a certain time before the shutter is closed. To record the changes induced by burning, W is turned on and the sample absorption is measured as before.

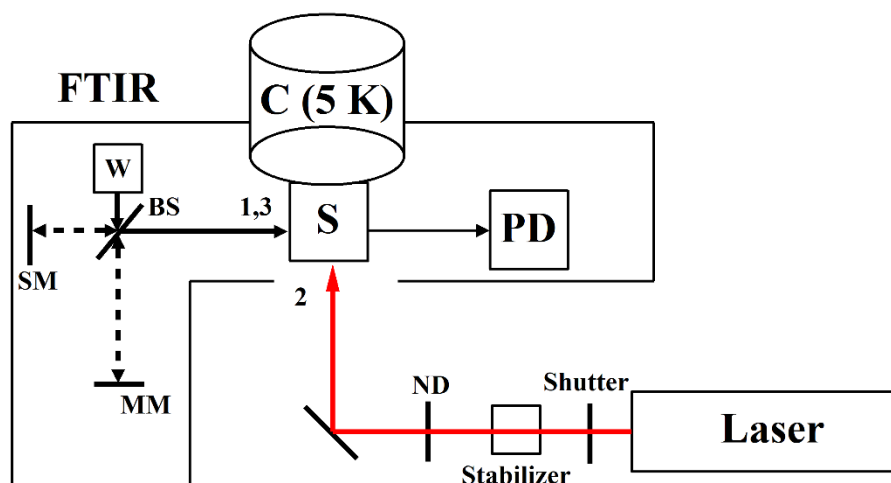


Figure 1.7 Experimental setup for low-temperature absorption and HB measurements. The sample (S) is illuminated three times: first by the white light probe in order to record the preburn absorption (1), followed by excitation with the narrow-band laser source (2), and finally the FTIR probe measures the postburn absorption (3).

In order to record fluence-dependent spectra, the above procedure continues by alternating between burn and probe steps until saturation (i.e., the sample no longer undergoes any laser-induced changes). As long as low temperature is maintained, the absorption changes persist and the HB spectra (postburn minus preburn) exhibit persistent holes. Transient spectra can also be measured when the system enters a long-lived state, such as a triplet or CS state with lifetimes on the order of μs to ms .^{78,144} In this case, the sample is continuously excited during recording of the absorption spectrum. That is, the absorption is measured while the shutter is open and the system is in, for example, a triplet-bottleneck. Since both persistent and transient burning occur simultaneously, another absorption spectrum is measured (post-transient) which contains only the contribution from persistent changes (i.e., measured with the shutter closed). The transient HB spectrum is the difference of the post-transient minus the transient absorption.

Two types of HB mechanisms are discussed in the literature:^{96,124,145} photochemical and nonphotochemical. Photochemical HB (PHB) results from changes in the absorbing molecule itself (such as photooxidation or proton tautomerization).^{71,146,147} The transition energy distribution before and after PHB occurs are referred to as the educt and product, respectively, and often experience far energetic separation. In nonphotochemical HB (NPHB), small changes in energy result from a rearrangement of the local environment upon excitation of the pigment.^{96,145,148,149}

Figure 1.8 shows a diagram depicting NPHB of a single site. Upon excitation, phonon-assisted tunneling can occur in the excited state and upon relaxation the system is in a new ground state. If the thermal energy is sufficiently low, the potential barrier between the two ground states cannot be overcome. Therefore, the pigment is trapped in the new ground state as long as low temperature is maintained and persistent holes result.^{96,145}

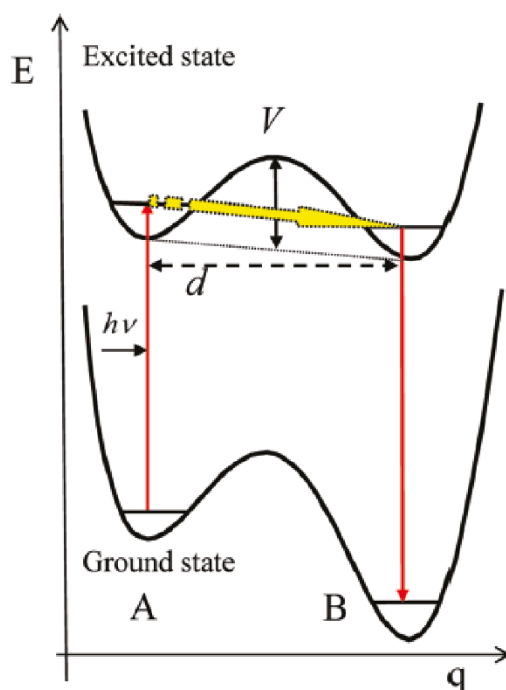


Figure 1.8 Energy level diagram illustrating the phonon-assisted tunneling mechanism of NPHB. The pigment is modeled as a multi-welled two level system. Red arrows represent excitation and relaxation, while the yellow arrow indicates tunneling in the excited state.^{96,150,151}

The absorption spectrum dependent on burn time (t_B) is given as^{96,152,153}

$$A(\tilde{\nu}, t_B) = \int_{-\infty}^{\infty} D(\tilde{\nu} - \Omega) N(\Omega) e^{-P\sigma(\tilde{\nu})\phi D(\tilde{\nu}-\Omega)t_B} d\Omega \quad (1.35)$$

where P is the laser power, $\sigma(\tilde{\nu})$ is the absorption cross section, and ϕ is the HB efficiency. For the preburn absorption, the exponent in the integrand equals one and the resulting absorption is the convolution of the lineshape function with the SDF (i.e., assuming a model of correlated disorder).

The HB spectrum is the difference between postburn and preburn spectra, which reduces to

$$HB(\tilde{\nu}, t_B) = \int_{-\infty}^{\infty} D(\tilde{\nu} - \Omega) N(\Omega) (e^{-P\sigma\phi D(\tilde{\nu}-\Omega)t_B} - 1) d\Omega \quad (1.36)$$

Figure 1.9 shows representative preburn and postburn absorption spectra, as well as the resulting HB spectrum. In correspondence to FLN spectra, which are composed of a ZPL and PSB, the HB spectra display a sharp zero-phonon hole (ZPH) resonant with the laser and two PSB holes (PSBHs).^{96,128,129} At higher energy than the ZPH is the real-PSBH, which results from a bleach of molecules excited via their ZPL. The pseudo-PSBH is observed due to a bleach of pigments via their PSBs. For low laser fluence only the sharp ZPH will be resolved and its intensity is given by the SDF. Thus, if many HB spectra are collected at constant fluence across the absorption band, the ZPH intensities will trace out the SDF.^{71,96,131} The envelope of the ZPH intensities is called the ZPH action spectrum and its FWHM is approximately Γ_{inh} (or FWHM_M for delocalized states).

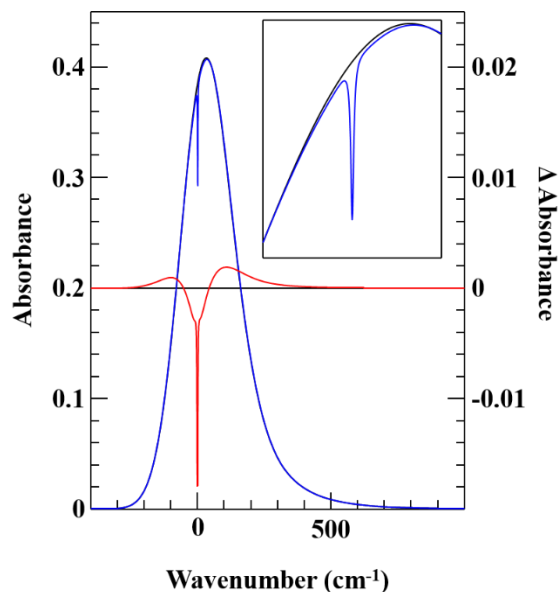


Figure 1.9 Preburn (black), postburn (blue) and HB (red) spectra for an inhomogeneously broadened absorption band. The HB spectra is multiplied by 10 and the ZPH is cut for clarity. The wavenumber scale is relative to the SDF peak position. The inset shows more clearly the differences between pre- and postburn spectra near $\tilde{\nu}_B$.

For molecular aggregates where EET is present, energy transfer competes with HB and lowers the HB efficiency.

$$\phi = \frac{\Omega_0 e^{-2\lambda}}{\Omega_0 e^{-2\lambda} + \tau_{fl}^{-1} + \tau_{EET}^{-1}} \quad (1.37)$$

The term in the numerator corresponds to the tunneling probability of the two level system, while τ_{fl} and τ_{EET} are the fluorescence lifetime and energy transfer time, respectively.⁹⁶ The tunneling probability in the excited state (see yellow arrow in Figure 1.8) depends on the tunneling parameter λ and prefactor Ω_0 .^{96,152} The implication from eq 1.37 is that the presence of EET lowers the HB yield for all but the trap states (where no further EET occurs). An example of this phenomena is the inability to burn ZPHs in the BChl *c* absorption maximum of the chlorosome,²⁶ consistent with time-domain measurements indicating very fast exciton relaxation to the lowest energy state.

Additionally, as mentioned previously energy transfer will produce lifetime broadening. That is, for low-fluence

$$\Gamma_{ZPH} = 2\Gamma_{hom} = \frac{1}{\pi c T_1} + \frac{2}{\pi c T_2^*} + \frac{1}{\pi c \tau_{EET}} \quad (1.38)$$

At low temperatures T_2^* is much longer than T_1 (which is on the order of nanoseconds for Chls). Since Redfield and Förster EET are on the orders of femtoseconds to picoseconds, τ_{EET} is the dominate term in eq 1.38 and the ZPH width is a direct measure of the energy transfer time.

Another powerful site-selective techniques is difference FLN (Δ FLN).^{154–156} Δ FLN is the difference of two FLN spectra before and after low-fluence HB.^{96,154} As Δ FLN combines the FLN and HB processes it is doubly selective, that is only pigments contributing to selective burning and selective excitation contribute to the Δ FLN spectrum.^{96,143}

$$\Delta FLN(\tilde{\nu}, t) = \int_{-\infty}^{\infty} D'(\tilde{\nu} - \Omega) D(\tilde{\nu}_B - \Omega) N(\Omega) (1 - e^{-P\sigma\phi D(\tilde{\nu}_B - \Omega)t}) d\Omega \quad (1.39)$$

An important property of Δ FLN is that its shape is proportional to the single-site fluorescence spectrum,^{157–159} meaning there is no contribution from the pseudo-PSB. Therefore, comparisons of calculated lineshape functions to the Δ FLN spectrum can be used to elucidate spectral density parameters. Additionally, $S(T)$ can be found from the Debye-Waller factor (α)^{96,160,161}

$$\alpha = \frac{I_{ZPL}}{I_{ZPL} + I_{PSB}} = e^{-S(T)} \quad (1.40)$$

where I_{ZPL} and I_{PSB} are the integrated intensities of the ZPL and PSB, respectively. Thus, Δ FLN is a useful technique for determining el-ph coupling parameters experimentally.

1.4. Organization of Dissertation

Chapter 2 provides a careful study of various functional forms for the spectral density. Comparisons between experimental Δ FLN and calculated single-site fluorescence spectra are given in order to determine which distributions yield physically realistic lineshapes and el-ph

coupling parameters. Chapter 3 describes a low-temperature study of FMO complexes from *C. tepidum*; revealing a small Stokes shift and the presence of intact and destabilized samples. Chapter 4 presents Redfield calculations of the low-energy 825 nm absorption band of FMO, in which intermonomer energy transfer is necessary to describe low-temperature absorption, fluorescence and nonresonant HB spectra. The results of Chapter 4 are expanded in Chapter 5, where simulations of the entire FMO trimer are given. Energy transfer, the site energy of BChl *a* 8, and various models of disorder are discussed as they pertain to fits of various optical spectra. Chapter 6 provides a HB study of LvWSCP, in which nonconservative holes are attributed to PHB proceeding by a mechanism of electron exchange between Chls and the nearby protein environment. Chapter 7 contains conclusions and future directions.

Chapter 2

On the Shape of the Phonon Spectral

Density in Photosynthetic Complexes

Adam Kell,[†] Ximao Feng,[†] Mike Reppert,[§] and Ryszard Jankowiak^{†,‡}

[†]Department of Chemistry and [‡]Department of Physics, Kansas State University, Manhattan,
Kansas 66506, USA

[§]Department of Chemistry, Massachusetts Institute of Technology, Cambridge, Massachusetts
02139, USA

Reproduced from the *Journal of Physical Chemistry B* **2013**, *117*, 7371–7323

Copyright 2013 American Chemical Society

Abstract

We propose a critical assessment of typical phonon spectral densities, $J(\tilde{\nu})$, used to describe linear and nonlinear optical spectra in photosynthetic complexes. Evaluation is based on a more careful comparison to experiment than has been provided in the past. $J(\tilde{\nu})$ describes the frequency-dependent coupling of the system to the bath and is an important component in calculations of EET times. On the basis of the shape of experimental $J(\tilde{\nu})$ obtained for several photosynthetic complexes, we argue that the shape of $J(\tilde{\nu})$ strongly depends on the pigment–protein complex. We show that many densities (especially the Drude–Lorentz/constant damping Brownian oscillator) display qualitatively wrong behavior when compared to experiment. Because of divergence of $J(\tilde{\nu})$ at zero frequency, the Brownian oscillator cannot fit a single-site spectrum correctly. It is proposed that a lognormal distribution can be used to fit experimental data and exhibits desired attributes for a physically meaningful phonon $J(\tilde{\nu})$, in contrast to several commonly used spectral densities which exhibit low-frequency behavior in qualitative disagreement with experiment. We anticipate that the lognormal $J(\tilde{\nu})$ function proposed in this work will be further tested in theoretical modeling of both time- and frequency-domain data.

2.1 Introduction

The primary input into energy transfer and lineshape calculations for excitonic systems is a spectral density, $J(\tilde{\nu})$, which describes the coupling of the electronic transition to matrix vibrations. Rate constants for exciton transfer, as well as lineshape functions of optical transitions, strongly depend on the shape of $J(\tilde{\nu})$ of exciton-vibration coupling.¹⁶² Although experimental data clearly indicate that the shape of $J(\tilde{\nu})$ varies depending on the photosynthetic system under consideration,^{163–165} in theoretical studies standard functional forms are often assumed for $J(\tilde{\nu})$ which either deviate significantly from experimental data or are valid only for specific systems.⁹⁹ Many efforts have been undertaken to extract the bath spectral densities from mixed quantum-classical calculations.^{166–169} Various semiclassical corrections to the spectral density have also been investigated.¹⁶⁹ Direct calibration against experiment, however, is generally difficult due to the inherently broad spectral transitions observed for room temperature photosynthetic complexes.

Below, we provide a critical assessment of $J(\tilde{\nu})$ typically used to describe linear and nonlinear optical spectra, such as those obtained from spectral HB and 2DES. We argue that many functions used so far either poorly describe the shape of $J(\tilde{\nu})$ or cause clear difficulties in spectral calculations.

To avoid confusion, we adopt the definition of May and Kühn for $J(\tilde{\nu})$:⁹⁸

$$J(\tilde{\nu}) = \sum_i s_i \delta(\tilde{\nu} - \tilde{\nu}_i) \quad (2.1)$$

with $s_i = \tilde{\nu}_i d_i^2 / 4$, the dimensionless Huang-Rhys factor for each bath mode indicating the strength of el-ph coupling. Here, $\tilde{\nu}_i$ is the frequency of the i^{th} bath mode and d_i is the displacement of the i^{th} bath mode minimum in the ground and excited electronic state potential energy surfaces. $J(\tilde{\nu})$

(in units of wavenumbers) is sometimes referred to as the phonon profile and defines the total Huang-Rhys factor⁹⁸

$$S = \int_0^{\infty} J(\tilde{\nu}) d\tilde{\nu} = \sum_i s_i \quad (2.2)$$

and reorganization energy

$$E_{\lambda} = \int_0^{\infty} \tilde{\nu} J(\tilde{\nu}) d\tilde{\nu} \quad (2.3)$$

Under this definition, $J(\tilde{\nu})$ differs by a factor of $\tilde{\nu}^2$ from the anti-symmetric component of the Fourier-Laplace transform of the energy gap correlation function

$$C''(\tilde{\nu}) = \tilde{\nu}^2 J(\tilde{\nu}) \quad (2.4)$$

which is itself sometimes referred to as the spectral density.¹⁷⁰ As the primary determinant of system-bath interactions in model calculations for excitonically coupled systems, $J(\tilde{\nu})$ directly determines both spectral characteristics and exciton relaxation dynamics.¹⁷¹

Although $J(\tilde{\nu})$ can be obtained by Δ FLN spectroscopy,^{163–165} to be useful one needs to express its shape by a function that can be used in theoretical calculations of the lineshape functions and EET rates. The shape of the spectral density is critical to properly describe various optical spectra and, in particular, exciton relaxation processes. Specifically, we suggest that for photosynthetic systems a proper model for $J(\tilde{\nu})$ should: (1) converge to zero as frequency approaches zero; (2) ensure that the quantity $\tilde{\nu}^2 J(\tilde{\nu})$ converges to zero at infinite frequency; and (3) fit the experimental profile obtained for $J(\tilde{\nu})$. The first condition has already been briefly discussed by Toutounji and Small¹⁷¹ in the context of ZPL widths and is necessary to ensure that the PSB in optical spectra decays toward zero near the ZPL, as consistently observed in experimental data. Note also that without this condition S may be undefined. The second criterion provides a well-defined value for E_{λ} and ensures under certain conditions (e.g., Redfield

relaxation) that the energy transfer rate decays to zero at infinite energetic separation. For simple lineshape and dynamics calculations (e.g., Förster or Redfield relaxation rates) these three conditions suffice, as all required spectral manipulations can be performed numerically. However, for more advanced calculations a convenient analytical form of the function may also be important. This is one of the reasons why many theoretical papers use either an Ohmic density with exponential cutoff or the overdamped Brownian oscillator (OBO) (vide infra). The functions describing $J(\tilde{\nu})$, along with corresponding equations defining S and E_λ , are summarized in Appendix A.

In the case where molecules are coupled to a continuum of low-frequency, damping modes and a single high-frequency mode, the anti-symmetric component can be written as:¹⁷²

$$C''(\tilde{\nu}) = C_0''(\tilde{\nu}) + C_{vib}''(\tilde{\nu}) \quad (2.5)$$

Of course coupling to multiples modes, especially on the low-frequency part of the vibronic spectrum (up to $\sim 500 \text{ cm}^{-1}$), might be relevant for energy transfer in the FMO complex.¹⁷³ In eq 2.5 the (fast) $C_0''(\tilde{\nu})$ mode corresponds to the a smooth background describing fluctuations due to the protein environment, while the second term expresses couplings to one or multiple discrete vibrational modes, which may be of intramolecular origin. Thus, the second term, $C_{vib}''(\tilde{\nu})$, represents the spectral density of (slow) molecular vibrations (damped or undamped) whose importance was recently addressed in the context of molecular vibrations in 2DES signals.¹⁷² The influence of fast vibrations on energy transfer continues to be of great interest; for example, recently Kolli et al.¹⁷⁴ showed the importance of high-energy quantized vibrations and their non-equilibrium dynamics for energy transfer in photosynthetic systems with highly localized excitonic states. Finally, we note that vibrational frequencies and their Huang-Rhys factors can be measured

by ΔFLN ¹⁵⁹ and HB spectroscopies.⁹⁶ In this manuscript, however, we focus only on the phonon spectral density.

2.2 Results and Discussion

Below we provide careful comparison of various spectral densities to experimental data. For example, we show that divergence of $J(\tilde{\nu})$ at zero frequency is in qualitative disagreement with experimental data. We argue that the OBO and Ohmic densities (vide supra) cannot fit a single-site spectrum correctly. We begin with a brief description and comparison of phonon spectral densities used so far in modeling studies. We focus on shortcomings and advantages of various functions used in theoretical calculations of optical spectra and EET rates in photosynthetic complexes.

2.2.1. Gaussian-Lorentzian

The empirical function given by a Gaussian distribution on the low-energy side and a Lorentzian distribution on the high-energy side (G-L) (see Appendix A) is often used in modeling of HB spectra and experimental $J(\tilde{\nu})$ obtained by ΔFLN spectra^{163–165} because its asymmetric shape is similar to experiment. Also, specific lineshape characteristics, peak position and FWHM, are input parameters; making adjustments to the lineshape simple and intuitive. This function, however, leads to infinitely large E_λ (vide infra) and cannot be used in energy transfer rate expressions. Problems can also arise in calculations of the ZPL, as certain values for peak position and Gaussian width result in a $J(\tilde{\nu})$ that does not decay to zero at zero frequency; leading to an unphysical broadening of the ZPL.¹⁷¹

2.2.2. B777

The B777 spectral density,⁹⁹ used in Redfield-based calculations of optical spectra of photosynthetic complexes and given below (eq 2.6), was obtained from the 1.6 K FLN spectra

measured for B777 complexes from LH1. The B777 complex contains a single BChl *a* molecule bound to a single α helix protein.⁹⁹

$$J(\tilde{\nu}) = \frac{S_0}{s_1 + s_2} \sum_{i=1,2} \frac{S_i}{7! 2\tilde{\nu}_i^4} \tilde{\nu}^3 e^{-(\tilde{\nu}/\tilde{\nu}_i)^{1/2}} \quad (2.6)$$

where $s_1 = 0.8$, $s_2 = 0.5$, $\tilde{\nu}_1 = 0.56 \text{ cm}^{-1}$ (0.069 meV) and $\tilde{\nu}_2 = 1.9 \text{ cm}^{-1}$ (0.24 meV). $J(\tilde{\nu})$ given by eq 2.6 is qualitatively reasonable (i.e., it captures the right physical trend; vide infra) but its shape could be improved by comparing to the shape of experimental Δ FLN spectra. Concerning the exciton-vibration coupling, Δ FLN spectra (not FLN spectra) provide valuable information on the spectral density, i.e., FLN signals and Δ FLN signals collected under the same conditions are not proportional to each other.^{142,159} Only Δ FLN spectra reduce directly to the single-site fluorescence lineshape function in the low-fluence limit,¹⁵⁹ providing information on the phonon spectral density. While the B777 $J(\tilde{\nu})$ has been applied to various photosynthetic complexes,^{108,114,175,176} due to the simplistic nature of the B777 protein it cannot represent a generic spectral density observed experimentally in various photosynthetic complexes, e.g., FMO,¹⁶³ the minor light harvesting antenna (CP29) from PSII,¹⁶⁴ WSCP.¹⁶⁵ This is especially true for the shape of $J(\tilde{\nu})$ for WSCP (vide infra), which has three clearly distinguishable peaks.¹⁶⁵ It has also been noted before that there exist differences between the B777 density and the G-L $J(\tilde{\nu})$ ¹⁶⁵ of the major light harvesting complex in PSII (LHCII), although it was suggested that the differences could be due to low-frequency protein vibrations improperly assigned as intramolecular modes.¹⁷⁶

Approximate functions have been proposed in the literature for the B777 $C''(\tilde{\nu})$ when applied to the B850 band of the LH2 antenna of purple bacteria,^{177–180} where application of the B777 $J(\tilde{\nu})$ would be most warranted due to the similar pigment-protein interactions (i.e., LH1 and LH2 have similar pigment-protein subunits⁹⁹). The alternative functions were used to preserve the

peak position and shape of $C''(\tilde{\nu})$, and to simplify calculations with the use of an interpolated formula when calculating the correlation function.^{178,181} These approximations were sums of Ohmic-like densities discussed below. A three term Super-Ohmic density was also used to approximate the B777 function when applied to bacterial RCs with CT states.¹⁸²

2.2.3. Brownian Oscillator

An often used functional form for the spectral density is the OBO or Drude-Lorentz density, which depends on E_λ , and a damping constant, γ :¹⁷⁰

$$C''(\tilde{\nu}) = \frac{2E_\lambda\gamma\tilde{\nu}}{\pi(\tilde{\nu}^2 + \gamma^2)} \quad (2.7)$$

Often when this function is used for $C''(\tilde{\nu})$, π^{-1} is included as part of E_λ . To keep our definitions consistent throughout the text, the π term is included in the denominator of the OBO function. This overdamped function is a special case of the more general multimode BO density obtained by assuming constant damping for a single mode at zero frequency.¹⁷⁰ Constant damping implies that

$$J(\tilde{\nu}) \sim \frac{1}{\tilde{\nu}} \text{ as } \tilde{\nu} \rightarrow 0 \quad (2.8)$$

Under this assumption the OBO $J(\tilde{\nu})$ mentioned above diverges at zero frequency, meaning that S is undefined and, as a result, the OBO $J(\tilde{\nu})$ will never fit single-site spectra correctly. Aside from failing to accurately describe experimental HB lineshapes, this leads to the intuitively undesirable result that single-site absorption and emission spectra can no longer be divided cleanly into R-phonon excitation profiles.⁹⁶ The careful modeling of the continuous part of the spectral density toward zero frequency is essential for the prevalence of coherence in molecular networks because it determines the pure dephasing rate, γ_d .¹⁸³ Also, the OBO $J(\tilde{\nu})$ does not yield long lasting cross-peak oscillations in 2D echo spectra of the seven-site FMO complex.^{183–185}

The more general multimode BO model is often used for describing high-frequency vibrations,^{166,186} while a modified OBO, the quantum overdamped bath function, has been proposed as it overcomes the slow Lorentzian decay of the standard OBO.¹⁷² However, if constant damping is assumed, both the multimode BO and quantum OBO functions suffer from the same drawbacks encountered by the standard overdamped form (e.g., infinite value at zero frequency and undefined S).

2.2.4. Ohmic

Another common function is the Ohmic-type spectral density of the form⁹⁸

$$C''(\tilde{\nu}) = \eta \tilde{\nu} \left(\frac{\tilde{\nu}}{\tilde{\nu}_c} \right)^{\alpha-1} e^{-\frac{\tilde{\nu}}{\tilde{\nu}_c}} \quad (2.9)$$

where α is the order of the function and η is a normalization factor that is directly proportional to E_λ (see Appendix A for details). The B777 function described earlier (see eq 2.6) is a sum of several densities with closely related forms (although the exponential cutoff in B777 is raised to the power of 1/2). Three types of densities can be distinguished: (1) sub-Ohmic ($0 < \alpha < 1$); (2) Ohmic ($\alpha = 1$); and (3) super-Ohmic ($\alpha > 1$); all of which are simply Gamma distributions multiplied by $\tilde{\nu}$ with various shape parameters (divided by $\tilde{\nu}^2$ in the case of $J(\tilde{\nu})$). Note that the designation of a density as “Ohmic” reflects the behavior of $C''(\tilde{\nu})$ at zero frequency: any Ohmic or sub-Ohmic choice for $C''(\tilde{\nu})$ will result in a $J(\tilde{\nu})$ that diverges at zero frequency, which is in qualitative disagreement with experiment.^{163–165}

2.2.5. Lognormal

Based on our extensive search for functions that could describe experimental $J(\tilde{\nu})$ in several photosynthetic complexes, we found that the lognormal distribution defined below is an excellent choice:

$$J(\tilde{\nu}) = \frac{S}{\tilde{\nu}\sigma\sqrt{2\pi}} e^{-\frac{[\ln(\tilde{\nu}/\tilde{\nu}_c)]^2}{2\sigma^2}} \quad (2.10)$$

where $\tilde{\nu}_c$ is the cutoff frequency and σ is the standard deviation. This lineshape is advantageous because it converges for large frequencies (e.g., both S and E_λ are defined) and has an adjustable asymmetry which describes very well the experimental $J(\tilde{\nu})$ and various optical spectra (to be reported elsewhere). This function also contains two adjustable parameters ($\tilde{\nu}_c$ and σ), unlike the other functions discussed previously, which rely solely on a cutoff frequency or damping constant (with the exception of G-L) as S and E_λ only affect normalization/peak amplitude. See Table A.1 in Appendix A for how parameters affect the shapes of different spectral densities.

2.2.6 Application to Photosynthetic Antenna Complexes

In this section, we present comparisons of a number of spectral density models with experimental data for a variety of photosynthetic complexes. Figures 2.1 and 2.2 focus on the FMO antenna complex. The FMO complex is an often studied system due to the presence of long-lasting quantum coherence exhibited in 2D spectra,^{43,44} and all functions mentioned in this text have been applied to model exciton relaxation and optical spectra of FMO. Figure 2.1 shows calculated single-site spectra compared to the experimental Δ FLN spectrum for FMO (*C. tepidum*),¹⁶³ as the shape of the phonon spectral density directly determines the PSB of the single-site spectrum.⁹⁶ Using the often published parameter values for the B777 density leads to a broadened single-site spectrum that cannot fit the experimental data (frame A). It should be noted that the main argument for using the B777 function to describe FMO comes from Figure 2 of ref 108. There, $J(\tilde{\nu})$ is compared directly to the experimental 4 K FLN spectrum (not Δ FLN as shown in this work) of FMO (*Pr. aestuarii*). For comparison, frame B plots the same experimental absorption spectrum together with the diverging $J(\tilde{\nu})$ profiles for the OBO and Ohmic functions. Although viable single-site absorption spectra can be calculated from these functions, due to the divergence of $J(\tilde{\nu})$

at zero frequency the corresponding spectra do not display a well-defined PSB; giving rise instead to broadening of the ZPL.¹⁷¹

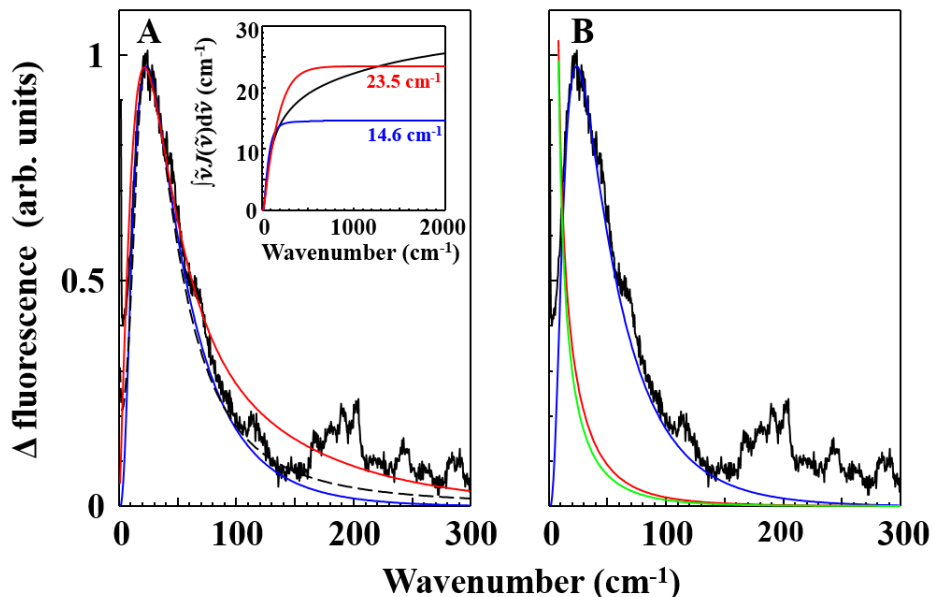


Figure 2.1 Frame A: experimental FMO (*C. tepidum*) Δ FLN spectrum (black, $\tilde{\nu}_{ex} = 12\,090\text{ cm}^{-1}$)¹⁶³ and single-site spectra calculated with G-L (black dashed, $\tilde{\nu}_m = 22\text{ cm}^{-1}$, $\Gamma_G = 22\text{ cm}^{-1}$, $\Gamma_L = 60\text{ cm}^{-1}$),¹⁶³ lognormal (blue, $\tilde{\nu}_c = 38\text{ cm}^{-1}$, $\sigma = 0.7$) and B777 (red) functions. The inset shows the integral of $\tilde{\nu}J(\tilde{\nu})$ ($S = 0.3$) for the corresponding curves. Frame B: Δ FLN and lognormal curves from frame A with single-site spectra calculated with OBO (red, $\gamma = 53\text{ cm}^{-1}$) and Ohmic (green, $\tilde{\nu}_c = 50\text{ cm}^{-1}$) functions. OBO and Ohmic fits scaled to match FWHM of ZPL (not shown).

The B777 density with modified parameters can be used to fit the *C. tepidum* data using only one term (i.e., $s_2 = 0$), as seen in Figure 2.2. Doing so, however, limits the function to one adjustable parameter, $\tilde{\nu}_1$, which will change both the peak position and curve width simultaneously. A theoretical spectral density for FMO could be directly obtained using a normal mode analysis,¹⁸⁷ though the average diagonal part of such a spectral density obtained for the monomeric subunit of the FMO protein significantly differed from the experimental average phonon spectral density obtained in ref 108 (eq 2.6 with $S_0 = 0.5$). The authors argued the deviation was likely due to anharmonicities experienced by the soft degrees of freedom that govern the

conformational flexibility of the macromolecule.¹⁶² Other studies have been made to directly determine, and fit with an analytical form, the energy gap autocorrelation function using molecular dynamics and electronic structure calculations.^{166,168,169}

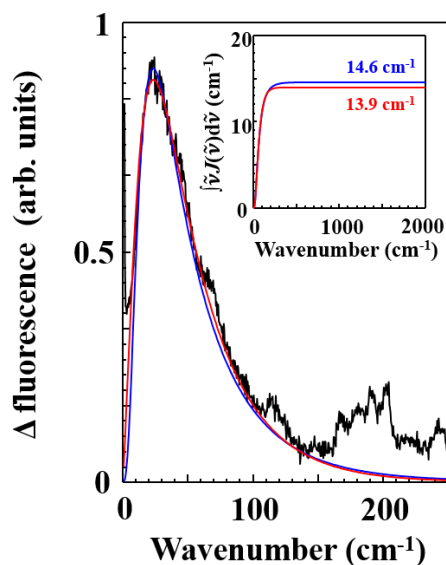


Figure 2.2 Experimental FMO (*C. tepidum*) Δ FLN spectrum (black, $\tilde{\nu}_{ex} = 12\,090\text{ cm}^{-1}$)¹⁶³ and single-site spectra calculated with lognormal (blue, $\tilde{\nu}_c = 38\text{ cm}^{-1}$, $\sigma = 0.7$) and modified B777 (red, $s_1 = 1$, $s_2 = 0$, $\tilde{\nu}_1 = 0.65\text{ cm}^{-1} = 0.08\text{ meV}$, $\tilde{\nu}_2 = 0\text{ cm}^{-1}$) functions. The inset shows the integral of $\tilde{\nu}J(\tilde{\nu})$ ($S = 0.3$) for each curve.

The CP29 antenna complex is involved in energy transfer within PSII. Frame A of Figure 2.3 shows the lognormal distribution ($\tilde{\nu}_c = 50\text{ cm}^{-1}$, $\sigma = 0.9$)¹⁸⁸ compared to the published G-L ($\tilde{\nu}_m = 22\text{ cm}^{-1}$, $\Gamma_G = 20\text{ cm}^{-1}$, $\Gamma_L = 110\text{ cm}^{-1}$)¹⁶⁴ and B777 densities. The G-L from ref 164 has a different lineshape compared to the others due to an improper contribution attributed to the pseudo-PSB in the Δ FLN data; however, this function cannot be used in calculations due to the lack of a well-defined E_λ (see inset). Using a lognormal fit to the G-L parameters above, as opposed to fitting Δ FLN data, for simultaneous calculations of various optical spectra results in site energies that are $\sim 30\text{ cm}^{-1}$ higher than those published recently¹⁸⁸ (data not shown). Thus, the precise shape of the spectral density is needed to obtain reliable site energies from modeling studies. The

lognormal and B777 calculated single-site spectra compared to the experimental data is shown in frame B of Figure 2.3. For CP29, both the lognormal and B777 functions fit the experimental data very well.

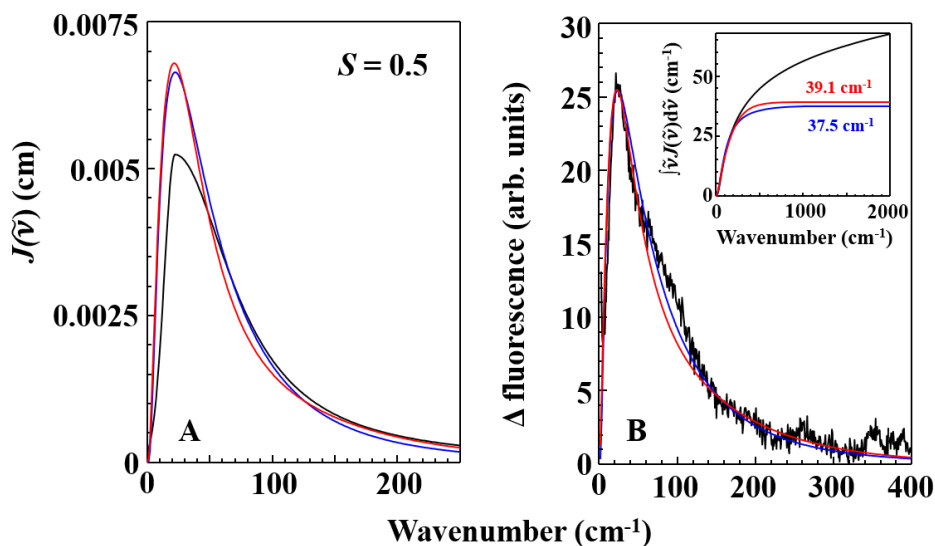


Figure 2.3 Frame A: $J(\tilde{\nu})$ curves obtained using the G-L (black, $\tilde{\nu}_m = 22 \text{ cm}^{-1}$, $\Gamma_G = 20 \text{ cm}^{-1}$, $\Gamma_L = 110 \text{ cm}^{-1}$),¹⁶⁴ lognormal (blue, $\tilde{\nu}_c = 50 \text{ cm}^{-1}$, $\sigma = 0.9$) and B777 (red) functions for CP29. Frame B: Experimental CP29 Δ FLN spectrum (black, $\tilde{\nu}_{ex} = 14\,620 \text{ cm}^{-1}$)¹⁶⁴ and single-site spectra calculated with lognormal (blue) and B777 (red) $J(\tilde{\nu})$ from frame A. The inset shows the integral of $\tilde{\nu}J(\tilde{\nu})$ ($S = 0.5$) for the corresponding curves.

A small pigment-protein complex that is neither bound to the thylakoid membrane nor directly involved in photosynthesis, WSCP of higher plants is a tetramer binding Chl *a* or Chl *b*.⁴⁶ Δ FLN data for CaWSCP have shown that $J(\tilde{\nu})$ has three distinct bands that contribute to the PSB, which are suggested to arise from delocalized vibrations that correspond to the protein tetramer, dimer and monomer.¹⁶⁵ Figure 2.4 shows the fit of the single-site spectrum calculated using the lognormal distribution with the experimental Δ FLN data for CaWSCP. To account for the detail available for WSCP, the lognormal $J(\tilde{\nu})$ used is a sum of three functions with parameters reported in Table 2.1. Also shown in Figure 2.4 is the published B777 function, which has been applied to WSCP in calculations of optical spectra.^{175,189} The B777 density is qualitatively similar to the

Δ FLN signal in peak position and width; however, it cannot reproduce the multiple peaks seen in experiment, meaning it will underestimate the contribution from phonon modes at certain peak positions (i.e., 24 and 88 cm^{-1} for Chl *a*, and 82 cm^{-1} for Chl *b*). The B777 parameters also overestimate E_λ by $\sim 20 \text{ cm}^{-1}$, as seen in the insets of Figure 2.4.

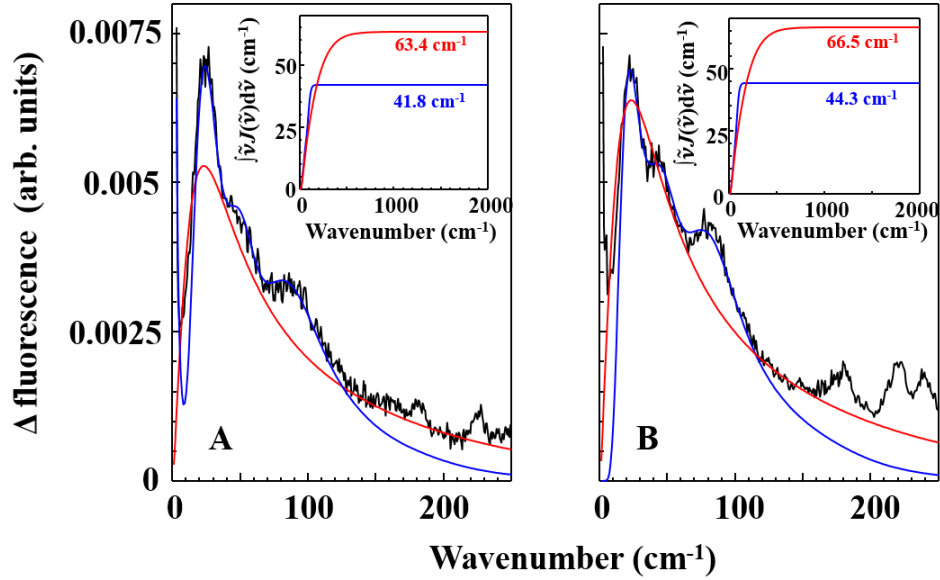


Figure 2.4 Frame A: experimental Chl *a*-CaWSCP Δ FLN spectrum (black, $\tilde{\nu}_{ex} = 14\,596 \text{ cm}^{-1}$)¹⁶⁵ and single-site spectra calculated with lognormal (blue) and B777 (red) functions. Frame B: experimental Chl *b*-CaWSCP Δ FLN spectrum (black, $\tilde{\nu}_{ex} = 15\,006 \text{ cm}^{-1}$)¹⁶⁵ and single-site spectra calculated with lognormal (blue) and B777 (red) functions. For the three term lognormal curves, parameters are listed in Table 2.1. Inset of each frame shows the integral of $\tilde{\nu}J(\tilde{\nu})$ ($S = 0.81$ and 0.85 for Chl *a* and Chl *b*, respectively) for the corresponding curves.

Table 2.1 Lognormal distribution parameters used to fit Δ FLN spectra for Chl *a*- and Chl *b*-CaWSCP*

Chl <i>a</i>	$\tilde{\nu}_c \text{ (cm}^{-1}\text{)}$	σ	S_i	Chl <i>b</i>	$\tilde{\nu}_c \text{ (cm}^{-1}\text{)}$	σ	S_i
1	28	0.4	0.45	1	26	0.4	0.39
2	54	0.2	0.15	2	51	0.25	0.23
3	90	0.2	0.21	3	85	0.2	0.23

* S_i is the relative contribution of each term to the total integrated area, which is 0.81 and 0.85 for Chl *a* and Chl *b*, respectively.¹⁶⁵

A comparison of Ohmic-type curves with the experimentally determined lognormal $J(\tilde{\nu})$ for FMO is shown in Figure 2.5. Curves 1–4 are obtained from eq 2.9 with $\alpha = 0.5, 1, 2$ and 3 , respectively; while the dashed curve is the lognormal $J(\tilde{\nu})$ used to calculate the single-site spectrum in Figure 2.1. Frames A and B show $\tilde{\nu}^2 J(\tilde{\nu})$ and $J(\tilde{\nu})$ for the parameters above, respectively. In frame A, all curves are normalized to the peak position and it is clear that the discrepancies between different Ohmic curves are greater on the high-frequency side of the peak position. However, all curves in frame A display the same qualitative shape. When one compares the corresponding $J(\tilde{\nu})$ curves (frame B), it becomes evident that only Super-Ohmic ($\alpha > 3$) curves display the same qualitative shape as $J(\tilde{\nu})$ derived from Δ FLN data. Even though the super-Ohmic ($\alpha = 2$) curve converges at zero frequency (S has a finite value), the curve poorly describes the experimental $J(\tilde{\nu})$ and $\tilde{\nu}^2 J(\tilde{\nu})$ curves. The nonzero phonon contribution at zero frequency will also introduce broadening effects to the ZPL.¹⁷¹

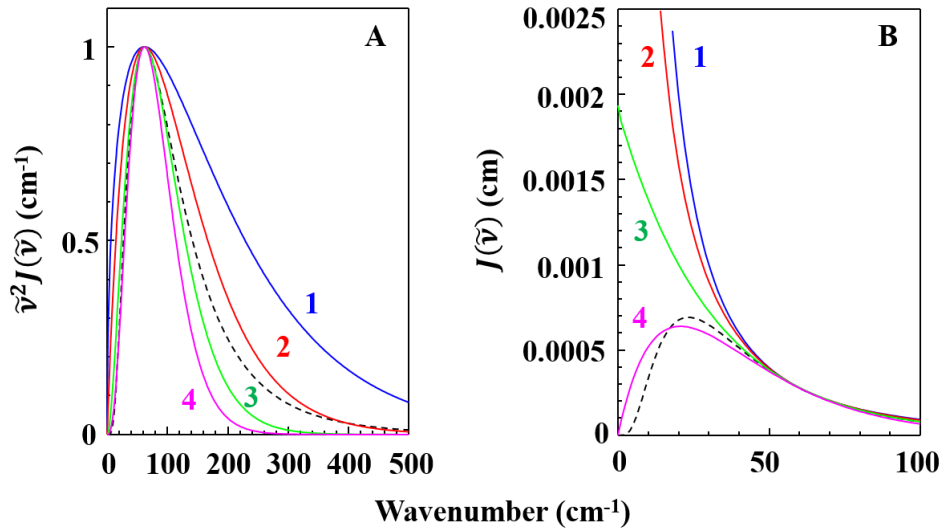


Figure 2.5 Frame A: curve 1–4 are normalized Ohmic-type functions (eq 2.9) obtained for the following parameters: (1) $\alpha = 0.5$, $\tilde{\nu}_c = 124$ cm⁻¹; (2) $\alpha = 1$, $\tilde{\nu}_c = 62$ cm⁻¹; (3) $\alpha = 2$, $\tilde{\nu}_c = 31$ cm⁻¹; (4) $\alpha = 3$, $\tilde{\nu}_c = 20.7$ cm⁻¹. The dashed curve is the FMO lognormal $J(\tilde{\nu})$, multiplied by $\tilde{\nu}^2$. Frame B: corresponding $J(\tilde{\nu})$, i.e., the curves in frame A divided by $\tilde{\nu}^2$.

A comparison of both Ohmic ($\alpha = 1$) and OBO curves, using parameters published previously for FMO, to the lognormal curve is shown in Figure 2.6. The $\tilde{\nu}_c$ values for the Ohmic curves are 50,¹¹⁶ 100¹⁹⁰ and 150¹⁹¹ cm^{-1} for curves 1–3, respectively (frame A). The γ values for the OBO $J(\tilde{\nu})$ curves are 32,¹⁹² 53¹⁹³ and 106¹⁹⁴ cm^{-1} (which correspond to γ^{-1} values of 166, 100 and 50 fs), respectively (frame B). Note that Ohmic and OBO curves with $\tilde{\nu}_c$ and $\gamma \sim 50 \text{ cm}^{-1}$ match the peak position of the lognormal curve fairly well (see also curve 2 in Figure 2.5A). However, the corresponding $J(\tilde{\nu})$ functions diverge at zero frequency and S is undefined; as seen in Figure 2.5 for the Ohmic function. For both the Ohmic and OBO functions, the peak position and width are dependent upon the same parameter ($\tilde{\nu}_c$ and γ , respectively), i.e., as the peak position increases in frequency the curve broadens. Thus, if the peak position is not matched, then the resulting curves are too broad and high frequency modes are improperly weighted. This is truer of the OBO function than of the Ohmic, due to the OBO function having a slow Lorentzian decay.

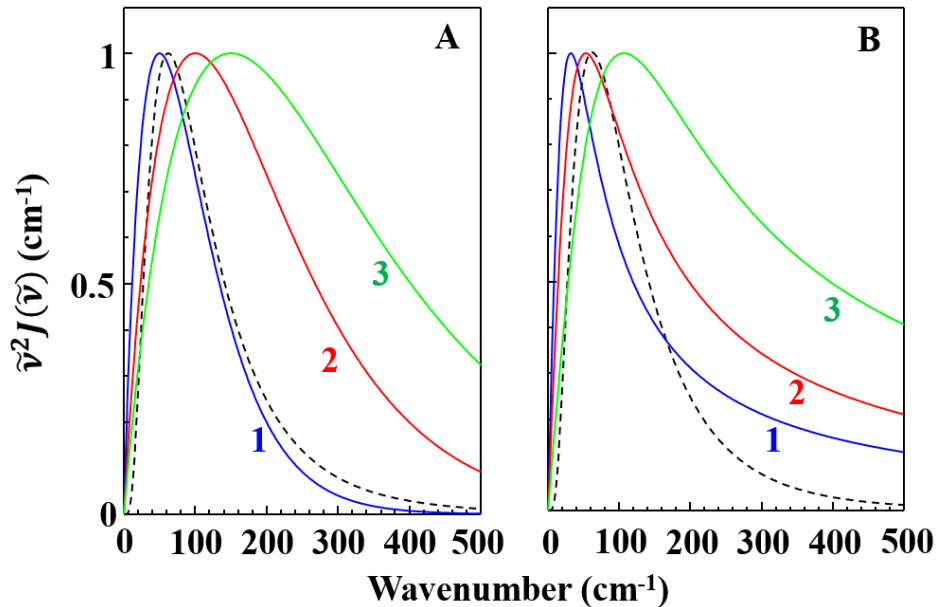


Figure 2.6 Frame A: normalized curves for the Ohmic ($\alpha = 1$) function. Curves 1–3 were obtained with $\tilde{\nu}_c$ values of 50, 100 and 150 cm^{-1} , respectively (see eq 2.9). Frame B: normalized curves defined by eq 2.7 for the OBO function. Curves 1–3 were obtained with γ values of 32, 53 and 106 cm^{-1} (which correspond to γ^{-1} values of 166, 100 and 50 fs), respectively. In each frame, the dashed curve is the FMO lognormal $J(\tilde{\nu})$, multiplied by $\tilde{\nu}^2$.

2.3. Concluding Remarks

We have demonstrated that many shapes of the commonly used spectral densities, especially the OBO (or Drude-Lorentz) and Ohmic $J(\tilde{\nu})$, are qualitatively wrong in comparison to experiment. The B777 $J(\tilde{\nu})$ (with a qualitatively reasonable shape) can only be used if its parameters can be adjusted to fit experimental Δ FLN spectra. We have shown that experimentally measured $J(\tilde{\nu})$ of FMO, the CP29 antenna complex of PSII and WSCP can be well described using the proposed lognormal function. Based on the examples discussed above, it is clear that the shape of $J(\tilde{\nu})$ strongly depends on the pigment-protein complex. This is not surprising; as the interaction of the vibrations with different environments will vary from system to system (it is the protein environment that adjusts the pigment site energies). Pigment binding to the protein scaffolding may also affect frequency and intensity of existing chromophore vibrations. This could lead to frequency shifts or suppression of certain backbone motions by formation of additional bonds to the protein environment; the latter was illustrated by Δ FLN spectra obtained recently for WSCP.¹⁶⁵ Thus, the functional form of $J(\tilde{\nu})$ is very important for further refinement of various theoretical models describing the spectral lineshape and, in particular, population dynamics in photosynthetic complexes.^{108,116,168,173} We suggest that the G-L $J(\tilde{\nu})$ used in modeling of HB spectra should be replaced with the lognormal function or B777 (with adjusted parameters), which provide a more physically realistic fit of the high-energy side of experimental spectral densities. The absence of the long Lorentzian tail in the lognormal function eliminates problems associated with continuously increasing E_λ , which is not well defined since the integral does not converge for the Lorentzian. The lognormal form also solves problems with the zero frequency behavior of the constant damping BO $J(\tilde{\nu})$, which contradicts experiment. We anticipate that the $J(\tilde{\nu})$ function

proposed in this work (see eq 2.10) will be successfully tested in theoretical modeling of both time- and frequency-domain data.

Despite the central role that the spectral density plays in excitonic dynamics and energy relaxation, a thorough general understanding of how specific spectral density features influence dynamics is still lacking. Here we only note that very recently it has been demonstrated that electronic coherence and fast thermalization depend sensitively on the continuum part of the spectral density;¹⁸³ therefore it is critical to use functions that properly describe the experimental $J(\tilde{\nu})$. In modeling of 2DES data obtained for photosynthetic complexes, both parts of the spectral density, i.e., $C_0''(\tilde{\nu})$ and $C_{vib}''(\tilde{\nu})$, need to be considered,¹⁷² as coherent excitonic dynamics may assist coupling to selected modes that channel energy to preferential sites in the complex.¹⁷⁴ The effect of various spectral densities on the calculated 2DES spectra, in particular on the extent of long-lasting and purely electronic, electronic/vibronic, or vibronic coherence has been discussed in ref 172. Thus, we conclude that experimentally determined $J(\tilde{\nu})$ must be used in modeling studies of a particular protein complex, as its shape is very important in the proper description of bath relaxation dynamics associated with the exciton transfer process. For example, careful modeling of the continuous part of the $J(\tilde{\nu})$ toward zero frequency is essential for the prevalence of coherence in molecular networks because it determines the pure dephasing rate.¹⁸³

Acknowledgments

This work was supported by the Chemical Sciences, Geosciences and Biosciences Division, Office of Basic Energy Sciences, Office of Science, U.S. Department of Energy (Grant No. DE-FG02-11ER16281 to R.J.). Partial support for A.K. was provided by European Social Fund's Doctoral Studies and Internationalisation Programme DoRa during a short research visit to the University of Tartu (UT), Estonia. We acknowledge useful discussions with Drs. Jörg Pieper (UT) and Arvi Freiberg (UT), and Drs. Margus Rätsep (UT) and Jörg Pieper for sharing with us x-y data of their previously published Δ FLN spectra.

Chapter 3

On Destabilization of the Fenna-Matthews-Olson

Complex of *Chlorobaculum tepidum*

Adam Kell,[†] Khem Acharya,[†] Robert E. Blankenship,[§] and Ryszard Jankowiak^{†,‡}

[†]Department of Chemistry and [‡]Department of Physics, Kansas State University, Manhattan, Kansas 66506, USA

[§]Departments of Chemistry and Biology, Washington University in St. Louis, St. Louis, Missouri 63130, USA

Reproduced from *Photosynthesis Research* **2014**, *120*, 323–329

Copyright 2014 Springer Science and Business Media

Abstract

The FMO complex from the GSB *C. tepidum* was studied with respect to its stability. We provide a critical assessment of published and recently measured optical spectra. FMO complexes were found to destabilize over time producing spectral shifts, with destabilized samples having significantly higher HB efficiencies; indicating a remodeled protein energy landscape. Observed correlated peak shifts near 825 and 815 nm suggest possible correlated (protein) fluctuations. It is proposed that the value of 35 cm^{-1} widely used for E_λ , which has important implications for the contributions to the coherence rate,¹⁸³ in various modeling studies of 2DES is overestimated. We demonstrate that the value of E_λ is most likely 15 to 22 cm^{-1} and suggest that spectra reported in the literature (often measured on different FMO samples) exhibit varied peak positions due to different purification/isolation procedures or destabilization effects.

3.1 Introduction

GSB contain a BChl *a* binding antenna complex called the FMO protein.^{27–29} FMO connects the chlorosome to the RC in the cytoplasmic membrane and functionally forms a bridge to transfer excitation energy. The structure of FMO from *C. tepidum* has been determined by X-ray diffraction to be a trimer with C₃-symmetry containing seven BChl *a* pigments per monomer.³⁶ A more recent model of the crystal structure includes an eighth pigment in a similar binding pocket as observed for *Pr. aestuarii*,³⁹ while mass spectrometry data revealed BChl *a* 8 in *C. tepidum* with partial occupancy.⁴⁰ Currently, only a single monomer is taken into account in simulations of optical spectra and, due to an assumed low occupancy or absence in isolated complexes, the eighth pigment is often neglected.^{108,116,195} Even so, different sets of electronic site energies used in theoretical studies lead to differences in the reported transfer dynamics,^{108,116,195} which may cause additional suppression or enhancement of oscillations (i.e., long-lived quantum coherences). This work will address differences arising in FMO sample preparations that, at least in part, contribute to the vast amount of site energies available and the absence of a consensus about the excitonic structure in the literature.

To study stability and intactness of various FMO samples from *C. tepidum* we use absorption, emission, and HB spectroscopies. HB relies on differences observed in the absorption spectrum of a low-temperature system after narrow-band laser excitation. In general, if a pigment molecule (in resonance with the laser) undergoes a photochemical reaction, it ceases to absorb at its original wavelength/frequency and one speaks of PHB. In the case of NPHB the pigment molecule does not undergo a chemical reaction, but its immediate environment experiences some rearrangement; for more details see refs 96 and 196. Both PHB and NPHB result in the formation of persistent holes, meaning the holes are preserved after the initial excitation is turned off, as long

as low temperature is maintained. In either case, the HB spectrum is obtained as the difference between the measured absorption spectrum before and after laser excitation. Both resonant and nonresonant holes can be obtained.⁹⁶ In this work we focus on nonresonant (persistent) holes formed by downward energy relaxation along the “excitonic energy ladder” within the trimer; such holes reveal the shape of the lowest energy excitonic state from which emission occurs. A theoretical description of the excitonic structure of the entire trimer and EET processes will be discussed elsewhere.

3.2 Materials and Methods

FMO complexes were prepared as described previously^{197,198} with a 50 mM Tris-HCl buffer and stored in a freezer ($< 0^{\circ}\text{C}$). A glass-forming solution of glycerol and ethylene glycol (55:45 v/v) was added to all samples. OD_{825} was 0.2 to 0.4 for all samples. Details about the experimental setup were described elsewhere.¹⁹⁹ Briefly, absorption and HB spectra were measured by a Bruker HR125 Fourier transform spectrometer. For all absorption and HB spectra a spectral resolution of 4 cm^{-1} was used. Fluorescence spectra were collected, with a resolution of 0.1 nm, by a Princeton Instruments Acton SP-2300 spectrograph equipped with a back-illuminated CCD camera (PI Acton Spec10, 1340×400). The laser source ($\lambda = 496.5\text{ nm}$) for fluorescence and (nonresonant) HB spectra was produced by a Coherent Innova 200 argon ion laser. Laser power was set by a continuously adjustable neutral density filter. Experiments were performed at 5 K inside either a Janis 8-DT Super Vari-Temp liquid helium cryostat or an Oxford Instruments Optistat CF2 cryostat. Sample temperature was read and controlled with a Lakeshore Cryotronic model 330 or Mercury iTC temperature controller for the former and latter cryostats, respectively.

3.3 Results and Discussion

3.3.1. Absorption and Hole Burned spectra

An adequate theoretical description of the excitonic structure and EET dynamics in FMO complexes requires data obtained for intact protein complexes. However, the band positions (and peak intensity distribution) of low-temperature optical spectra of FMO from *C. tepidum* reported in the literature vary,^{116,163,200} although the changes were admittedly rather small ($\Delta\lambda \leq 1$ nm). The latter, however, does not mean that small shifts of the electronic transitions do not affect the dynamics of the studied protein system, e.g., the HB yield. For consistency, the three resolvable peaks will be referred to by the peak positions of the most redshifted spectrum: 826 nm, 816 nm and 805 nm peaks. It was observed that some peaks in the absorption spectra shifted continuously over time, even though samples were kept in a freezer and in the absence of light. That is, peak positions shifted to higher frequency with time. However, it was also found that some fresh samples had blueshifted absorption peaks; indicating that the peak position also depends on the sample preparation procedures. These data present a constraint on the interpretation of FMO optical spectra and their underlying electronic structure.

To illustrate this problem, we present low-temperature (5 K) absorption, fluorescence and HB spectra obtained for intact samples, whose 826 nm band positions are compared with data obtained for destabilized samples and previously reported results. As an example, Figure 3.1A shows absorption and nonresonant HB spectra for samples measured in 2009 (curve a) and 2012 (curve b). After one year the sample measured in 2009 had a shifted absorption spectrum similar to the fresh 2012 sample shown in Figure 3.1A. Thus, the FMO samples can destabilize over time or by preparation procedures but either way results in similar blueshifted absorption spectra. The observed blueshift in the Q_y absorption region from the 2009 sample (curve a) to the 2012 sample

(curve b in Figure 3.1A) is ~ 1 nm (15 cm^{-1}) for both the 826 and 816 nm peaks, which indicates the changes are occurring mainly to the two lowest energy absorption bands, as shown by the difference spectrum ($c = b - a$; red curve). Based on excitonic calculations reported previously,^{108,116,195,200} this spectral region is mostly contributed to by the two lowest energy excitonic states (vide infra), with some contribution from the third highest state also.

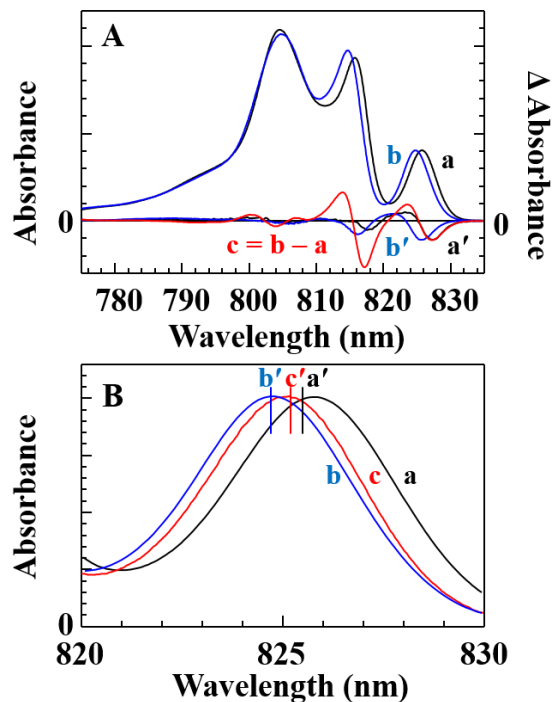


Figure 3.1 Frame A: curves a and b correspond to the absorption spectra obtained for FMO samples measured in 2009 and 2012, respectively. The difference between spectra is shown as curve c ($c = b - a$). Curves a' and b' are the saturated nonresonant HB spectra ($\lambda_B = 496.5$ nm) obtained for curves a and b, respectively. The spectra are normalized to the low-energy band/hole. Frame B: the two 825 nm bands for FMO samples shown above (curves a and b) as well as an absorption band measured in 2010 (curve c). The vertical lines mark the peak position of 825 nm bands reported in the literature (see text for details).

The lowest energy bands in the nonresonant holes shown in Figure 3.1 (curves a' and b') correspond to the lowest energy trap states of the FMO samples represented by absorption spectra a and b, respectively, since the NPHB rate is much smaller than both fluorescence and EET rates. Therefore, the shape of the “nonresonant hole origin” is nearly identical to the shape of the

emission origin spectrum.^{96,201} The higher energy bands observed in spectra a' and b' in Figure 3.1A are due to modified excitonic interactions when HB occurs in the lowest energy state of the excitonically coupled system. However, to explain the shape of emission and nonresonant HB spectra of FMO complexes, a downward uncorrelated EET between FMO trimer subunits has to be taken into account; however, this, as well as the description of the excitonic structure of the entire FMO trimer, is beyond the scope of this manuscript and will be discussed elsewhere.

Frame B in Figure 3.1 shows the low-energy bands of FMO (*C. tepidum*) samples measured at different times compared to peak positions reported in the literature (see the vertical lines, which mark the peak positions of 826 nm bands reported in the literature, i.e., 825.5 nm,¹⁶³ 824.7 nm²⁰⁰ and 825.2 nm¹¹⁶ for lines a'–c', respectively). Clearly, the experimental curves from this work accurately approximate the range of 826 nm band positions reported in the literature. The similar shifts of both the 826 and 816 nm bands indicate the possibility of spatially correlated environmental fluctuations. From excitonic calculations, the pigments contributing to these two bands are BChl *a* 3–5 and 7,^{108,116,195,200} all of which are likely influenced by the motions of the protein α helix 5.¹³⁶ Also, molecular dynamics simulations have shown correlations between the dipole couplings V_{45} and V_{57} (where V_{mn} is the coupling constant between pigments m and n).²⁰² A correlation of energy shifts could contribute to a short dephasing time²⁰³ and subsequent oscillations between the low-energy exciton states 1 and 2.¹⁹⁵

For nonresonant HB spectra shown in Figure 3.2, a burn frequency of 496.5 nm is used, and the lowest energy hole corresponds to the lowest exciton state. Figure 3.2 shows the development of holes under increasing fluence ($f = It_B$; where I is laser intensity and t_B is burn time) until saturation for samples measured in 2009 and 2012 (see Figure 3.1, curves a and b, respectively). The lowest energy hole position for the most intact FMO sample is 827.4 nm. The

HB spectra in Figure 3.2A are redshifted relative to the position of the corresponding steady-state absorption bands due to the presence of a relatively slow EET between the lowest energy states (mostly localized on BChl *a* 3) of the monomers of the trimer.²⁰¹

The destabilized FMO (2012 sample) has blueshifted holes, and in contrast to data shown in Figure 3.2 (frame A) the hole position (at 826.1 nm for low fluence, shallow hole) shifts to the blue as a function of fluence. That is, in this case the hole position is fluence dependent. This shift (~0.4 nm, relative to the low fluence hole) indicates that the blueshifted absorption spectrum is likely a mixture of intact and destabilized FMO complexes. A blueshift also occurs in the 816 nm hole, but is half (0.2 nm) that of the low-energy hole. Thus, the overall blueshift of both saturated holes (deepest holes of the 816 and 826 nm bands, curve a') is 1.7 nm when compared to the saturated hole positions of the 2009 sample (curve a, Figure 3.2A); showing, as did its corresponding absorption spectrum, a conserved shift between these two states. The latter suggests that more efficient bleaching occurs in the destabilized FMO sample. Since the intact FMO sample (measured in 2009) does not show any noticeable shift in the position of the low-energy hole over the course of burning, this suggests that the preparation is free of destabilized complexes. Interestingly, an absorption band at 826 nm has been observed in the FMO–RC complex and attributed solely to FMO absorption²⁰⁴ in agreement with our observations. In the FMO–RC preparations, pigments contributing to the lowest energy band (i.e., mainly BChl *a* 3) should not be destabilized due to binding of the RC. As such, this supports our assignment that intact complexes have a low-energy absorption band near 826 nm.

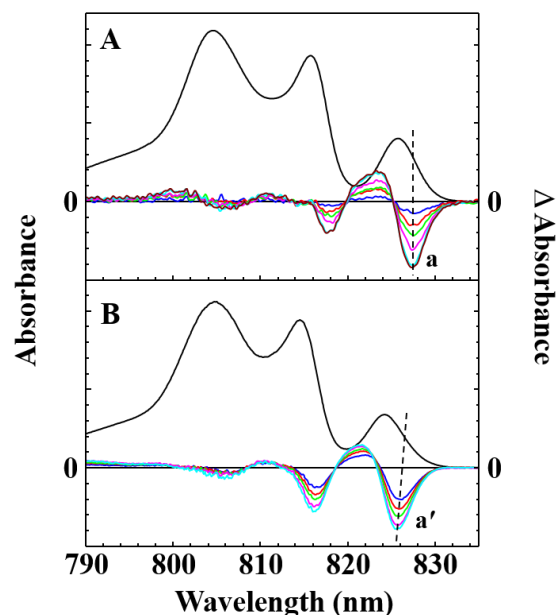


Figure 3.2 Absorption spectra and fluence dependent nonresonant HB spectra obtained with a burn wavelength (λ_B) of 496.5 nm. Dashed lines are included to guide the eye along the evolving hole position. Frame A: spectra for intact samples. Saturated hole (curve a) is located at 827.4 nm and all HB spectra are multiplied by 40. Frame B: spectra for destabilized samples. Saturated hole (curve a') is located at 825.7 nm and HB spectra are multiplied by 4.

To measure the HB efficiency of a system, the percent hole depth (defined for a specific wavelength as the ratio of absorbance change due to HB and original “preburn” absorbance) versus fluence is plotted for each hole burned. The resulting plot for three FMO samples with slightly different 826 nm band positions is shown in Figure 3.3. The destabilized sample (with the most blueshifted absorption spectrum) exhibits the largest relative HB efficiency; an effect that has also been reported previously for mixtures of CP47 photosynthetic complexes.²⁰⁵ This change in HB efficiency clearly indicates modified protein landscape tiers that are directly probed by HB spectroscopy. Thus, it cannot be excluded that the theoretical description of experimental data generated for FMO samples with contributions from destabilized proteins could also lead to a slightly modified excitonic structure and, in particular, modified EET dynamics. It appears that even though the sample measured in 2010 (from a different batch) has a blueshifted 826 nm band,

the HB efficiency would indicate that this sample is still mainly contributed to by intact FMO complexes. Thus the observed differences in shifts may not only be caused by destabilization but also by slightly different pH values, which are difficult to control. That is, it cannot be excluded that the net protein charge near low-energy pigments could change, leading to modified hydrophobic interactions,²⁰⁶ see also data shown in Figure 3.3 and 3.4.

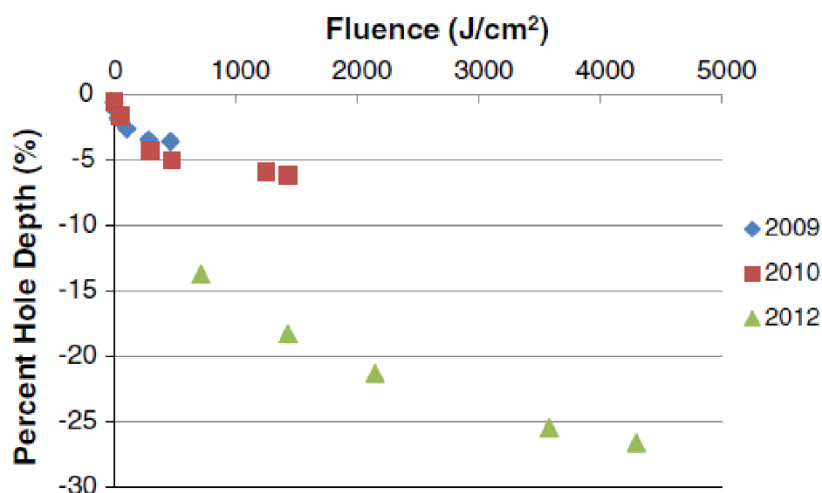


Figure 3.3 Percent hole depth plotted as a function of fluence (J cm^{-2}). Blue diamonds correspond to the most intact FMO complex, while red squares and green triangles represent complexes measured in 2010 and 2012, respectively.

To assess the contributions of intact and destabilized complexes measured for samples from the same batch, a simple spectral subtraction method was used. The analysis of the absorption (curve b) and HB spectrum (curve b') measured in 2012, shown in Figure 3.4, suggests possible contributions from intact (curve a) and destabilized (curve c) FMO proteins. The spectra measured in 2009 represent intact samples, while curves $c = b - a$ and $c' = b' - a'$ were obtained by subtraction after the corresponding spectra were normalized at the low-energy side of the 826 nm band. Curve c' shows the destabilized complexes are the main contributors to the saturated hole, as suggested above, being consistent with the much higher HB yield observed for blueshifted samples. We did

not attempt to deconvolve emission spectra, as the fluorescence quantum efficiency of intact and destabilized complexes is unknown.

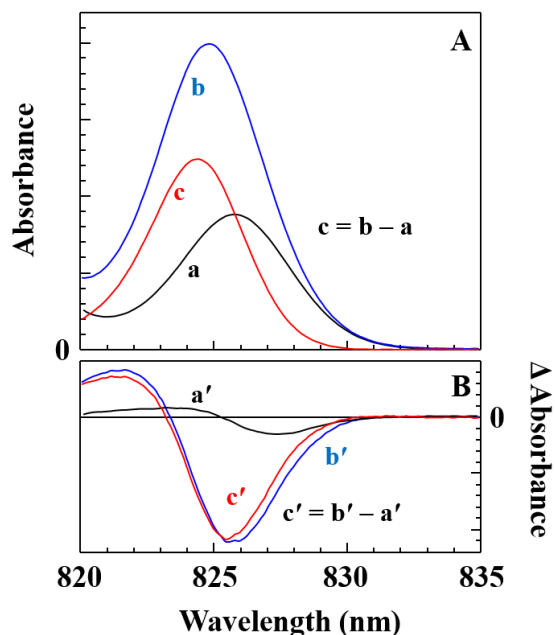


Figure 3.4 Frame A: 825 nm bands for 2009 measured sample (intact sample; curve a) and sample measured in 2012 (destabilized preparation; curve b) normalized at the low-energy absorption wing. Curve c corresponds to the difference spectrum ($c = b - a$), assigned as the absorption of destabilized proteins. Frame B: saturated nonresonant holes ($\lambda_B = 496.5$ nm) for the 2009 (curve a') and 2012 (curve b') samples normalized at the low-energy side of the nonresonant hole. Curve c' is the difference spectrum ($c' = b' - a'$) assigned to the bleach from destabilized complexes. Note the significant difference in HB efficiency.

It is not clear, however, by what mechanism this destabilization occurs, especially that similar blueshifts in peak position of the 826 nm band have been produced by oxidation with potassium ferricyanide and reduction with sodium dithionite (data not shown). Similar effects, though more pronounced due to higher concentrations, to those reported by Bina and Blankenship²⁰⁷ were observed in the 5 K lowest energy absorption. That is, the band shifts to 824.7 nm after the sample is treated with potassium ferricyanide; the same wavelength as the most destabilized sample found in both our data and the literature absorption spectra.^{200,208} Another possible mechanism, as eluded to above, includes changes to pH of the Tris-HCl buffer solution.

3.3.2. Reorganization and Site Energies

Figure 3.5 shows that the low-energy absorption and emission peaks measured in 2009 (frame A) and 2012 (frame B) shift by the same amount (~ 1 nm), which leads to conservation of the Stokes shift, and subsequently, E_λ . For weak el-ph coupling, E_λ can be approximated as half of the Stokes shift, leading to a E_λ of ~ 11 cm^{-1} from the experimental Stokes shift of ~ 22 cm^{-1} . The value of E_λ appears to be independent of sample age/preparation; however, comparing spectra from different batches, experiments and/or laboratories can lead to overestimated values of E_λ . This is illustrated in frame C of Figure 3.5 where the absorption spectrum (curve 2 from frame B) is plotted with the emission spectrum (curve 2 from frame A). This proves that comparison of spectra from different experiments can lead to incorrect conclusions about E_λ . Therefore, care must be taken to assess the quality of samples when comparing data.

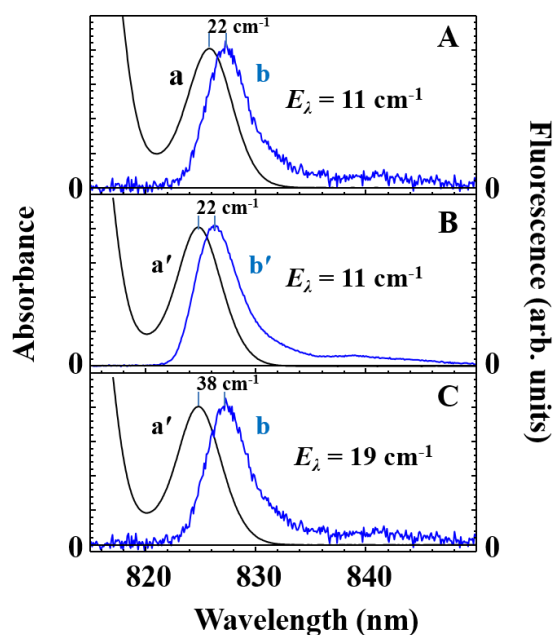


Figure 3.5 Frame A: absorption (curve a) and emission (curve b) spectra obtained for the intact (2009) sample. Frame B: absorption (curve a') and emission (curve b') obtained for the destabilized (2012) sample. In both frame the Stokes shift is conserved (see main text for details). Frame C: absorption (curve a') and emission (curve b) from frames A and B, showing that a comparison of spectra from different experiments leads to an incorrect E_λ value.

Regarding the value of E_λ , we note that this parameter can also be calculated from the spectral density (i.e., the weighted one-phonon profile) as

$$E_\lambda = \int_0^\infty \tilde{\nu} J(\tilde{\nu}) d\tilde{\nu} \quad (3.1)$$

However, the values can be highly dependent on the functional choice of the spectral density²⁰⁹ and scale linearly with S , which for various FMO complexes ranges from 0.3 to 0.5 in the literature.^{108,163,210,211} For completeness, Figure 3.6 shows the experimental Δ FLN spectrum¹⁶³ compared to the single-site spectrum calculated using a lognormal spectral density.²⁰⁹ From this spectral density and eq 3.1 E_λ ranges from 14.6 to 24.3 cm^{-1} for $S = 0.3\text{--}0.5$. In a similar manner, the shape of the spectral density can be roughly approximated from fits of the pseudo-PSBH found in resonant HB spectra. Calculating E_λ from simplistic fits to the pseudo-PSBH of FMO (data not shown) leads to values of 18.0–30.0 cm^{-1} for the same S values as above. All of the above suggests that the true value of E_λ is likely somewhere in the range of 15 to 25 cm^{-1} . While the experimental value derived from the Stokes shift is likely underestimated, it appears the often-used value of 35 cm^{-1} (e.g., in refs 116, 194, 212 and 213) is overestimated. This value was derived from fitting a partly destabilized absorption spectrum (lowest energy band of 825.2 nm) using an Ohmic spectral density. It should be noted that often when the OBO spectral density is used, the definition for E_λ includes a π term; meaning the values calculated in this work should be divided by π in order to be directly comparable.

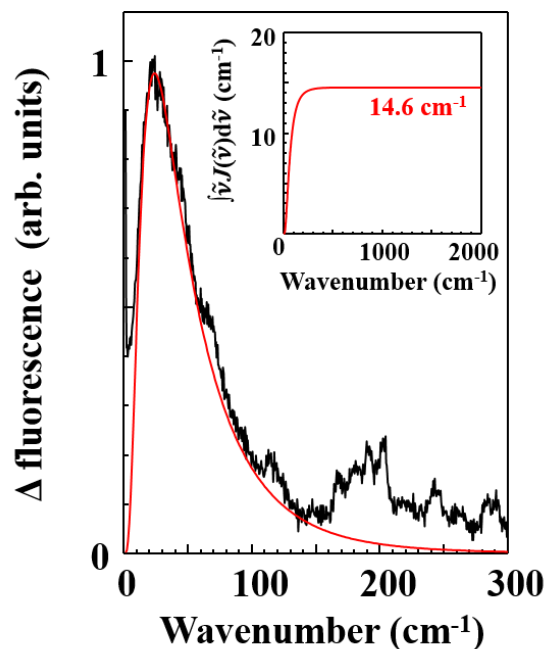


Figure 3.6 Experimental Δ FLN spectrum of Rätsep and Freiberg¹⁶ (black noisy curve, $\tilde{\nu}_{ex} = 12\,090\text{ cm}^{-1}$) compared to the single-site spectrum calculated with the lognormal spectral density of Kell et al.²⁰⁹ (red curve). The inset shows the integral of $\tilde{\nu}J(\tilde{\nu})$ assuming the $S = 0.3$.

Many sets of site energies listed in the literature are found from fits of optical spectra (ref 29 and references therein), although some attempts have been made to elucidate site energies from calculations based on the crystal structure.^{85,108,136} While comparisons would be easily accomplished if the entire absorption spectra shifted in concert, as seen in Figure 3.1 this is not the case as the 805 nm band, contributed to by several pigments, never appears to shift. Thus, not all sets of site energies are directly comparable even based on absorption spectra alone. However, as seen in Figure 3.5, comparison of absorption and emission spectra measured in different experiments (and/or for samples) can also lead to erroneous conclusions.

Regarding site energies of FMO pigments, the values of Adolphs and Renger¹⁰⁸ are often used when simulating 2DES cross peak oscillations^{214,215} and exciton populations.^{194,216} The site energies, specifically for *C. tepidum*, were derived from fits to the linear optical spectra of Vulto et al.,²⁰⁰ the absorption of which has a very blueshifted 826 nm band (824.7 nm). These parameters

cannot fit all of the spectra presented in this work, i.e., absorption for samples measured in 2009 and 2010. As mentioned above, the calculated absorption spectrum from which $E_\lambda = 35 \text{ cm}^{-1}$ was derived¹⁶ also had a blueshifted absorption peak and this sample was most likely a mixture of intact and destabilized samples, possibly exhibiting modified excitonic structure and EET dynamics. In fact, none of the published site energies for FMO (*C. tepidum*) can describe simultaneously absorption, emission, CD, LD, and transient HB spectra, suggesting that proper site energies have not been established as yet.

3.4 Conclusions

Based on our data, the low-energy absorption bands near 825 and 815 nm reported in the literature^{116,163,200} likely correspond to partly destabilized samples, which, if used in excitonic calculations, could lead to different parameter sets that should not be directly comparable to each other; that is, each set of site energies is dependent on sample preparation. Conserved shifts between absorption bands at 826 and 816 nm point towards correlated effects caused by the protein environment. Such effects have been shown theoretically to decrease the transfer rate to the lowest energy state and preserve coherence.^{217,218} Besides discrepancies in E_λ values used in the modeling of optical spectra for FMO (*C. tepidum*), the apparent peak shifts can also lead to a range of pigment site energies, which are important input parameters into energy transfer and lineshape calculations for excitonically coupled systems. Consideration of the sample preparation procedures when modeling optical spectra of FMO is critical for correct interpretation of the excitonic structure for both isolated proteins and complexes in vivo.

Acknowledgments

This work was supported by the Chemical Sciences, Geosciences and Biosciences Division, Office of Basic Energy Sciences, Office of Science, U.S. Department of Energy (Grant DE-FG02-11ER16281 to R.J). Authors are thankful to Mike Reppert (University of Chicago) and Dr. Valter Zazubovich (Concordia University) for fruitful discussions at the early stage of this work. FMO complexes were kindly provided by Dr. Jianzhong Wen (Washington University in St. Louis).

Chapter 4

On the Controversial Nature of the 825 nm Exciton Band in the FMO Protein Complex

Adam Kell,[†] Khem Acharya,[†] Valter Zazubovich,[§] and Ryszard Jankowiak^{†,‡}

[†]Department of Chemistry and [‡]Department of Physics, Kansas State University, Manhattan,
Kansas 66506, USA

[§]Departments of Physics, Concordia University, Montreal H4B 1R6, Quebec, Canada

Reproduced from the *Journal of Physical Chemistry Letters* **2014**, *5*, 1450–1456

Copyright 2014 American Chemical Society

Abstract

The nature of the low-energy 825 nm band of the FMO protein complex from *C. tepidum* at 5 K is discussed. It is shown, using hole-burning spectroscopy and excitonic calculations, that the 825 nm absorption band of the FMO trimer cannot be explained by a single electronic transition or overlap of electronic transitions of non-interacting pigments. To explain the shape of emission and nonresonant HB spectra, downward uncorrelated EET between trimer subunits should be taken into account. Modeling studies reveal the presence of three sub-bands within the 825 nm band, in agreement with nonresonant HB and emission spectra. We argue that after light induced coherences vanish, uncorrelated EET between the lowest exciton levels of each monomer takes place. HB induced spectral shifts provide a new insight on the energy landscape of the FMO protein.

4.1 Introduction

The FMO protein of GSB is a long studied pigment-protein complex which funnels energy from the chlorosome to the RC.^{27–29} This complex continues to be of great interest due to observed quantum effects, which were suggested to be responsible for the very high efficiency of EET in photosynthetic antenna complexes.^{43,44} Until recently it was believed that each monomer of the FMO trimer binds seven BChl *a* molecules. Recently X-ray diffraction and mass spectrometry data have confirmed the presence of an additional pigment (BChl *a* 8) located at the monomer connection regions with partial occupancy.^{35,37,40} While there are multiple assignments of pigment site energies in the literature, it is well accepted that BChl *a* 3 and 4 contribute mostly to the lowest excitonic state in each monomer.^{116,195,200,217}

There is a remarkable amount of experimental and theoretical papers related to the topic of excitonic structure of FMO, its vibrational environment, and the origin of measured^{43,44} and simulated^{108,116,194,219,220} long-lived quantum coherences. However, usually only the monomer is taken into account in simulations of excitonic structure,²⁰³ energy transfer pathways^{221–224} and non-Markovian noise correlation effects.²²⁵ This is in spite of a number of previously published experimental data obtained by HB spectroscopy,^{210,226} Δ FLN,^{163,227} pump-probe spectroscopy,^{228–230} photon echo experiments²³¹ and triplet minus singlet (T–S) measurements,²³² as well as theoretical modeling,²³³ which all suggested the possibility of intermonomer energy transfer in FMO proteins. Additionally, a very recent study considered three identical SDFs for the 825 nm band. In this simple model it was assumed that the three states are localized on BChl *a* 3 only. The results also suggested that EET should be taken into account to explain the shapes of both resonant and nonresonant HB spectra.¹³¹ In this work, using a model that incorporates excitonic interactions, we further challenge the present consensus^{29,203} that the low-energy 825 nm

band can be properly described by a single excitonic state. We focus on the nature of the lowest energy absorption band of FMO complexes from *C. tepidum* which remains controversial.

The above mentioned consensus is due to the fact that most authors in recent years have argued that the intersubunit coupling between BChl *a* 3 is too weak to warrant consideration for the entire trimer. However, Förster theory^{110,111} predicts that energy transfer on the order of picoseconds is possible even for very weak ($|V| < 5 \text{ cm}^{-1}$) electronic coupling between chromophores. The coupling constant between BChl *a* 3 and 4 (the lowest energy pigments within a monomer) is -53.5 cm^{-1} , when calculated from the crystal structure (PDB ID: 3ENI)³⁵ using the TrEsp method⁸⁷ and assuming a Q_y transition dipole strength of 25.2 D^2 (effective dipole strength includes the influence of the dielectric constant). In this case the coupling between BChl *a* 3 pigments and BChl *a* 4 pigments located in various monomers is -2.5 and 2.5 cm^{-1} , respectively. It has been previously proposed that the three bands underlying the 825 nm absorption band may correspond to three transitions shifted by 20 cm^{-1} .²³⁴ This model has not been accepted, as one would have to assume different site energies for each monomer, an unlikely scenario. In addition, the Monte Carlo simulations did not provide downward EET rates consistent with the resonant HB spectra.²³⁴ In contrast, we propose that the average site energies of BChls in each monomer are the same, but disorder causes the energies to vary between the three monomers of the trimer.

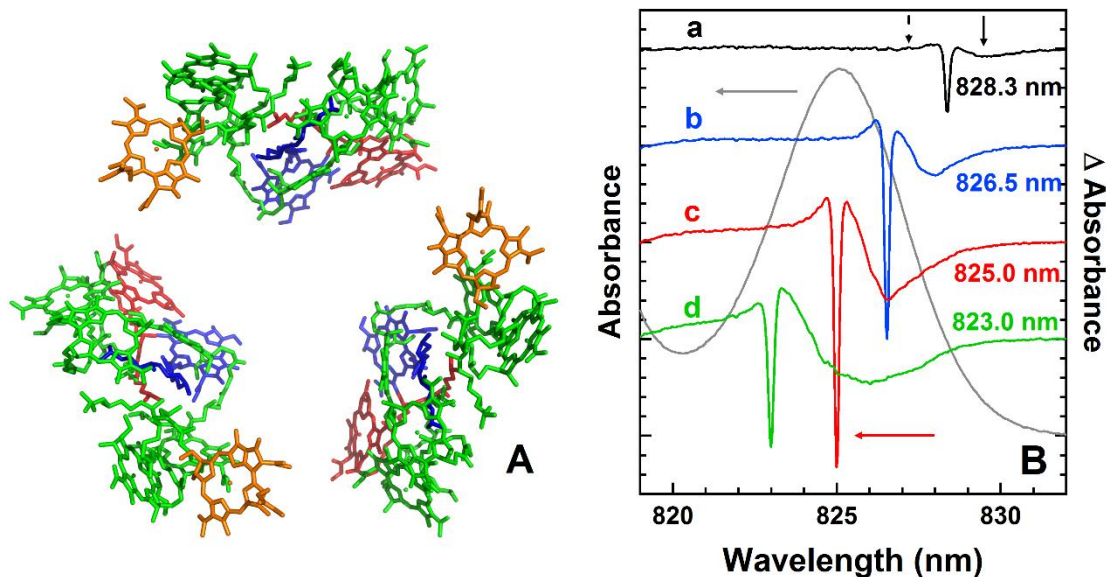


Figure 4.1 Frame A: structure of the FMO trimer showing the orientation of BChl *a* pigments. BChl *a* 3, 4 and 8 are colored blue, red and orange, respectively. Frame B: resonant HB spectra burned within the 825 nm band. Spectra a–d were obtained with $\lambda_B = 828.3, 826.5, 825.0$ and 823.0 nm, respectively, and are shifted for clarity. The dashed and solid arrows mark the real- and pseudo-PSBHs, respectively, while the red arrow indicates (as an example) the intense ZPH for curve c. The grey curve is the absorption band.

4.2 Results and Discussion

Figure 4.1 shows the 825 nm absorption band (grey curve) and four resonant NPHB spectra obtained for $\lambda_B =$ of 828.3, 826.5, 825.0 and 823.0 nm, curves a–d, respectively. All holes were obtained with a fluence of 120 J cm^{-2} ; the percent hole depths of curves a–d are 65.0%, 66.7%, 59.5% and 47.4%, respectively. Although the resolution of these resonant holes is 1 cm^{-1} , we purposely burned deeper holes to demonstrate the presence of EET between subunits. Therefore, the widths of our ZPHs are power broadened. However, high-resolution (shallow) holes (using low fluence; hole depth $< 10\%$) were reported elsewhere, where the estimated lifetimes of the Q_y states also indicated downward EET.^{210,226} The shapes of the entire HB spectra in Figure 4.1 (curves a–d) also indicate the presence of downward energy transfer between FMO monomers.

That is, low-energy satellite hole features are significantly more enhanced than would be warranted if EET was not present.

The narrow deepest holes are the resonant ZPHs coincident with λ_B , with pseudo- and real-PSBHs located $\sim 22 \text{ cm}^{-1}$ to the red and the blue, respectively. A similar phonon frequency of 22 cm^{-1} was observed by Matsuzaki et al.²²⁶ in FMO complexes from *Pr. aestuarii*. The spectra in Figure 4.1 clearly establish the existence of EET in that the bleaching to the lower energies with respect to the ZPHs is indicative of energy acceptors, not purely the pseudo-PSBHs as would be expected if the band was composed of a single exciton state. Thus, the pseudo-PSBHs are not well resolved in spectra b–d due to a broad contribution from downward EET, as pigments in different sub-SDFs, as discussed below, are burned due to direct transfer from the highest energy pigment subpopulation to the lowest energy subpopulation. That is, assuming the 825 nm band is composed of a single exciton state (no intraband EET and weak el-ph coupling), the pseudo-PSBH of curve d would be much narrower. Thus, our data indicates the presence of intermonomer EET. Therefore, in contrast to ref 234, where it was assumed that the 825 nm band is contributed to by three equi-spaced states (20 cm^{-1}) with widths of 50 cm^{-1} , we propose a model with identical SDFs for each monomer (not equi-spaced sub-bands) in which downward energy transfer between identical trimer subunits is taken into account.

More specifically, we suggest that not only the whole trimer has to be considered in simulations of optical spectra, but the presence of uncorrelated EET between the FMO monomers must be considered to explain both resonant and nonresonant HB spectra. Due to disorder and EET between BChl *a* 3 pigments (and in part BChl *a* 4 molecules, which have a small probability be the lowest energy pigments) in the three monomers, one sub-band of the 825 nm band should correspond to the lowest energy pigments in the trimer (that cannot transfer energy), with the

second sub-band (shifted blue) corresponding to pigments that serve as an acceptor and donor, and the last sub-band corresponding to the highest energy pigments that efficiently transfer energy to the two lower energy acceptors (the two lowest energy subpopulations of BChls) within the trimer. Throughout this work we refer to these sub-bands (and pigments contributing to them) as sub-bands 1, 2 and 3; with band 1 being lowest in energy and band 3 being highest in energy. Thus, we assume that due to uncorrelated EET between subunits the excitation energy can be transferred to either one of the energy acceptors and the process is competitive. This, as mentioned above, should lead to three sub-SDFs within the 825 nm absorption band, as illustrated below.

Regarding HB, pigments in resonance with narrow-band laser excitation may undergo a reaction (PHB) or experience rearrangement of the local environment (NPHB).^{96,196} These changes are reflected in HB spectra, which are the difference between absorption spectra measured before and after laser excitation. The resulting holes are persistent, meaning the holes are only removed by raising the temperature of the sample. For nonresonant HB, persistent holes are formed after energy relaxation to the lowest exciton states and the holes reflect the shape of the emitting state. Thus, in FMO, the pigments contributing to sub-band 1 will be burned first, as HB yield depends on the excited state lifetime. However, a partial bleaching of sub-band 2 cannot be entirely excluded. That is, some bleaching of higher-energy pigments occurs because their HB yield is small but not zero; and once some sub-band 1 pigments experience NPHB, pigments that used to contribute to sub-band 2 become lowest-energy, and their HB yield increases.

Table 4.1. Hamiltonian for reduced structural model of FMO from *C. tepidum*

BChl <i>a</i>	3A	4A	3B	4B	3C	4C
3A	12 155	-53.5	-2.5	5.7	-2.5	0.5
4A		12 245	0.5	2.5	5.7	2.5
3B			12 155	-53.5	-2.5	5.7
4B				12 245	0.5	2.5
3C					12 155	-53.5
4C						12 245

Site energies and dipole coupling matrix elements are in units of cm^{-1} . BChl *a* 3 and 4 pigments from different monomers are designated as A, B and C.

In modeling of absorption, emission, and HB spectra we assume that the lowest states of all three monomers have the same SDFs. To fit the 825 nm exciton band, emission band and low-energy hole, a reduced structural model is used (i.e., a trimer of BChl *a* 3 and 4 pigments) as, based on our calculations for the entire trimer²³⁵ (see Chapter 5) and literature data,^{116,195,200,217} BChl *a* 3 mostly contributes to the lowest energy exciton with minor contributions from BChl *a* 4. Our excitonic modeling studies of various optical spectra revealed that the site energies for BChl *a* 3 and 4 are 12 155 and 12 245 cm^{-1} , respectively; with an inhomogeneous broadening (FWHM) of 90 cm^{-1} . The site energies apply to the structural model used in this work, as the site energy for BChl *a* 4 may change slightly when interactions with other pigments are included. The Hamiltonian used for the reduced structural trimer model of FMO is shown in Table 4.1. BChl *a* 3 and 4 pigments from different monomers are designated as A, B and C. For monomer calculations (i.e., no intermonomer EET present), see Figure 4.2B, in order to fit the 825 nm absorption band the site energies of both pigments were redshifted by 5 cm^{-1} . The solid (black) spectra in Figure 4.2 correspond to the experimental absorption, emission and the persistent nonresonant HB spectra, all obtained for *C. tepidum*. The corresponding noisy red (frame A) and blue (frame B) curves are the calculated spectra with and without EET between monomer subunits,

respectively. Intramonomer interactions were modeled using Redfield theory,^{100,101} with Förster energy transfer occurring between lowest energy molecules of various monomers.

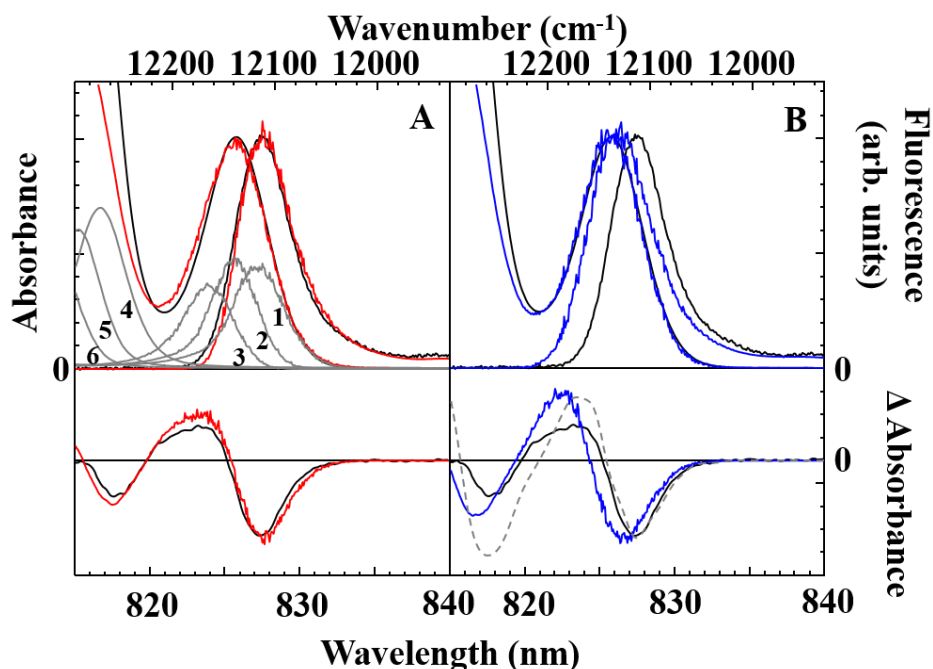


Figure 4.2 Frame A: Calculated (red) absorption, emission and HB ($\lambda_B = 496.5$ nm; fluence = 468 J cm^{-2} ; hole depth at 827 nm = 3.6%) spectra for a trimer model with EET compared to experiment (black). Grey curves are the calculated exciton states. Frame B: Spectra calculated assuming no EET between monomers (blue) compared to experiment (black). The grey dashed curve is the calculated HB spectrum assuming no 60 cm^{-1} shift after burning. HB spectra are offset for clarity.

The importance of lifetime broadening (using the Redfield theory) was already demonstrated by modeling of HB spectra for various model dimers with weak el-ph coupling ($S < 1$).¹⁴¹ Though for stronger el-ph coupling strength ($S > 1$), different lineshape theories must be employed, as suggested in refs 236, 237 and 239, the Redfield approach is an appropriate approximation for systems with low el-ph coupling strength, i.e., for modeling various optical spectra of FMO complexes. In order to address the nature of the 825 nm band of FMO complexes we applied a combination of Redfield and Förster theories to FMO complexes, simultaneously modeling absorption, emission, and nonresonant HB spectra taking into account the uncorrelated

EET between FMO monomers. That is, the exciton energies and lineshapes (including lifetime broadening) were modeled with Redfield theory as described previously,^{99,141} while energy transfer rates between the lowest energy pigments of each monomer were calculated using the Förster theory.^{110,111}

We used the spectral density for *C. tepidum* FMO from ref 209 which critically assessed the widely used spectral density functions. The above parameters were used in calculations of absorption, emission, and HB spectra; which are calculated for 50 000 complexes using a Monte-Carlo approach, with site energies chosen randomly according to the SDF. *S* factor of 0.4 was used and the effective *S* value (due to a small amount of delocalization) for the lowest excitonic state is 0.3, in agreement with previous Δ FLN data measured on the low-energy side of the 825 nm band.¹⁶³ E_{λ} for the lowest energy state is about 12 to 14 cm^{-1} , in agreement with our experimental data,²⁴⁰ and not 35 cm^{-1} as widely used in the theoretical calculations.^{116,194,212,213} The monomer calculations (frame B) cannot account for the positions of nonresonant holes or the emission spectrum, which is also too broad. The grey dashed curve in frame B is the calculated HB spectrum assuming no 60 cm^{-1} shift of the antihole (vide infra). While the hole positions are now more correct compared to experiment, the depth of the high-energy hole (\sim 817 nm) is too large. Thus, the focus is placed on calculations assuming EET between monomer subunits, which explain the experimental optical spectra more convincingly. The calculated emission (frame A) is slightly redshifted due to the assumption that only the lowest state emits. However, the experimental emission spectrum could also possess a small contribution from a fraction of pigments contributing to sub-band 2, because for small coupling and, for example, EET on the order of 100 ps, sub-band 2 could also emit directly, albeit with reduced probability, even if sub-band 1 is not bleached.

The grey curves in frame A of Figure 4.2 represent the calculated excitonic states, with the three grey sub-bands of the 825 nm absorption band (curves 1–3) corresponding to sub-bands 1, 2 and 3, respectively. The peak positions of these sub-bands are 827.2, 825.6 and 823.8 nm. The calculated nonresonant HB spectrum, as expected, is a result of NPHB of the lowest energy state of FMO, whose shift results in redistribution of oscillator strength at various wavelengths. The agreement with experimental data suggests that BChl *a* 3 and 4 are indeed the main pigments contributing to the lowest energy exciton state, in agreement with refs 116, 195, 200 and 217. Modeling studies revealed that BChl *a* 5 and 7 do not contribute to the lowest energy band/hole, as these pigments have negligible excitonic interaction with BChl *a* 3. The best fit of the nonresonant hole in frame A was obtained assuming a 60 cm⁻¹ blueshift of postburn site energies; that is, after burning the site energy is shifted, on average, by 60 cm⁻¹ to higher energy (see Figure 4.2).

Regarding the shape of the resonant HB spectra (see Figure 4.1), it is well known^{96,241} that the antihole (for low-dose HB spectra) is not uniformly distributed over the whole absorption band, rather it is typically distributed over the much narrower range both to the blue and to the red (by ~10 cm⁻¹) of the ZPH, though larger blueshifts are also observed.⁹⁶ The latter indicates the presence of different tiers in the protein energy landscape. For example, data shown in Figure 4.1 show that the antihole absorption is peaked at about 5–10 cm⁻¹ to the blue and to the red of λ_B . Interestingly, the higher dose nonresonant HB spectrum shown in Figure 4.2 shows a larger average shift (~60 cm⁻¹) of the antihole with respect to the main bleach. Similar behavior was observed for B800 BChl *a* molecules in the LH2 antenna complex of *Rhodospseudomonas acidophila*.²⁴¹ Thus HB spectroscopy provides averaged magnitudes of light-induced spectral shifts, most likely probing two different tiers of the protein energy landscape. Similar ranges of

spectral shifts were directly observed by a single photosynthetic complex study for B800 BChl *a* in *Rhodospirillum rubrum*.²⁴² The latter paper also discusses possible origins of various spectral shifts within the tiers of the potential energy hyper surface of a protein.

Figure 4.3 shows the contribution to the 825 nm absorption band (curve a) from pigments 3 (curve b) and 4 (curve c). Curves b' and c' illustrate their contribution to the nonresonant hole (curve a'). The sum of spectra b' and c' provides the calculated hole (red curve) shown in Figure 4.2 (frame A). The lowest energy excitonic state (with a maximum near 827.2 nm) has a relative oscillator strength of ~0.86 BChl *a*, with largest contributions from BChl *a* 3 (80%). The delocalization length (inverse participation ratio) of the lowest excitonic state (sub-band 1) is 1.5. However, in our reduced structural trimer model we have six excitonic states labeled as 1–6 in Figure 4.2A; thus, the oscillator strength for the remaining five exciton states in the BChl *a* 3/BChl *a* 4 trimer (i.e., three monomer subunits with the above mentioned two pigments) are: 0.81, 0.67, 1.40, 1.15, and 1.06. We hasten to add that excitons 4–6 (in our reduced FMO model) are mostly contributed to by BChl *a* 4 (~ 80%) and BChl *a* 3 (~ 20%), though in calculated spectra for the entire trimer the second exciton state is also in part contributed to by pigments 5 and 7 (see Chapter 5). Since only pigments 3 and 4 contribute to the 825 nm absorption band, our reduced structural model suffices to properly describe the 825 nm absorption, emission, and nonresonant HB spectra.

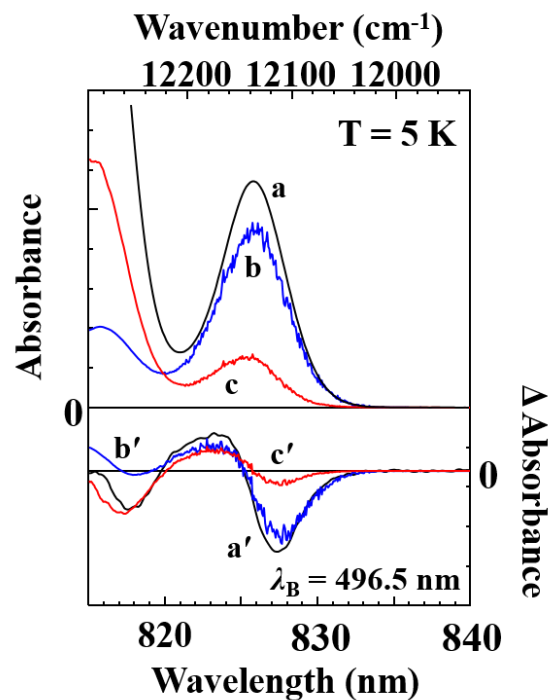


Figure 4.3 Spectra a and a' (black curves) are the absorption and nonresonant spectra ($\lambda_B = 496.5$ nm). Spectra b/b' and c/c' represent the contributions from BChl *a* 3 and 4, respectively. The corresponding occupation numbers for BChl *a* 3 and 4 to the 825 nm absorption band are 80% and 20%, respectively.

Figure 4.4 shows distributions of the relaxation times for sub-band 2 (frame A) and sub-band 3 (frame B) pigments, calculated with Förster theory for $V_{33} = -2.5$ cm⁻¹. The lowest energy pigment of each monomer is assumed to be BChl *a* 3. While the average relaxation time for sub-band 2 (positioned at 825.6 nm) is 70.0 ps, the distribution peaks at 32 ps. Likewise, the average and peak times for sub-band 3 are 41.3 and 20 ps, respectively. The average relaxation times assuming the lowest energy pigment in one monomer of the trimer is BChl *a* 4 are 26.4 and 20.3 ps for sub-bands 2 and 3, respectively (data not shown). Recall that BChl *a* 4 contributes only 20% to the lowest energy band. It should be noted that in general Redfield theory predicts faster transfer rates (data not shown), as mentioned in ref 237. Previously reported experimental (high-resolution) resonant holes burned at $\lambda_B = 822.8/824.8$ nm (in *Pr. aestuarii*) and 823.0/825.0 nm

(in *C. tepidum*) suggested the presence of downward energy transfer in the 825 nm absorption band.^{226,243} In those papers, the observed average relaxation time of 37 ps, i.e., EET time obtained from $\lambda_B = 823.0$ nm, is in reasonable agreement with our finding (vide supra), in particular, when the distribution of EET times is taken into account. However, based on our data it is difficult to estimate the average relaxation time for the middle of the 825 nm band (i.e., $\lambda_B = 825.0$ nm), as at this wavelength there are contributions from sub-bands 2 and 3, as well as the trap states that do not transfer energy (i.e., sub-band 1). The 37 ps component was also found in the kinetic measurements for FMO complexes (*Pr. aestuarii*) and was attributed to energy transfer between subunits of the FMO trimer,^{118,231} in agreement with our data. The previously observed time-dependent redshift of the FMO emission spectrum, where the ~30 ps time constant was related to energy transfer in the protein trimer between monomer subunits²⁴⁴ is also consistent with our model. Finally, studies focused on slower processes taking place in FMO complexes, both at room and 77 K temperatures, found that a complete spectral equilibration in FMO proteins occurs in about 26 ps,²³⁰ which again is likely due to equilibration within the trimer caused by the uncorrelated EET discussed above.

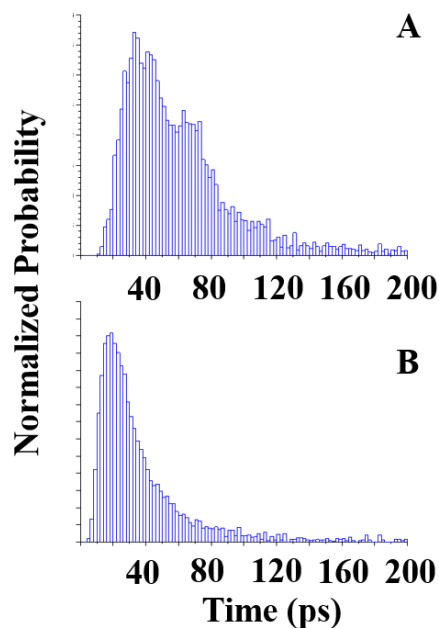


Figure 4.4 Distributions of Förster transfer times for pigments contributing to sub-band 2 (frame A) and sub-band 3 (frame B). Obtained for $V_{33} = -2.5 \text{ cm}^{-1}$ (i.e., for the coupling between BChl *a* 3 pigments located in various monomers). The probabilities are normalized over 50 000 iterations (i.e., the sum of all probabilities is 1).

4.3 Conclusions

In summary, as argued above, the HB spectra and modeling studies, along with previously reported data,^{163,210,226–232} clearly indicate the existence of EET within the lowest absorption band of the FMO complex. Thus, in contrast to the presently accepted consensus^{29,203} (suggesting that only one monomer can be used to describe linear optical spectra), we conclude that each trimer has three identical (degenerate) SDFs from the three monomers connected by Förster EET. Therefore, the 825 nm band in the FMO protein cannot be explained for by a single electronic transition. That is, for the very weak el-ph coupling observed ($S \sim 0.3$),¹⁶³ the broad and structured holes in Figure 4.1 cannot be explained by standard EET-free HB theory.⁹⁶ Also, the dependence of S across the 825 nm band observed in refs 163 and 227 is consistent with uncorrelated EET between monomers of the FMO trimer. Finally, our findings are also consistent with the shapes of

the vibronically excited FLN spectra (data not shown for brevity), in which only very weak ZPLs were superimposed on a broad fluorescence origin band, clearly supporting the EET within the FMO trimer.

We have demonstrated, using HB spectroscopy, that the 825 nm absorption band of the FMO trimer cannot be explained by a single electronic transition. To explain the shape of emission and nonresonant HB spectra, downward uncorrelated EET between trimer subunits should be taken into account. Of course uncorrelated EET between monomers is preceded by downward energy relaxation along the “excitonic energy ladder” in each monomer on a femtosecond time scale.^{41,244} We propose that after light induced coherences vanish, uncorrelated EET between the lowest by exciton levels of each monomer takes place due to static structural inhomogeneity in the trimer leading to equilibration within the trimer that takes several tens of picoseconds.

Acknowledgments

This work was supported by the Chemical Sciences, Geosciences and Biosciences Division, Office of Basic Energy Sciences, Office of Science, U.S. Department of Energy (Grant No. DE-FG02-11ER16281 to R.J.). We thank Drs. Robert E. Blankenship and Jianzhong Wen (Washington University in St. Louis) for providing the FMO samples and Mike Reppert (University of Chicago) for helpful discussions during the early stage of this project. We acknowledge Dr. Chen Lin for the measurements of vibronically excited FLN spectra. V.Z. acknowledges support of NSERC Discovery grant.

Chapter 5

Effect of Spectral Density Shapes on the Excitonic Structure and Dynamics of the Fenna-Matthews-Olson Trimer from *Chlorobaculum tepidum*

Adam Kell,[†] Robert E. Blankenship,[§] and Ryszard Jankowiak^{†,‡}

[†]Department of Chemistry and [‡]Department of Physics, Kansas State University, Manhattan,
Kansas 66506, USA

[§]Departments of Chemistry and Biology, Washington University in St. Louis, St. Louis, Missouri
63130, USA

Abstract

The FMO trimer (composed of identical subunits) from the GSB *C. tepidum* is an important protein model system to study exciton dynamics and EET in photosynthetic complexes. In addition, FMO is a popular model for excitonic calculations, with many theoretical parameter sets reported describing different linear and nonlinear optical spectra. Due to fast exciton relaxation within each subunit, intermonomer EET results predominantly from the lowest energy exciton states (contributed to by BChl *a* 3 and 4). Using experimentally determined shapes for the spectral densities, simulated optical spectra are obtained for the entire FMO trimer. Simultaneous fits of low-temperature absorption, fluorescence and HB spectra place constraints on the determined pigment site energies; providing a new Hamiltonian that should be further tested to improve modeling of 2DES data and our understanding of coherent and dissipation effects in this important protein complex.

5.1 Introduction

The FMO protein complex is found mainly in GSB and facilitates EET from light-harvesting chlorosomes to the RC.^{28,29} It was the first pigment–protein complex to have the crystal structure determined³³ and X-ray crystallography data for FMO from several GSB are available,^{35,38,39} which reveal very similar features for FMO of *C. tepidum*, *Pr. aestuarii* and *Pl. phaeum*. That is, FMO is a homotrimer with each monomer binding seven to eight BChl *a* pigments enclosed in a series of β sheets. The existence of BChl *a* 8 was discovered more recently³⁷ and its occupancy in isolated complexes is known to vary.^{35,38,40}

The wealth of crystallography data on FMO is particularly appealing for structure-based calculations. Recent studies have been undertaken to calculate pigment site energies based solely on Chl conformations using quantum chemical and optimization approaches.^{245,246} While such atomistic studies represent important advances in structure-based modeling, the reported energies (and ordering) for FMO²⁴⁵ cannot explain experimental data as of yet. However, such studies reveal that site energies critically depend on the protein binding pocket and pigment conformations. Therefore, at this point the best approach for elucidating site energies is simultaneous calculations of optical spectra using an optimization algorithm (vide infra).

Much of the interest in FMO is due to the results of pump-probe and 2DES measurements, where quantum beats were observed in the 19 K polarized pump-probe signal⁴² and 2D maps at 77 K⁴³ and room temperature.⁴⁴ The relaxation of localized and delocalized states can be treated by Förster^{111,112} and Redfield^{99–101} theories, respectively. Since photosynthetic complexes often fall within an intermediate regime between the two limits of weak and strong coupling, various other theoretical methods have been proposed, often with FMO as a model system. For example, Redfield,^{85,108,220} modified Redfield,¹¹⁶ correlated driving-dissipation equation,²⁴⁷ zeroth order

functional expansion master equation,^{173,213} equation-of-motion phase-matching,²⁴⁸ hierarchical equations-of-motion,^{183–185,194} and numerical path integral^{216,249} approaches have been applied in the interpretation of population dynamics and coherent oscillations involved in EET within FMO.

While fast timescale kinetics (on the order of femtoseconds) can be described with only intramonomer exciton relaxation, intermonomer EET is important when considering steady-state and frequency-domain spectra, e.g., fluorescence and HB spectra.²⁰¹ In order to generate the most physically realistic Hamiltonian possible, as many constraints need to be placed on the fitting process as possible. That is, the entire trimer has to be taken into account in order to properly describe various optical spectra simultaneously.^{131,201} For example, linear absorption spectra have been shown to differ for various FMO complexes reported in the literature,²⁴⁰ suggesting that site energies generated from simulations of only absorption spectra can vary for different samples or laboratories.

In this work, Redfield theory is applied in order to generate an optimized Hamiltonian for the FMO trimer from *C. tepidum*. Since the intermonomer dipole coupling is weak, Generalized Förster theory^{114,115} is used to describe three excitonic domains (corresponding to the pigments bound by each protein subunit). That is, exciton delocalization is restricted to a single domain and interdomain EET between lowest energy excitons of each domain is described by the Förster rate equation.^{111,112} However, BChl *a* 8 is included in the domain of the neighboring protein monomer, as this pigment has a larger intermonomer coupling constant with BChl *a* 1 of the adjacent subunit than any intramonomer couplings.

5.2 Theory

Simulated spectra are calculated following Generalized Förster theory,^{114,115} with exciton lineshapes and relaxation within excitonic domains described by a non-Markovian density matrix

approach.⁹⁹ Exciton delocalization is restricted to three distinct domains with each domain corresponding to the pigments bound by a protein subunit (with the exception for BChl *a* 8 mentioned above). BChl *a* atomic coordinates are taken from the X-ray structure (PDB ID: 3ENI)³⁵ and included full occupancy of BChl *a* 8.⁴⁰ Electronic coupling constants are calculated using the TrEsp method⁸⁷ with an effective transition dipole strength $|\mu|^2 = 25.2 \text{ D}^2$ (which includes contributions of the relative dielectric of the medium).^{108,201}

The spectral density (weighted one-phonon profile) is assumed to be a lognormal distribution.²⁰⁹ For the lowest energy state, the spectral density shape is determined from Δ FLN data,¹⁶³ with $\tilde{\nu}_c = 38 \text{ cm}^{-1}$, $\sigma = 0.7$,²⁰⁹ and $S = 0.4$, where $\tilde{\nu}_c$, σ and S correspond to the cutoff frequency, standard deviation, and Huang-Rhys factor, respectively. For higher energy pigments, a broader spectral density shape is used, i.e., $\tilde{\nu}_c = 45 \text{ cm}^{-1}$, $\sigma = 0.85$ (vide infra). In addition, BChl *a* ground state vibrational modes determined from the Δ FLN spectrum were included in the lineshape ($S_{vib} = 0.4$).¹⁶³

The FWHM of inhomogeneous broadening for BChl *a* 3 (75 cm^{-1}) is constrained by the width of the 825 nm absorption and fluorescence (0,0)-bands. All other BChl *a* have FWHM of 125 cm^{-1} , in order to better fit the high-energy absorption features. Pigment site energies are adjusted to provide simultaneous fits to absorption, fluorescence and persistent nonresonant HB spectra. In order to optimize the fits to experimental data, a Nelder-Mead simplex²⁵⁰ algorithm was utilized to search the solution space and minimize the root-mean-square deviation

$$\text{RMSD} = \sqrt{\frac{\sum_{i=1}^N (y_i^{theo} - y_i^{exp})^2}{N}}, \quad (5.1)$$

where N is the total number of compared points.

HB spectra were best fit assuming a 60 cm^{-1} blueshift of the post-burn site energy distributions,^{131,201} suggesting that the main energy tier in the FMO protein energy landscape is about 60 cm^{-1} . The spectral contributions of BChl *a* pigments to the absorption spectrum can be calculated according to¹⁰⁸

$$d_m(\tilde{\nu}) = \tilde{\nu} \left\langle \sum_M |c_{mM}|^2 D_M(\tilde{\nu}) \right\rangle_{dis}, \quad (5.2)$$

where $D_M(\tilde{\nu})$ is the lineshape of exciton state M , $|c_{mM}|^2$ is the contribution number (squared eigenvector coefficient) of site m to state M , and $\langle \dots \rangle_{dis}$ indicates disorder averaging. The contribution numbers also define the delocalization length (inverse participation ratio) by

$$L_M = \frac{1}{\sum_M |c_{mM}|^4}. \quad (5.3)$$

5.3. Results and Discussion

Structure-based calculations and simultaneous fits of absorption, fluorescence and persistent nonresonant ($\lambda_B = 496.5 \text{ nm}$) HB spectra, including uncorrelated EET between monomers, provides a method of elucidating BChl *a* site energies (Table 5.1). The shape of the HB spectra was independent of laser fluence used (i.e., no shift of the lowest energy bleach was observed), indicating that this FMO sample was intact and not a mixture of intact and destabilized proteins (for details see ref 240). Figure 5.1 shows the results of simulated absorption (curves a'), fluorescence (curve b') and nonresonant HB (curve c') spectra using the Hamiltonian presented in Table 5.1 compared to the respective experimental data (curves a–c). The lowest energy absorption ($12\,110 \text{ cm}^{-1}$) and fluorescence ($12\,086 \text{ cm}^{-1}$) bands, in addition to the lowest energy hole, are well-fit by considering the entire FMO trimer, as shown previously for a simplified model consisting of only BChl *a* 3 and 4.^{131,201} In addition, only $E_\lambda \sim 15 \text{ cm}^{-1}$ can describe the small Stokes shift²⁴⁰ and fit the narrow absorption band at $12\,110 \text{ cm}^{-1}$ (due to weaker coupling to

phonon modes). For a qualitative comparison of simulated T-S, CD and LD spectra with experimental data from the literature, see Figures B.1 and B.2, as well as discussion, in Appendix B.

The “type 2” absorption spectrum of *C. tepidum* (where the $12\,430\text{ cm}^{-1}$ peak is more intense than the $12\,260\text{ cm}^{-1}$ peak^{35,208,251}) is reproduced and the intensity of the $12\,260\text{ cm}^{-1}$ peak is found to be critically dependent on the energy values of pigments strongly coupled to BChl *a* 4 (i.e., BChls 3, 5 and 7). Oscillator strength can be redistributed between BChl *a* 4 and BChl *a* 3, 5 and 7; suggesting that BChl *a* 4 plays an important role in the FMO absorption differences between species of GSB. Note that in this work the Q_y region is well-fit with 3 BChl *a* 8 per trimer. However, this assignment could be lower as mass spectrometry results indicate both detergent- and sodium carbonate-extracted FMO complexes have on average 2–3 BChl *a* 8 per complex.⁴⁰ An occupancy of ~80%, is a more likely scenario, but determining the exact spectroscopic contribution of BChl *a* 8 is beyond the scope of this work.

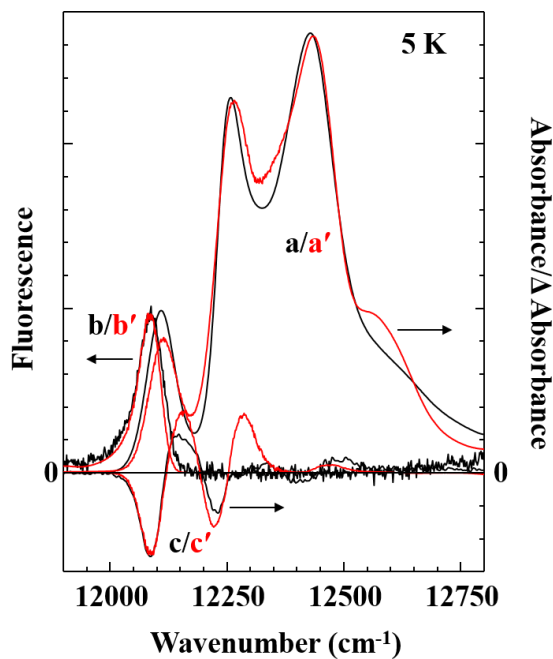


Figure 5.1 5 K experimental²⁴⁰ (black) and simulated (red) absorption (a/a'), emission (b/b') and nonresonant HB (c/c') spectra.

As reported recently,²⁵² simulated fits for absorption, fluorescence and nonresonant HB spectra may not lead to a unique parameter set. Specifically, different models of static and dynamic disorder were able to describe the experimental data of CP47 well. For the FMO simulations in this work, two additional parameters sets were used to describe the data in Figure 5.1: assuming all pigments have the same spectral density and S but variable inhomogeneous width; and all pigments have the same spectral density and inhomogeneous width but $S = 2.2$ for all BChl a except BChl a 3. However, the former and latter models failed to accurately describe exciton population dynamics and temperature-dependent absorption (see Figures B.3 and B.4 in Appendix B). In order to overcome the issues with the above-mentioned models, the fits shown in Figure 5.1 assume that the spectral density has a different shape for BChl a 3 (determined from Δ FLNS²⁰⁹) compared to all other BChl a . Since the coupling to phonons differs for BChl a 3, its inhomogeneous width is also allowed to vary from that of the other pigments. As shown below, this model is able to more accurately describe various experimental data.

The pigment spectral contributions are shown in Figure 5.2. In agreement with the current consensus,^{29,197,253} BChl a 3 is the most redshifted pigment and contributes ~85% to the lowest energy exciton state, while BChl a 4 contributes (~50%) mainly to the second exciton state at $\sim 12\,260\text{ cm}^{-1}$ (see Table 5.2). As BChl a 6 is located near the baseplate,¹⁹⁷ it has the highest site energy and is the main contributor to the highest energy exciton state; with minor contribution from BChl a 5. Note that a higher site energy of BChl a 5 is consistent with its position with respect to α helices 4 and 5.^{35,136} The positive ends of the α helix dipoles are in the vicinity of the positive region of the Q_y transition dipole (near N_D) of BChl a 5, potentially raising the pigment site energy.

Table 5.1 Frenkel exciton Hamiltonian for the FMO trimer in the site representation*

BChl <i>a</i>	1	2	3	4	5	6	7	8
1	12 405	-87	4.2	-5.2	5.5	-14	-6.1	21
2		12 505	28	6.9	1.5	8.7	4.5	4.2
3			12 150	-54	-0.2	-7.6	1.2	0.6
4				12 300	-62	-16	-51	-1.3
5					12 470	60	1.7	3.3
6						12 575	29	-7.9
7							12 375	-9.3
8								12 430

*All values in units of cm^{-1}

It is possible that the site energy of BChl *a* 5 differs in other species of GSB; that is, as mentioned previously, the intensity of the low-temperature absorption band at $12\,260\text{ cm}^{-1}$ was found to be sensitive to the site energy of pigments strongly coupled to BChl *a* 4. For example, as reported in Table 5.1 $|V_{45}| = 60\text{ cm}^{-1}$, which is the second largest off-diagonal element in the Hamiltonian. Thus, a different energy gap between BChl *a* 4 and 5 will have a significant impact on the shape of the absorption spectrum. In addition, while the local protein environment of most binding sites is highly conserved among species, there are differences near the binding site of BChl *a* 5 in *C. tepidum*^{35,38} which could result in a significant change in the site energy. Note that changes in the site energy of BChl *a* 7 could have similar effects, although the binding site is very homologous between various GSB species.^{35,38}

Table 5.2 Contribution numbers ($|c_{mM}|^2$) of sites m for states M from a simultaneous fit of spectra shown in Figure 5.1

$m \backslash M$	1	2	3	4	5	6	7	8
1	0.00	0.07	0.45	0.13	0.05	0.03	0.21	0.05
2	0.01	0.02	0.15	0.06	0.04	0.07	0.51	0.14
3	0.84	0.13	0.02	0.01	0.00	0.00	0.00	0.00
4	0.14	0.49	0.08	0.10	0.08	0.06	0.02	0.02
5	0.00	0.07	0.04	0.12	0.19	0.31	0.10	0.17
6	0.00	0.00	0.01	0.02	0.10	0.15	0.12	0.60
7	0.01	0.22	0.12	0.36	0.19	0.07	0.01	0.02
8	0.00	0.01	0.13	0.19	0.35	0.30	0.03	0.00
L_M	1.39	2.30	2.10	2.56	2.33	2.25	2.21	1.93

Due to its relatively recent discovery and seemingly partial occupancy, BChl *a* 8 has gained much interest into its occupancy in isolated versus in vivo FMO complexes and its role in EET. Since a small occupancy was predicted based on electron density of the X-ray structure³⁵ and the suggestions that BChl *a* 8 may be removed from the protein by detergent⁴⁰ or polyethylene glycol,³⁹ many studies neglect its presence by assuming only a negligible amount remains after protein purification. However, Wen et al.⁴⁰ showed that significant populations of BChl *a* 8 exist in various isolated FMO samples from *C. tepidum* in both detergent- and sodium carbonate-extracted samples. While theoretical studies often assign BChl *a* 8 a very blueshifted site energy (12 600–12 700 cm^{-1}),^{167,220} a spectral position of ~ 806 nm (12 407 cm^{-1}) was proposed based on absorption changes induced by chemical oxidation at 77 and 293 K.²⁰⁷ Below we report on the 5 K oxidation of FMO by potassium ferricyanide and compare to the spectral contribution of BChl *a* 8 from Redfield calculations.

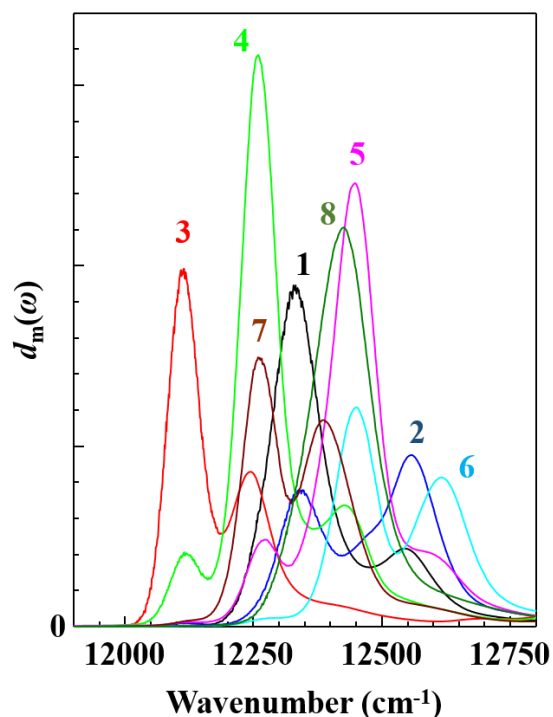


Figure 5.2 BChl *a* contributions to absorption ($d_m(\tilde{\nu})$) calculated with eq 5.2.

Figure 5.3 shows a comparison of two absorption spectra for FMO; chemically neutral (curve a) and oxidized (curve b). The oxidized sample had a concentration of ~ 2 M ferricyanide, which was much larger than used in the previous study.²⁰⁷ The difference curve (c) indicates that a small population of the low-energy BChl *a* 3 and 4 pigments are oxidized, but the main feature is the bleach at $12\,420\text{ cm}^{-1}$. Bina and Blankenship²⁰⁷ proposed that BChl *a* 8 should be preferentially oxidized due to its location at the interface of two protein subunits and, similar to Figure 5.3, observed the largest bleach $\sim 12\,400\text{ cm}^{-1}$. The green curve in Figure 5.3 is the spectral contribution from Figure 5.2 for BChl *a* 8 inverted and scaled for comparison. The distribution matches the bleach at $12\,420\text{ cm}^{-1}$ quite well and suggests that BChl *a* 8 contributes to the most intense $12\,430\text{ cm}^{-1}$ band in *C. tepidum*. The relative absorption changes in the $12\,420\text{ cm}^{-1}$ region indicate that curve b represents $\sim 30\%$ oxidation of the BChl *a* 8 population (assumed to be 3 per protein trimer). In this case, it is unlikely that BChl *a* 8 plays a role in the intensity of the

12 260 cm^{-1} absorption peak,³⁵ as a Q_y energy shift of -200 cm^{-1} for BChl *a* due to the coordination state of the central magnesium ion is unlikely.¹³⁷ Based on extensive model simulations, the difference between types 1 and 2 absorption spectra for FMO of various GSB results from differing interactions of BChl *a* 4 with nearby pigments (vide supra).

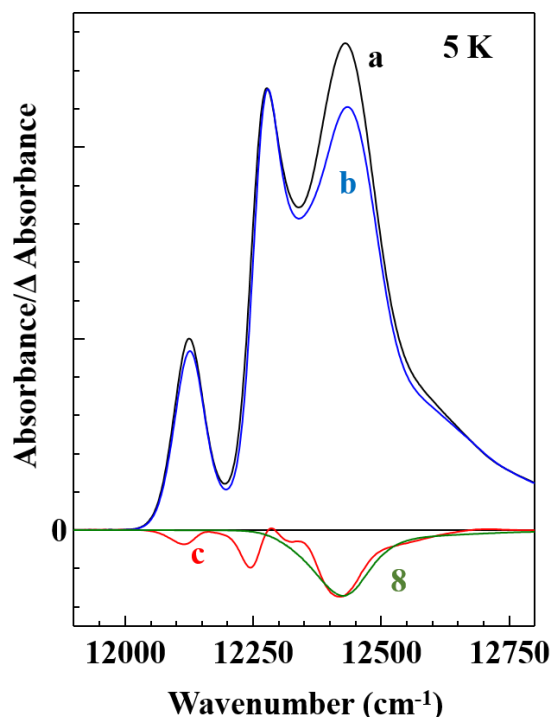


Figure 5.3 Absorption spectra for FMO in neutral (curve a) and oxidizing (curve b) conditions, i.e., after the addition of potassium ferricyanide. The red curve $c = b - a$. The green curve labeled 8 is the inverted and scaled BChl *a* 8 spectral contribution from Figure 5.2 with a peak position of $12\,422 \text{ cm}^{-1}$.

Calculated Redfield rate constants for intramonomer exciton relaxation are shown in Table 5.3. Redfield EET occurs between two states whose energy difference matches some phonon frequency of the bath.^{100,101} Thus, the rates depend on the spectral density used in calculations. Therefore, we emphasize that the spectral density shape must be experimentally established for the particular pigment–protein complex under study (e.g., in this work FMO). Only then can a reliable rate matrix be used to calculate exciton population dynamics (see Table 5.3). In ref 209 it was shown that the lognormal distribution for FMO (after multiplying by $\tilde{\nu}^2$) can be compared to

an Ohmic function with parameters from ref 116. The Ohmic parameters were determined by fitting 2D photon echo spectra (with $E_\lambda = 35 \text{ cm}^{-1}$), but should not be used in calculations as the Ohmic function cannot properly describe the PSB. However, the lognormal spectral density used in this work for high-energy pigments ($E_\lambda \sim 25 \text{ cm}^{-1}$) is capable of describing both the absorption lineshape and exciton population dynamics; although $E_\lambda \sim 15\text{--}20 \text{ cm}^{-1}$ is necessary to describe the lowest energy state.

Table 5.3 Rate constant matrix (ps⁻¹)

<i>M</i>	1	2	3	4	5	6	7	8
1	0	-1.7	-0.2	-0.1	-0.1	0	0	0
2	0	1.7	-0.7	-1.7	-0.8	-0.5	-0.2	-0.1
3	0	0	0.9	-0.6	-0.8	-0.5	-1.5	-0.2
4	0	0	0	2.4	-0.6	-0.7	-0.7	-0.4
5	0	0	0	0	2.3	-0.4	-0.7	-0.9
6	0	0	0	0	0	2.2	-0.8	-1.6
7	0	0	0	0	0	0	3.9	-0.7
8	0	0	0	0	0	0	0	4.0

Figure 5.4 shows the exciton population dynamics determined from Table 5.3. The initial populations are calculated assuming excitation by a 50 fs laser pulse at $12\,626 \text{ cm}^{-1}$.^{108,116} States 6, 7 and 8 have the largest initial populations, with the lowest energy state 1 having negligible initial population. By 5 ps the population of state 1 is approximately 70% via relaxation from state 2 ($k_{21} = 1.7 \text{ ps}^{-1}$). As reported previously,^{108,116} state 3 decays rather slowly due to the small spatial overlap with exciton states 1 and 2.¹¹⁶ The relative populations in Figure 5.4 are consistent with experimental data, which observed relaxation to the lowest energy state within 1–10 ps.^{244,254,255}

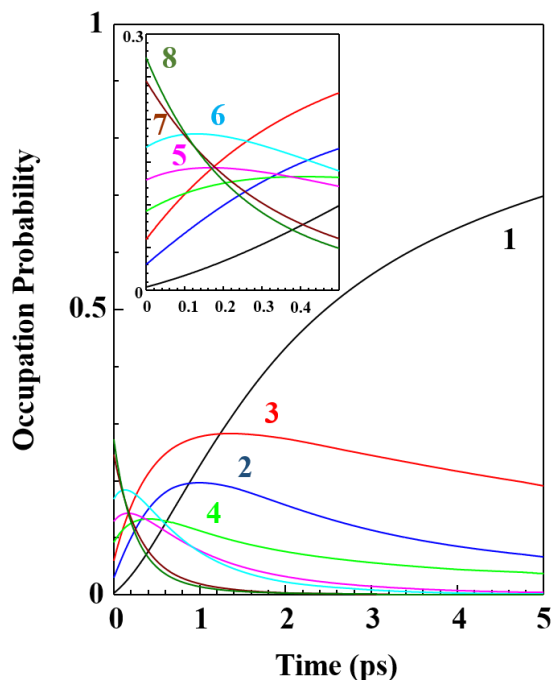


Figure 5.4 Exciton population dynamics after initial excitation by a 50 fs laser pulse ($12\,626\text{ cm}^{-1}$).^{108,116} The initial populations are normalized to one. The inset shows the dynamics of the fast-decaying, high-energy state in the first 0.5 ps.

The temperature dependence in Redfield calculations is solely due to the shape of the spectral density and strength of S .⁹⁹ As noted above and in Appendix B, a large value of S cannot explain temperature-dependent absorption spectra of FMO; consistent with previous studies.^{108,163,211} Temperature-dependent absorption spectra, calculated with the parameters of Table 5.1, are shown in Figure 5.5. The temperature range was chosen such that additional effects due to crossing the glass transition (150–200 K),^{256,257} can be ignored. A comparison of frames A and B shows that the parameters used in this work are capable of describing the temperature dependence, as the three main absorption bands are still resolved even at 150 K.

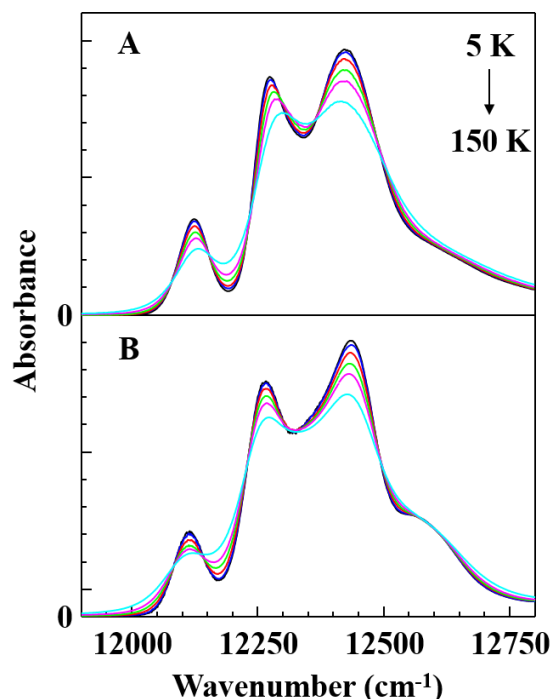


Figure 5.5 Frame A: Experimental temperature-dependent absorption spectra measured at 5, 25, 50, 75, 100 and 150 K. Frame B: Corresponding simulated curves.

In regards to the photosystem of GSB, Figure 5.6 shows the energy levels of FMO calculated in this work compared to the 5 K fluorescence spectrum of the chlorosome–baseplate complex of *C. tepidum*.²⁶ The FMO absorption covers the region from 12 100 to 12 600 cm^{-1} and exhibits spectral overlap with both the chlorosome and baseplate (BChl *a*–CsmA) fluorescence bands. The baseplate, which is spatially close to BChl *a* 1 and 6,¹⁹⁷ has an emission band coinciding with the spectral position of the lowest energy states of FMO. However, at room temperature this fluorescence band broadens significantly and shifts to $\sim 12\,430\ \text{cm}^{-1}$,^{136,220} which increases spectral overlap with the higher energy exciton levels. This increased spectral overlap can promote more efficient EET, as incoherent hopping is distance dependent and BChl *a* 6 and 8 have been proposed as excitation entrances to FMO due to their close proximity with the baseplate.^{108,220,223} Such an arrangement is consistent with the “downhill energy funnel” model of FMO.¹³⁶ Although the exact structure of the chlorosome–baseplate–FMO–RC (including BChl *a* distances and orientations) is

not known, recent studies have reported that within 10 ps 60–70% of the exciton transfers from the chlorosome to FMO via the baseplate,²⁵⁸ while FMO → RC EET is on the order of hundreds of ps.²⁵⁹

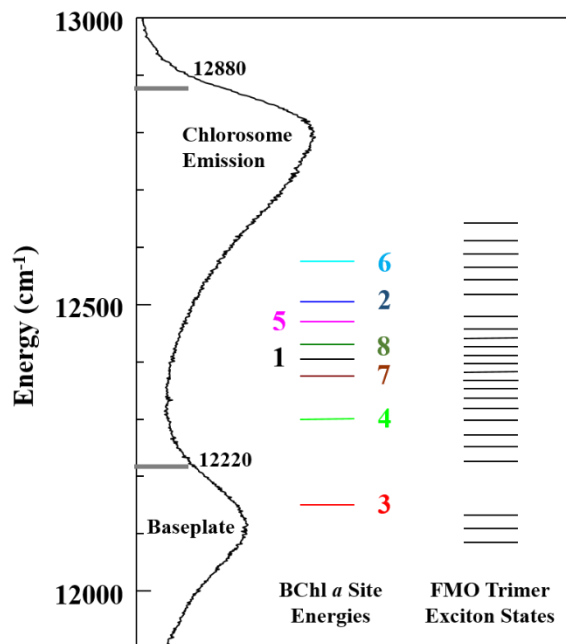


Figure 5.6 Energy levels of the eight BChl *a* site energies and 24 exciton states. The spectrum is the experimental fluorescence for the chlorosome–baseplate system,²⁶ with horizontal grey bars indicating the maxima of the ZPH action spectra for the chlorosome²⁶⁰ and baseplate²⁶ pigments.

5.4 Conclusions

The present study (see also Appendix B) has shown that the whole trimer, and presence of uncorrelated EET between monomers of the trimer, must be considered to explain various linear optical spectra. The pigment site energies elucidated from simultaneous fits of 5 K absorption, fluorescence and persistent nonresonant HB spectra are also consistent with previously reported exciton population dynamics revealed by time-domain spectra.^{244,254,255} BChl *a* 8 contributes to the absorption spectrum at $\sim 12\,420\text{ cm}^{-1}$. This assignment contrasts the high energy values previously proposed by theoretical considerations,^{167,220} but is consistent with experimental data for oxidized FMO reported in this work and ref 207. More detailed experimental studies (including studies of

different FMO mutants) are needed to provide additional evidence about the spectral contribution of BChl *a* 8 to optical spectra.

A more accurate description of the site-dependent el-ph coupling is of interest, as dynamics and extracted site energies critically depend on the shape of the spectral density. In this work, a minimum of two spectral density shapes were necessary in order to describe the exciton population dynamics and temperature-dependent broadening. Even though molecular dynamics simulations can provide information on spectral densities,^{166,261,262} the analytical form needed to extract spectral density shapes from energy gap fluctuations cannot describe the PSB nor define the *S* factor.²⁰⁹ To date only the spectral density shape of the lowest energy state can be measured experimentally. Thus, more work is needed to extract site-dependent spectral densities from experimental data. In order to further test the Hamiltonian and el-ph coupling parameters proposed in this work, theoretical descriptions of pump-probe and 2DES frequency maps are also needed to provide more insight on the population and coherence dynamics for the FMO complex, in particular on the time evolution of the 2DES rephasing and non-rephasing spectra of the FMO trimer when treated separately (research in progress).

Acknowledgments

This work was supported by the U.S. Department of Energy, Office of Science, Office of Basic Energy Sciences, under Award Number DE-SC-0006678 (to R.J.). Sample preparation of the FMO protein was funded by the Photosynthetic Antenna Research Center (PARC), an Energy Frontier Research Center funded by the U.S. Department of Energy, Office of Science, Office of Basic Energy Sciences, under Award Number DE-SC-0001035. The authors acknowledge useful discussion with Dr. Darius Abramavicius (Vilnius University, Lithuania) and Dr. Tonu Reinot for help in development of the software used in the present work.

Chapter 6

New Insight into the Water-Soluble Chlorophyll-Binding

Protein from *Lepidium virginicum*

Adam Kell,[†] Dominika Bednarczyk,[§] Khem Acharya,[†]

Jinhai Chen,[†] Dror Noy,^{||} and Ryszard Jankowiak^{†,‡}

[†]Department of Chemistry and [‡]Department of Physics, Kansas State University, Manhattan, Kansas 66506, USA

[§]Department of Biological Chemistry, Weizmann Institute of Sciences, Rehovot 76100, Israel

^{||}Migal – Galilee Research Institute, Kiryat Shmona 11016, Israel

Reproduced from *Photochemistry Photobiology* **2016** (DOI: 10.1111/php.12581)

Copyright 2016 Wiley

Abstract

This study describes new recombinant LvWSCP. This complex binds four Chls (i.e., two dimers of Chls) per protein tetramer. We show that absorption, emission, HB spectra and the shape of the ZPH action spectrum are consistent with the presence of uncorrelated EET between two Chl dimers. Thus, there is no need to include slow protein relaxation within the lowest excited state (as suggested in a previous analysis of CaWSCP^{263,264}) in order to explain the large shift observed between the maxima of the ZPH action and emission spectra. Experimental evidence is provided which shows that electron exchange between lowest energy Chls and the protein may occur, i.e., electrons can be trapped at low temperature by nearby aromatic amino acids. The latter explains the shape of nonresonant HB spectra (i.e., the absence of antihole), demonstrating that the HB process in LvWSCP is largely photochemical in nature, though a small contribution from NPHB (in resonant holes) is also observed.

6.1. Introduction

In this work, we focus on the recombinant LvWSCP that was reconstituted with Chl *a* using a water-in-oil emulsion system.⁷⁰ These proteins have the sequence of mature, native LvWSCP without a C-terminal extension, which was cleaved off post-translationally *in vivo*.⁶³ This is in contrast to previously studied recombinant CaWSCP, which included, in addition to the C-terminal extension, an N-terminal six-histidine-tag.⁶⁸ WSCPs bind Chls with very high affinity and it has been demonstrated that WSCP can extract Chls from the thylakoid membrane.^{50,55,57} Typically, four Chl molecules are bound within the central hydrophobic protein cavity that is well shielded from the aqueous polar environment.⁴⁷ However, the functional importance of WSCP has not been clarified.

WSCPs are divided into two classes, I or II, depending on whether or not the absorption spectrum experiences a redshift after illumination of visible light, respectively.⁴⁶ Further, class II proteins can be categorized as class IIa or IIb based upon the binding ratio of Chl *a/b* in native complexes.^{62,63} Class IIa has a higher Chl *a/b* ratio than total leaf extract, while class IIb has a Chl *a/b* ratio lower than total leaf extract. LvWSCP (class IIb) is found in Virginia pepperweed^{54,265} and oligomerized preferentially to a tetramer,^{47,48} similar to CaWSCP (class IIa).^{57,68} However, it has been argued in several papers that class IIa protein tetramers bind a smaller number of Chls, e.g., two and one for CaWSCP^{57,68,69} and WSCP from Brussels sprouts,⁵⁰ respectively. Yet, recent spectroscopic evidence suggest that all class II WSCPs bind four Chls per tetramer.⁷⁰ Class IIb proteins were shown to bind four Chls per tetramer,⁵⁵ and this was verified by the X-ray crystal structure of LvWSCP (PDB ID: 2DRE)⁴⁷ that revealed four Chls bound within the core of a homotetrameric protein complex. The crystal structure of the LvWSCP protein complex is shown in Figure 6.1A, with the arrangement of the four Chl *a* pigments shown in frame B. Based on the X-

ray structure, the Chls are arranged in two “open sandwich” dimers related by nearly exact two-fold symmetry, while the Chls of each dimer have a tilt angle of 27° and a center-to-center distance of 10 \AA .⁴⁷

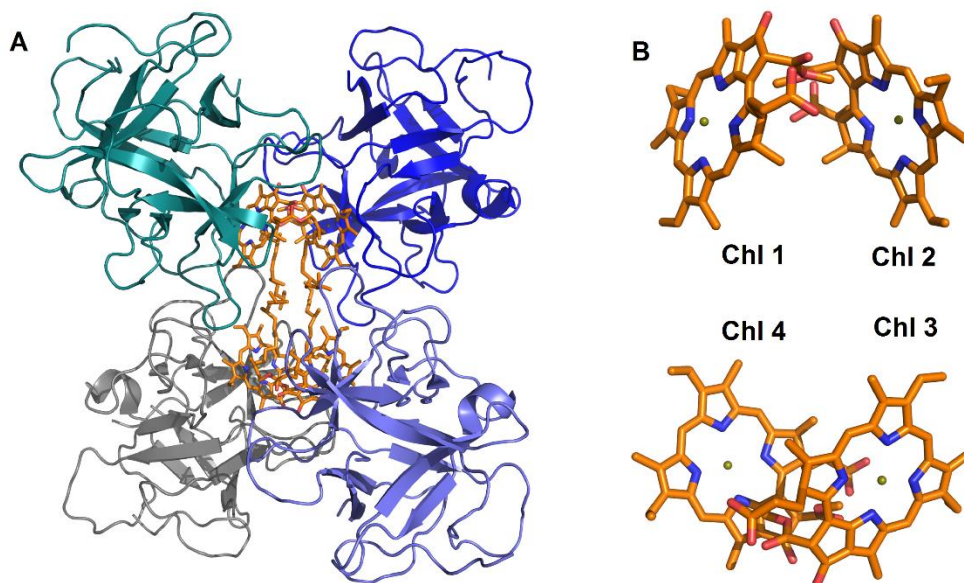


Figure 6.1 Frame A: Overall structure of the tetrameric LvWSCP. The four monomers are shown in green, blue, purple and grey. The four Chls are shown in orange. Frame B: The geometry of the 1/2 and 3/4 Chl dimers, with the phytol tails truncated for clarity. Both frames are based on the 2 \AA resolution crystal structure.⁴⁷

WSCPs are of great interest for high-resolution spectroscopic and modeling studies, and are being extensively studied, as they contain a small number of pigments that are tightly packed in a hydrophobic cavity at the center of the complex.⁴⁷ Yet, although LvWSCP is structurally well characterized by X-ray crystallography, most if not all of the spectroscopic work has been carried out on CaWSCP. For example, persistent spectral HB at 4.5 K has been used to investigate the excitonic energy level structure and the excited state dynamics of recombinant CaWSCP.²⁶⁴ The HB technique relies on differences observed in the absorption spectrum of a low-temperature system after narrow-band laser excitation. If a pigment molecule (in resonance with the laser) undergoes a photochemical reaction, it ceases to absorb at its original wavelength/frequency and

one speaks of PHB. In the case of NPHB, the pigment molecule does not undergo a chemical reaction, but its immediate environment experiences some rearrangement (for details see refs 96 and 124). Both PHB and NPHB result in the formation of persistent holes, meaning the holes are preserved after the initial excitation is turned off, as long as low temperature is maintained. In either case, the HB spectrum is obtained as the difference between the measured absorption spectrum before and after laser excitation. The reported HB spectra^{165,264} were composed of four main features: (1) a narrow ZPH at λ_B ; (2) a number of vibrational ZPHs; (3) a broad low-energy hole at ~ 683 and ~ 665 nm for Chl *a*- and Chl *b*-WSCP, respectively; and (4) a second satellite hole at ~ 673 and ~ 658 nm for Chl *a*- and Chl *b*-WSCP, respectively. A strongly asymmetric and highly structured PSB with the peak phonon frequency at $24/23$ cm^{-1} and shoulders at $48/46$ cm^{-1} and $88/82$ cm^{-1} has also been observed for Chl *a*/Chl *b*-WSCP.¹⁶⁵ Δ FLN and HB spectroscopies provided quantitative insight into el-ph coupling of excitonically coupled Chl homodimers in recombinant CaWSCP, revealing a moderately weak *S* of 0.81–0.85 and a rich structure of $S_1 \rightarrow S_0$ vibrational frequencies.^{165,264} Optical spectra have also been provided for Chl *d*-WSCP,¹⁰⁷ and 2DES has been used to probe energy transfer dynamics in LvWSCP.²⁶⁶

Previous spectroscopic and modeling studies provided evidence for significant exciton interaction between equivalent Chls in CaWSCP.^{107,165,189,264} The crystal structure of LvWSCP was used to model linear absorption and CD spectra, as well as excited state decay times, of CaWSCP reconstituted with Chl *a* and Chl *b*; assuming that the same binding motif exists in both class IIa and class IIb proteins.^{175,189} The close agreement between theory and experiment indeed suggested that this is the case, i.e., both types of WSCP share a common Chl binding motif, where the opening angle between pigment planes in class IIa should not differ by more than 10° from that of class IIb¹⁸⁹ (observed to be 27° based on X-ray crystallography data⁴⁷). A modeling study

based on fits of linear spectra,¹⁸⁹ taking into account lifetime broadening, vibrational sidebands and static disorder, revealed a tilt angle of 25°–36° between the chlorin ring planes, which was about half of the value suggested previously.¹⁰⁷ However, in the latter work the tilt angle was estimated based on simple exciton theory.

Below we report experimental room-temperature absorption, emission and CD spectra, as well as low-temperature absorption, emission and persistent HB spectra obtained for LvWSCP. The key aim of this work is to explain the nature of various linear optical spectra, including the shapes of *nonresonant* HB spectra. We argue that HB spectra provide additional insight into excitonic structure and EET of LvWSCP, i.e., on ultrafast relaxation processes between the strongly coupled states within the 1/2 and 3/4 dimers, as well as a possible interdimer energy transfer. The key questions addressed in this work are: (1) Is interdimer energy transfer in LvWSCP reflected in HB spectra and the shape of the ZPH action spectrum?; (2) Do the protein (280 nm) and Chl Q_y region (660–670 nm) absorption bands of LvWSCP and CaWSCP reveal a similar ratio of Chl to protein subunit?; and (3) Is it necessary to assume a slow protein relaxation between energetically inequivalent conformational sub-states within the lowest exciton state to explain optical spectra obtained for LvWSCP?

6.2. Materials and Methods

Recombinant Chl *a*-LvWSCP were prepared using water-in-oil emulsions, as described previously.⁷⁰ See Appendix C for the gene sequence of LvWSCP. Details about the measurement setup were described elsewhere.¹⁹⁹ Here, only a brief description is given. A Bruker HR125 Fourier transform spectrometer was used to measure the absorption and HB spectra in the Vis/NIR region. In absorption and nonresonant HB, the resolution was set at 4 cm⁻¹. For resonant HB, spectral resolutions of 0.5 or 1 cm⁻¹ were used. UV spectra were collected by a McPherson 2061

monochromator with a Princeton Instruments 1024 ICCD camera with a resolution of 2 nm. The fluorescence spectra were collected by a Princeton Instruments Acton SP-2300 spectrograph equipped with a back-illuminated CCD camera (PI Acton Spec-10, 1340 × 400). All emission spectra were obtained with a resolution of 0.1 nm. The laser source for both nonresonant HB and fluorescence was 496.5 nm, produced from a Coherent Innova 200 argon ion laser. In the resonant HB experiments, the tunable wavelengths came from a Coherent CR699 ring dye laser pumped by a Millennia 10s diode-pumped, solid-state laser at 532 nm from Spectra-Physics. With laser dye LD 688 (Exciton), a spectral range of 650 to 720 nm was available with a linewidth of 0.07 cm⁻¹. Power from the ring laser output was stabilized with a Laser Power Controller (Brockton Electro-Optics Corp.), while laser power in the experiments was precisely set by a continuously adjustable neutral density filter. The OD of the sample for the nonresonant and resonant HB was 0.6, while for emission spectra, OD ~ 0.1. All experiments were performed at 4.5 K inside an Oxford Instruments Optistat CF2 or a Janis 8-DT Super Vari-Temp cryostat for Vis/NIR spectra, and a Janis Supertran-VP cryostat for UV spectra. Sample temperature was read and controlled with a Mercury iTC or Lakeshore Cryotronic model 330 temperature controller for the Oxford and Janis cryostats, respectively. Chl *a*-LvWSCP spectra were recorded at room temperature with the instrumentation described above, as well as with a Jasco V-7200 Spectrophotometer with UV-Vis light in a range from 250 to 800 nm, using a quartz cuvette with a path length of 10 mm. The CD spectra were measured at room temperature with a Jasco J-815 CD Spectrometer in a range from 250 to 750 nm using a quartz cuvette with a path length of 10 mm, scan speed of 100 nm min⁻¹, bandwidth of 4 nm, data pitch of 0.5 nm and response time of 2 s. Data from five consecutive measurements of each sample were averaged.

6.3. Results

6.3.1. Room- and Low-Temperature Optical Spectra

Figure 6.2 shows the room-temperature UV-Vis absorption spectra of LvWSCP and CaWSCP. Although in this work we focus on LvWSCP, the comparison in Figure 6.2 reveals nearly identical ratios of protein absorbance at 280 nm to Chl Q_y region absorbance (observed for all samples studied). Since it is well established that LvWSCP binds four Chls per protein tetramer,^{47,55,70} the previous implies that both LvWSCP and CaWSCP bind the same number of Chls per protein tetramer,⁷⁰ in contrast to previous reports on CaWSCP binding only two Chls per tetramer.^{57,68,69,189,263} The discrepancy is most likely because previous studies used Chl extraction in order to determine the protein/Chl ratio, which may be biased by the very high Chl binding affinity of WSCPs. The latter could prevent complete extraction of Chls from the protein samples.

However, the asterisk in the inset of Figure 6.2 shows that the absorption bands are not identical. Thus, it is possible that a small subpopulation of Chl could be converted to Chl derivatives, as observed previously in the low-energy Q_y region for Chl *b*-CaWSCP.^{165,264} In addition, the room-temperature CaWSCP absorption spectrum in ref 70 shows a more intense shoulder at 660 nm and absorption band at 420 nm than spectrum b. The large blueshift of the LvWSCP Q_y region absorption bands in comparison with CaWSCP is very intriguing and will be revealed by ongoing mutational studies; however, here we only mention that the above shift could be induced by differences in the amino acid sequences of the two proteins.

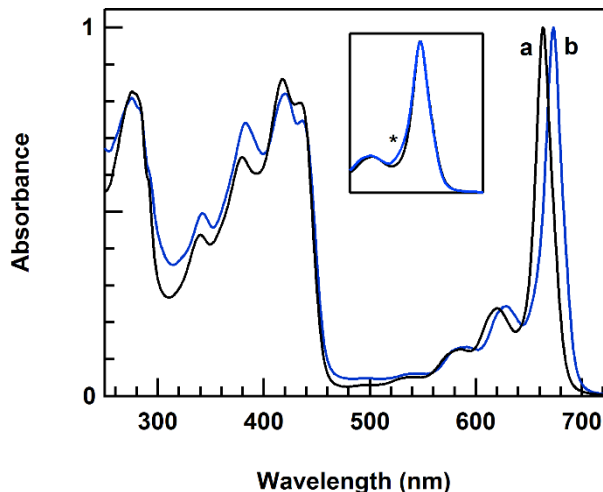


Figure 6.2 Spectra a and b correspond to the room-temperature absorption spectra obtained for LvWSCP and CaWSCP, respectively, using a novel water-in-oil emulsion system. The inset shows that the Chl Q_y region absorption spectra of both proteins (when arbitrarily shifted for a direct comparison) are nearly indistinguishable. A small difference on the high-energy side (see asterisk) may indicate potential contribution at ~ 660 nm from Chl derivatives in CaWSCP.

Figure 6.3 (frame A) shows room-temperature absorption (curve a, with a maximum of ~ 663 nm), emission (curve b, with the (0,0)-band near 675 nm) and CD (curve c, with the positive band at ~ 672 nm and a crossing point at ~ 665 nm) spectra obtained for LvWSCP. The CD spectrum is conservative, i.e., it does not contain any intrinsic negative CD of Chl *a* which is in agreement with the CD spectra obtained for CaWSCP.^{107,175} Frame B shows typical 4.5 K absorption and fluorescence spectra measured for low-OD samples to avoid reabsorption (OD = 0.1 at the ~ 663 nm band maximum). Compared with the literature spectra for CaWSCP,^{107,165,264} all low-temperature spectra of LvWSCP are blueshifted by ~ 11 nm (250 cm^{-1}). That is, in CaWSCP spectra (data not shown), the main absorption Q_y (0,0)-band (4.5 K) is located at 672.5 nm, while a weaker shoulder is redshifted to about 681 nm.^{107,165,264}

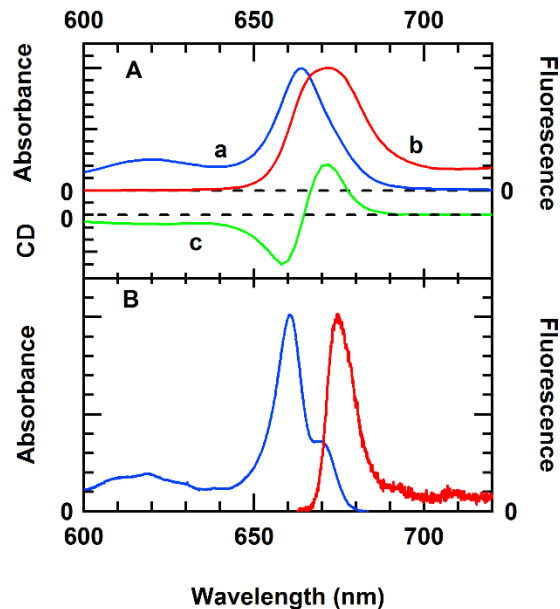


Figure 6.3 Frame A: LvWSCP room-temperature absorption (curve a, maximum of ~663 nm), emission (curve b, (0,0)-band near 675 nm) and CD (curve c) spectra. Frame B: 4.5 K absorption and fluorescence spectra (OD = 0.1).

6.3.2. Nonresonant and Resonant Hole-Burned Spectra

To characterize the inhomogeneity and excitonic structure of LvWSCP, persistent HB was performed at multiple λ_B ranging from 678 to 667 nm across the low-energy absorption band of LvWSCP. Figure 6.4 shows the 4.5 K absorption (curve a) and fluence-dependent, nonresonant HB spectra (curves c–i); where fluence is given by $f = It_B$, with I and t_B corresponding to laser intensity and burn time, respectively. The Gaussian fit (curve b) illustrates the shape of the SDF; being the spectral envelope of the inverted ZPH action spectrum (sharp spikes). ZPHs are obtained using constant fluence (6 J cm^{-2}) with burn depth $< 10\%$ and a read resolution of 0.5 cm^{-1} . The hole widths are resolution limited, although for $\lambda_B < 671 \text{ nm}$ the holes are slightly affected by lifetime broadening. Curves c through i are the nonresonant persistent HB spectra obtained with $\lambda_B = 496.5 \text{ nm}$. Interestingly, there is a lack of antihole (or photoproduct) in the measured spectral range of 500–1000 nm characteristic of a PHB process (vide infra).

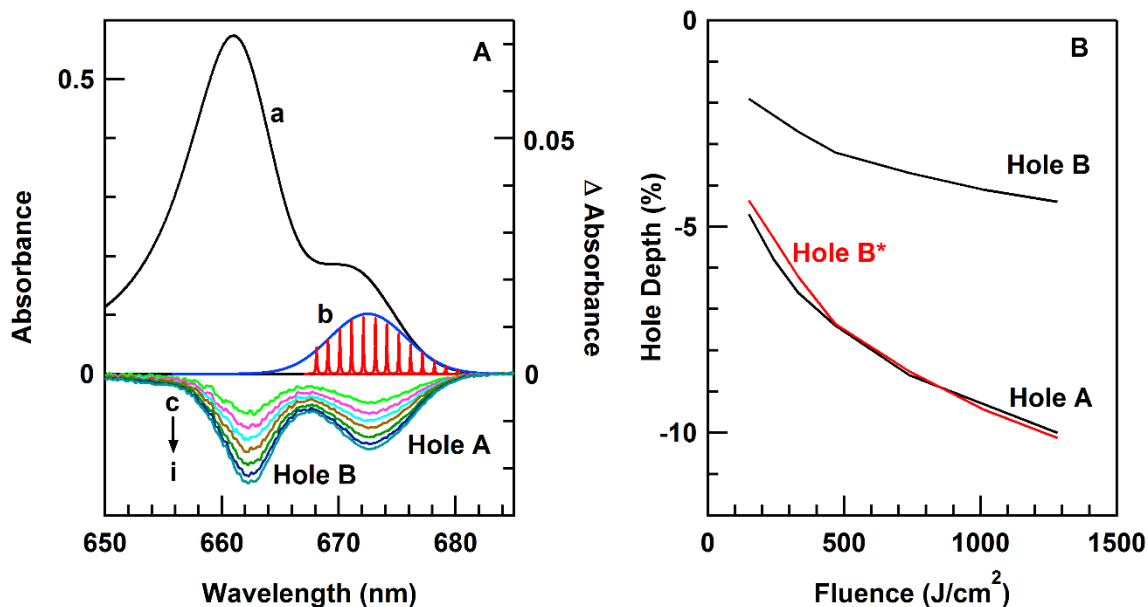


Figure 6.4 Frame A: Absorption (curve a), Lorentzian fits to the inverted ZPHs (red, narrow spikes), Gaussian ZPH action spectrum (curve b), and nonresonant HB spectra (curves c–i, $\lambda_B = 496.5$ nm). Holes A and B have minima at 672.7 and 662.3 nm, respectively. Frame B: Percent hole depth versus fluence plot for holes A and B of frame A. The red curve (Hole B*) is the black Hole B curve multiplied by a factor of 2.3, showing that holes A and B burn in concert.

Figure 6.5 shows resonant HB spectra for different λ_B (see arrows) in the Q_y region. All spectra, in addition to the sharp ZPHs and accompanying PSBHs, exhibit broad holes identical to those induced by nonresonant excitation (see Figure 6.4A). The presence of sharp and broad features induced by resonant excitation was also observed for CaWSCP.²⁶⁴ Fluence-dependent holes for $\lambda_B = 677$ nm are shown in Figure 6.5B normalized to the bleach at 662.3 nm. The intensities of the ZPHs are shown by the horizontal arrows and percent hole depth is given. It is clear that the resonant holes at 677 nm and broad features (at 672.7 and 662.3 nm) do not burn in concert and are due to two independent processes. While it is clear that the ZPHs are due to resonant laser excitation, it is not as obvious if the nonresonant holes are induced by the same or another excitation source (e.g., white light from the spectrometer). To check if HB can occur by white light excitation, multiple absorption spectra were recorded sequentially in the absence of

laser excitation. However, no HB was observed, suggesting that the spectrometer white light does not cause formation of nonresonant holes. A detailed theoretical study is necessary to investigate whether excitonic interactions could account for the observed bleach after laser excitation and potential photo-oxidation of Chls; thus, in this work, we ascribe NPHB and PHB to the resonant and nonresonant features, respectively (vide infra).

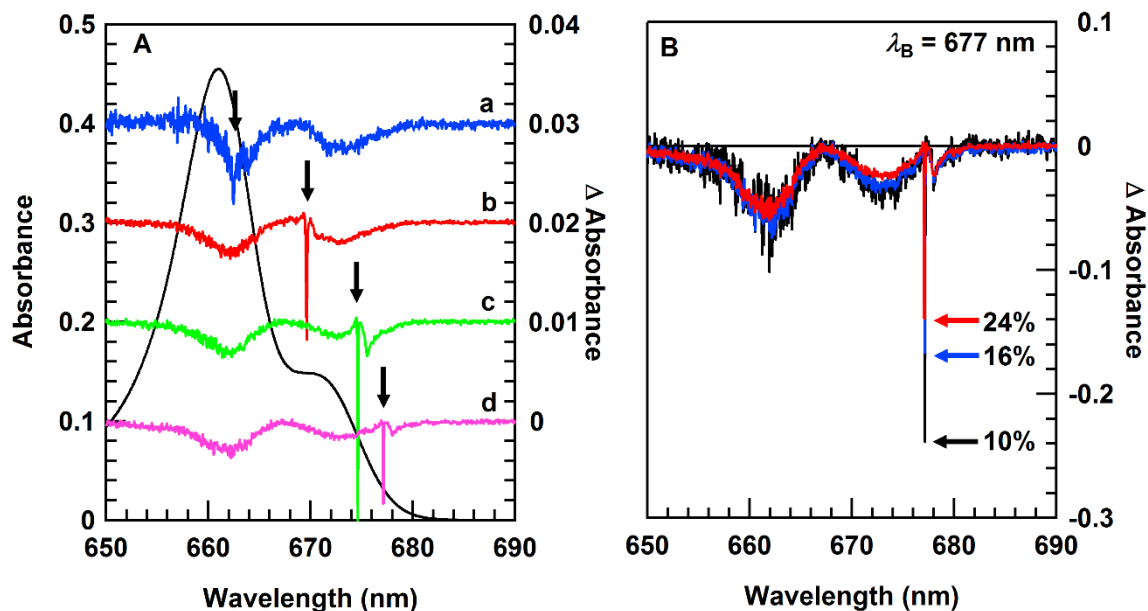


Figure 6.5 Frame A: Resonant HB spectra burned at 662.5, 669.5, 674.5 and 677 nm for holes a–d, respectively, with fluence $\sim 30 \text{ J cm}^{-2}$. Vertical arrows mark λ_B and the ZPHs. Frame B: Fluence-dependent HB spectra ($\lambda_B = 677 \text{ nm}$) normalized to the $\sim 660 \text{ nm}$ hole. Horizontal arrows mark the ZPH depths and percent hole depth is given.

6.3.3. On the Nature of Nonresonant Holes

For nonresonant HB spectroscopy, high-energy Chl states are excited which have negligible HB yield due to very fast relaxation to the Q_y state.⁹⁶ Additionally, the presence of EET between Chls competes with the HB process (i.e., decreases the HB yield) and (for EET on the order of ps) only the lowest energy state experiences HB.⁹⁶ The persistent HB spectrum is the resulting absorption difference before and after laser excitation. The shape of the persistent holes in Figure 6.4 clearly suggests that the origin of these holes (to a large extent) must be

photochemical in nature. We hasten to add that temperature annealing experiments did not reveal any permanent photodamage. That is, the bleaching is 100% reversible, and upon annealing all holes were perfectly removed and the original absorption spectrum was recovered. Such efficient photochemistry (revealed via persistent holes), to the best of our knowledge, has never been observed in any photosynthetic complexes studied so far, although, partly nonconserved (nonresonant) holes were also observed for the FMO complex.²⁴⁰ A similar effect, though not as strong as in the case of LvWSCP discussed in this work, was observed for CaWSCP, Chlide *a*-WSCPs, and in part, in FMO complexes for high fluences (unpublished data). This suggests that electron exchange between photosynthetic pigments and the protein, to different degrees, could be present in some photosynthetic complexes.

To shed more light on this phenomenon in LvWSCP, HB spectra with $\lambda_B = 496.5$ nm ($I = 440$ mW) were measured while monitoring bleaching in the UV spectral region. Figure 6.6 shows the UV absorption spectra of LvWSCP (curve a) in buffer/glycerol-based glass at 5 K. Curves b and c correspond to the 5 K nonresonant HB spectra obtained with fluences of 9 and 2175 J cm⁻², respectively. Curve b was multiplied by a factor of 3.5 to match the high-energy part of the bleach. The difference spectrum (c – b) reveals an additional bleach at higher fluences and is assigned to bleach of oxidized tryptophan (Trp) molecules located in the vicinity of the Chls (see Figure 6.6B). The weak band indicated by an asterisk, in agreement with theoretical calculations,²⁶⁷ does not correspond to protein, but Chl. Thus, the resulting holes near 245 and 280 nm can most likely be attributed to bleach of Chl and Trp, respectively, upon formation of redox products. Therefore, we suggest that electron exchange can occur between Chls and nearby Trp residues (Trp90 and Trp154).

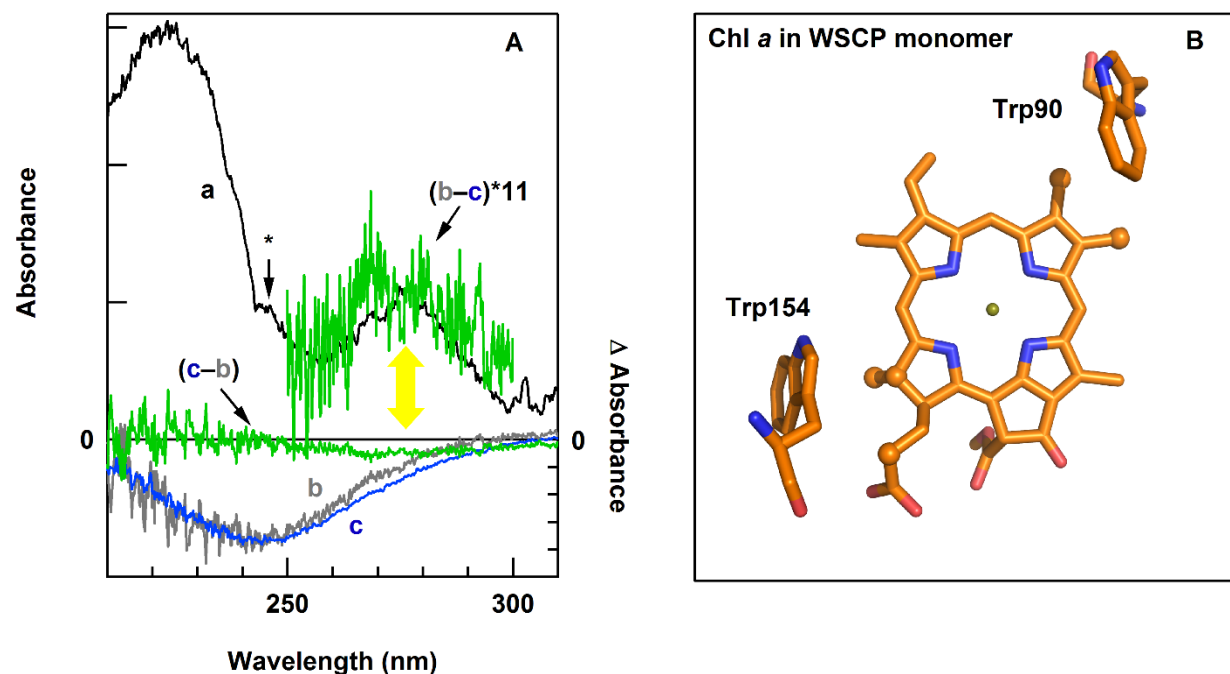


Figure 6.6 Frame A: Spectrum a is the low-temperature (5 K) UV absorption spectrum of LvWSCP. Curves b and c are the persistent HB spectra obtained with $\lambda_B = 496.5$ nm for fluences of 9 and 2175 J cm^{-2} , respectively. Curve b was multiplied by a factor of 3.5 for easy comparison. The green curve (c – b) is the difference spectra between high- and low-fluence HB spectra, which has been inverted and expanded for comparison to the protein absorption at 275 nm. The asterisk marks putative Chl UV absorption. Frame B: interactions between Chl *a* and Trp residues in LvWSCP. Chl *a* and Trp residues are shown in stick representations. Spheres mark Chl *a* atoms that are within 4 Å of a Trp residue. For clarity, the phytyl chains atoms of Chl *a* are not shown.

6.4. Discussion

6.4.1. Interdimer Uncorrelated Excitation Energy Transfer

Theiss et al.⁶⁹ argued that the arrangement of two Chls within the CaWSCP tetramer is the dominant structure, i.e., the existence of complexes containing one, three, or four Chls per tetramer is of low probability. In this regard, Pieper et al.^{165,264} assumed that CaWSCP binds only two Chl molecules per protein tetramer, so that a larger number of excited states can be ruled out. Theiss and colleagues⁶⁹ also argued that the 400 fs component they observed in time-resolved flash-induced transient absorption for CaWSCP corresponds to excited-state relaxation from the upper to the lower excitonic level of the strongly coupled “open sandwich” dimer. It is reasonable to

conclude from ref 70 and data presented in this work, which relied on the X-ray structural assignment for LvWSCP⁴⁷ and direct spectroscopic measurement rather than Chl extraction assays, that both LvWSCP and CaWSCP bind four Chls per complex.

Note that ref 263 found negligible emission near 667 nm for Chl *b* in CaWSCP samples with 4.2 and 2.6 Chl *a*:Chl *b*, even though the probability of Chl *b* homodimers is 3.5% and 8%, respectively. A tentative conclusion was drawn that WSCPs preferentially form heterodimers. Based on Figure 6.2 and data presented in ref 70, which show that class II WSCPs can bind more than two Chls per complex, the lack of fluorescence at 667 nm is not surprising. That is, the probability of forming Chl *b* homotetramers is 0.13% and 0.61% for samples containing 4.2 and 2.6 Chl *a*:Chl *b*, respectively. It is likely that previously studied CaWSCP samples bound four Chls per protein tetramer and the interpretation of optical spectra given below is not limited to LvWSCP.

For time-domain measurements, only 2DES data reported for LvWSCP have been interpreted as pertaining to a Chl tetramer.²⁶⁶ In addition to an unresolved lifetime longer than 1 ps, global analysis of wild-type LvWSCP (Chl *a*/Chl *b* ~2.4:1) revealed lifetimes of 50 and 250 fs, which were assigned to exciton relaxation and interdimer EET, respectively.²⁶⁶ The ZPH action spectrum in this work suggests a much slower EET time, as the resonant holes burned across the lowest energy band (668–680 nm) are resolution limited and ZPH depths trace out the entire SDF (as opposed to just the trap-state component, see below), indicating that the HB process strongly competes with EET. Below we discuss interdimer EET in Chl *a*-LvWSCP, focusing on the Chl tetramer and the emission peak position.

Since coupling matrix elements between the two dimers are very small compared to E_λ ($\sim 20 \text{ cm}^{-1} < \sim 60 \text{ cm}^{-1}$),²⁰⁹ we first consider two Chl dimers possessing identical SDFs that are connected by slow EET (for more details on uncorrelated EET see refs 131, 140 and 268). In this

model, in a given tetramer, one or another dimer can be lower in energy (due to disorder) and their energies are independent. Figure 6.7A presents a proposed composition of the SDF shown in Figure 6.4 (curve b), i.e., curve b in Figure 6.7A represents the identical SDFs of the low-energy Chl of each dimer. Grey curves c and d represent the sub-SDFs corresponding to Chls that can transfer and trap energy, respectively. That is, curve d represents the calculated probability of finding a pigment at a given energy that is also capable of EET and, correspondingly, curve c represents the probability that a pigment at a given energy is incapable of EET. Therefore, emission will originate from Chls with the sub-SDF represented by curve c when EET is present, and the entire SDF (curve b) when EET is absent. Curves d and c are equivalent to curve b (on an energy scale) multiplied by its cumulative distribution function and one minus the cumulative distribution function, respectively.^{131,140,268}

The calculated emission spectra, curves b' and c', are found by convoluting the single-site fluorescence spectrum¹⁶⁵ with curves b and c from frame A, respectively. These data clearly show that EET is capable of explaining the redshifted emission spectrum. That is, emission only occurs for the low-energy sub-SDF (curve c) which is incapable of EET. If emission originates from the entire SDF (curve b), then the resulting fluorescence would be too broad and blueshifted (see calculated curve b') when compared to experiment (curve a'). Thus, uncorrelated EET between two strongly coupled dimers of the Chl tetramer is a plausible alternative to the model of protein relaxation suggested for CaWSCP.^{165,263,264} That is, we did not find that the lowest energy hole of our nonresonant HB spectrum, corresponding to the lowest exciton level in LvWSCP, was at lower energy than the SDF, as previously observed for CaWSCP.²⁶⁴ As seen in Figure 6.4, the Gaussian fit of the SDF (curve b) found at 672.5 nm (FWHM $\sim 165 \text{ cm}^{-1}$) is very similar to the shape of the lowest energy hole. However, the (0,0)-fluorescence band (OD ~ 0.1 to prevent reabsorption) is

still redshifted in comparison to the SDF position. The ZPH action spectrum is only slightly broader than that measured for CaWSCP (FWHM = 150 cm⁻¹),²⁶⁴ suggesting that both LvWSCP and CaWSCP have similar energy distributions. In light of this data and the fact that CaWSCP binds four Chls,⁷⁰ a model of uncorrelated EET should also be able to explain the redshifted emission of CaWSCP.

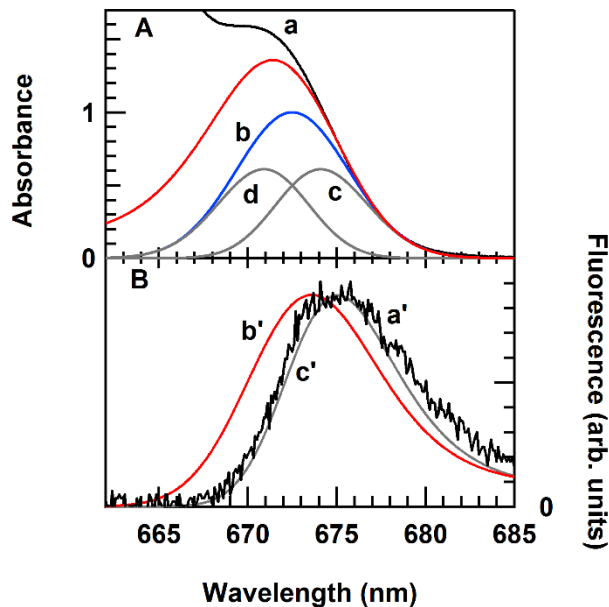


Figure 6.7 Frame A: Experimental absorption (curve a) and SDF (curve b) from Figure 7.4. The grey curves represent sub-SDFs incapable (curve c) and capable (curve d) of EET. The red curve is the low-energy absorption band calculated as the convolution of curve b with phonons. Frame B: Experimental fluorescence spectrum (curve a') compared to calculated spectra. The red curve (b') is calculated by the convolution of the whole SDF (i.e., curve b) from frame A and the single-site fluorescence spectrum from ref 165. The grey curve (c') is the convolution of the single-site spectrum with the non-EET sub-SDF (curve c) from frame A.

6.4.2. Electron Exchange

The data in Figure 6.5 indicate that ET between the Chls of the lowest energy dimer is slower than EET from high-energy dimers of the tetramer. That is, resonant excitation across the Q_y region induces the same nonresonant bleach independent of λ_B . Subsequent electron exchange could then occur between Trp and Chl, $\text{TrpChl}^- \text{Chl}^+ \rightarrow \text{Trp}^- \text{ChlChl}^+$. This would lead to a bleach

of the low-energy dimers and create additional absorption of monomeric Chl and oxidized monomer Chl (i.e., Chl⁺). It is feasible that ET from Chl⁻ to Trp could occur due to the change in oxidation potential of Chl. Similar light-induced electron exchange between tyrosine and Chl has been proposed as a quenching mechanism in the Cytochrome *b₆f* complex²⁶⁹ and ET can occur between riboflavin and Trp in riboflavin-binding proteins.²⁷⁰ For the proposed model of WSCP electron exchange, the electron is trapped as long as low temperature is maintained; that is, the reversible photochemistry occurs due to thermally activated recombination.

In order to qualitatively assess the proposed model of electron exchange, Figure 6.8 shows simulated spectra compared to experimental data. Curves a–c are the absorption, persistent HB and transient HB spectra, respectively, with corresponding simulated curves labeled as a'–c'. The blue curves 1–4 represent the absorption of exciton states of the two dimers, i.e., a lower and upper exciton component for each strongly coupled dimer within the Chl tetramer; with the sum of curves 1–4 equivalent to curve a'. Curves 1 and 2 are calculated as the convolution of the single-site fluorescence¹⁶⁵ reflected with respect to the ZPL with curves c and d from Figure 6.7, respectively. The upper exciton states (3 and 4) are assumed to be equivalent to curves 1 and 2, except shifted to higher energy and exhibiting stronger dipole strength.

To simulate the persistent and transient HB spectra, the difference between postburn and preburn spectra are taken. For persistent HB, the postburn spectrum is the summation of curves 2, 4 (representing the high-energy dimer) and the solid grey curve (corresponding to the decoupled monomer after electron exchange occurs). Note that the monomer absorption curve is scaled to a relative dipole strength of 1 Chl. The decoupled monomer site energy should be the average of lower and upper exciton energies. However, to account for the electrochromic shift induced by

Chl⁺, the decoupled monomer is shifted to higher energy. The resulting hole (curve b') qualitatively matches the experimental spectrum (curve b).

Similarly, the postburn spectrum for transient HB is simulated by the summation of curves 2, 3 and the dashed grey curve. Thus, for transient data, it is assumed that only those dimers with a very large energy gap contribute. Note that transient features are only measurable while the sample is under laser illumination; suggesting these dimers could have less efficient electron exchange than those that contribute to the persistent spectrum. Again, the decoupled monomer contribution is shifted to the blue, reflecting the proposed electrochromic shift.

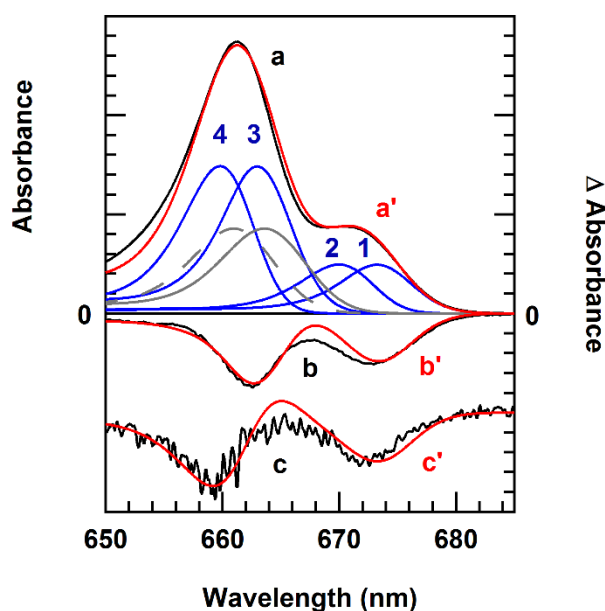


Figure 6.8 Experimental (black curves) and simulated (red curves) absorption (a/a'), and persistent (b/b') and transient (c/c') nonresonant HB spectra. Transient spectrum shifted for clarity. Curves 1–4 are the exciton states of the two Chl dimers. The solid and dashed grey curves represent the contribution of the decoupled, monomeric Chl absorption to the persistent and transient HB spectra, respectively.

6.5. Concluding Remarks

LvWSCP and CaWSCP complexes (obtained using a water-in-oil emulsion system) bind four Chls per tetramer as revealed by room-temperature absorption spectra (200–700 nm region).⁷⁰ This is consistent with the X-ray structure obtained for LvWSCP,⁴⁷ which revealed the presence of four Chls per tetramer. The absorption, emission and persistent HB spectra of LvWSCP are interpreted in terms of uncorrelated EET between two weakly interacting dimers. The shape of the ZPH action spectrum is also consistent with the above assignment and properly describes the redshifted emission peak position. Since LvWSCP and CaWSCP contain the same number of Chls per protein complex, the analysis presented in this work is valid for CaWSCP, in agreement with a very recent X-ray structure obtained for CaWSCP.⁶⁷ Therefore, we propose there is no need to include slow protein relaxation within the lowest excited state as suggested in previous analysis of CaWSCP fluorescence and HB spectra (which assumed the presence of a single Chl dimer).^{165,263,264} In addition, light-induced electron exchange between the Chls and protein has been demonstrated; providing insight into the origin of nonresonant (persistent) holes by indicating that the HB process is mostly photochemical in nature and that electrons may be trapped at low temperature by nearby aromatic amino acids. Further studies of WSCP mutants are necessary to determine the exact nature of the electron exchange (research in progress). Finally, since small differences have been observed from sample to sample in 5 K absorption and HB spectra, including spectra of dissolved CaWSCP crystals (data not shown for brevity), it remains to be established what fraction of Chl *a* could convert to Chl *a* derivative, e.g., 13²-HO-Chl *a*, during the protein reconstitution process. This is currently being tested via native electrospray mass spectrometry, as an exact composition is essential for future description of the excitonic structure and EET dynamics in these protein complexes.

Acknowledgments

This work has been supported by the Chemical Sciences, Geosciences and Biosciences Division, Office of Basic Energy Science, U.S. Department of Energy (award No. DE-SC0006678 to R.J.). We acknowledge useful discussions with Dr. Jörg Pieper (University of Tartu, Estonia).

Chapter 7

Conclusions

This work presents the application of laser-based spectroscopies, mainly spectral HB, and computer simulations towards two model pigment–protein complexes, i.e., FMO and WSCP. The two representative complexes are used to investigate the effects of structural symmetry and energy transfer on the shapes of optical spectra. By studying proteins with high-resolution crystal structures, structure-based calculations can be directly compared/contrasted with low-temperature measurements. In order to account for the presence of both strong and weak el-ph coupling, subunits are designated as excitonic domains described by a non-Markovian reduced density matrix lineshape (Redfield) approach and generalized Förster theory.

As the spectral density is key input parameter for Redfield calculations, accurate spectral density shapes are critical in order to properly describe spectral lineshapes and el-ph coupling parameters. Many functional forms used in the literature do not provide physically realistic values for S and/or E_λ . That is, at least one of two conditions is not met: the spectral density must converge to zero at zero wavenumbers or the Fourier-transformed correlation function must converge to zero as the wavenumber goes to infinity. The commonly used Ohmic and OBO spectral densities diverge at zero wavenumbers, causing S to be undefined. Additionally, care must be taken to fit experimental site-selective spectra (e.g., Δ FLN and single-complex spectra), which can reveal the homogeneous lineshape, as different photosynthetic complexes have varied PSB shapes. It is proposed that the lognormal distribution exhibits all the desired properties outlined above and is applied to several photosynthetic complexes. However, the complex form of the lognormal function does not allow for analytical solutions to integral equations. Such a limitation is minimal for spectra simulated in this work, where calculations can be performed numerically; but for more

advanced simulations of 2DES, such numerical calculations are not feasible. Therefore, further work into functional forms (potentially derived from theory) which can provide the shape and advantages of the lognormal distribution as well as analytical forms for integral equations is needed.

Experimental evidence suggests that FMO samples can contain mixtures of intact and destabilized complexes; distinguished by a shift in the 825 nm absorption band and change in HB efficiency. While the differences are slight, simulations of different spectra lead to different BChl *a* site energy assignments which introduces additional uncertainties when simultaneously modeling various spectra found in the literature. Interestingly, the Stokes shift is found to be the same for all samples, indicating that both intact and destabilized FMO complexes have weak el-ph coupling (with $E_\lambda \sim 15\text{--}20 \text{ cm}^{-1}$). Thus, only optical spectra measured on the same sample (preferably freshly prepared) can be simultaneously calculated. Considering the above comments, simulated absorption, fluorescence and HB spectra for intact FMO are presented. The resulting comparisons with experiment indicate that the entire trimer has to be taken into account in order to explain the low-energy exciton band at 825 nm. That is, while not important for femtosecond timescales, intermonomer energy transfer is present in FMO and affects the shape of fluorescence and nonresonant holes. A comprehensive comparison of simulated spectra with various optical spectra, temperature-dependent absorption and exciton population dynamics is used to elucidate a Hamiltonian for the entire FMO trimer complex. Current research is in progress to apply the trimer Hamiltonian towards complimentary time-domain spectra (i.e., pump-probe and 2DES), with the purpose of studying coherent and dissipation effects.

For WSCP, while initially investigated as a simple excitonic system (a dimer of dimers) for model calculations, the presence of nonconserved holes complicates any straight-forward

simulations. Based on nonresonant and resonant persistent HB spectra, both photochemical and nonphotochemical holes are burned. A mechanism of electron exchange is proposed to account for the PHB, where ET can occur between the lowest energy Chl *a* molecule and nearby Trp residues. HB in the absorption region of aromatic amino acids (~280 nm) is consistent with a model involving Trp. In addition, simple excitonic calculations of the low-energy state (utilizing experimental lineshape and SDF) combined with simulated absorption difference spectra can be used to qualitatively fit both persistent and transient nonresonant holes. Further measurements are necessary in order to confirm or reject the mechanism of electron exchange. Currently, a complementary study of CaWSCP is in progress utilizing both HB and transient absorption spectroscopies. Preliminary results are complicated, however, by the presence of Chl *a* derivatives (tentatively 13²-HO-Chl *a*) and a thorough pigment analysis is needed before optical spectra can be described accurately.

References

- (1) Blankenship, R. E. *Molecular Mechanisms of Photosynthesis*; Blackwell Science: Oxford, 2002.
- (2) Savikhin, S.; Jankowiak, R. Mechanism of Primary Charge Separation in Photosynthetic Reaction Centers. In *The Biophysics of Photosynthesis*; Golbeck, J., van der Est, A., Eds.; Biophysics for the Life Sciences, Volume 11; Allwell, N. M., Ed.; Springer: New York, 2014; pp 193–240.
- (3) Zazubovich, V.; Jankowiak, R. Biophotonics in Photosynthesis. In *Photonics Volume 4: Biomedical Photonics, Spectroscopy, and Microscopy*; Andrews, D. L., Ed.; Wiley: Hoboken, 2015; pp 129–164.
- (4) *Oxygenic Photosynthesis: The Light Reactions*; Ort, D. R., Yocum, C. F., Eds.; Advances in Photosynthesis, Volume 4; Govindjee, Ed.; Kluwar Academic: Dordrecht, The Netherlands, 1996.
- (5) *Photosystem II: The Light-Driven Water:Plastoquinone Oxidoreductase*; Wydrzynski, T. J., Satoh, K., Eds.; Advances in Photosynthesis and Respiration, Volume 22; Govindjee, Ed.; Springer: Dordrecht, The Netherlands, 2005.
- (6) *Photosystem I: The Light-Driven Plastocyanin:Ferredoxin Oxidoreductase*; Golbeck, J. H., Ed.; Advances in Photosynthesis and Respiration, Volume 24; Govindjee, Ed.; Springer: Dordrecht, The Netherlands, 2006.
- (7) Rémygy, H.-W.; Hauska, G.; Müller, S. A.; Tsiotis, G. The Reaction Centre from Green Sulphur Bacteria: Progress towards Structural Elucidation. *Photosynth. Res.* **2002**, *71*, 91–98.
- (8) Horton, P.; Ruban, A. Molecular Design of the Photosystem II Light-Harvesting Antenna: Photosynthesis and Photoprotection. *J. Exp. Bot.* **2005**, *56*, 365–373.
- (9) Krause, G. H.; Jahns, P.; Non-Photochemical Energy Dissipation Determined by Chlorophyll Fluorescence Quenching: Characterization and Function. In *Chlorophyll a Fluorescence: A Signature of Photosynthesis*; Papageorgeiou, G. C., Govindjee, Eds.; Advances in Photosynthesis and Respiration, Volume 19; Govindjee, Ed.; Springer: Dordrecht, The Netherlands, 2004; pp 463–495.
- (10) *Anoxygenic Photosynthetic Bacteria*; Blankenship, R. E.; Madigan, M. T., Bauer, C. E., Eds.; Advances in Photosynthesis, Volume 2; Govindjee, Ed.; Kluwar Academic: Dordrecht, The Netherlands, 1995.
- (11) Manske, A. K.; Glaeser, J.; Kuypers, M. M. M.; Overmann, J. Physiology and Phylogeny of Green Sulfur Bacteria Forming a Monospecific Phototrophic Assemblage at a Depth of 100 Meters in the Black Sea. *Appl. Environ. Microbiol.* **2005**, *71*, 8049–8060.

- (12) Beatty, J. T.; Overmann, J.; Lince, M. T.; Manske, A. K.; Lang, A. S.; Blankenship, R. E.; van Dover, C. L.; Martinson, T. A.; Plumley, F. G. An Obligately Photosynthetic Bacterial Anaerobe from a Deep-Sea Hydrothermal Vent. *Proc. Natl. Acad. Sci. U.S.A.* **2005**, *102*, 9306–9310.
- (13) Blankenship, R. E.; Olson, J. M.; Miller, M. Antenna Complexes from Green Sulfur Bacteria. In *Anoxygenic Photosynthetic Bacteria*; Blankenship, R. E., Madigan, M. T., Bauer, C. E., Eds.; Advances in Photosynthesis, Volume 2; Govindjee, Ed.; Kluwer Academic: Dordrecht, The Netherlands, 1995; pp 399–435.
- (14) Frigaard, N.-U.; Bryant, D. A. Chlorosomes: Antenna Organelles in Photosynthetic Green Bacteria. In *Complex Intracellular Structures in Prokaryotes*; Shively, J. M., Ed.; Microbiology Monographs, Volume 2; Steinbüchel, A., Ed.; Springer-Verlag: Berlin, 2006; pp 79–114.
- (15) Oostergetel, G. T.; van Amerongen, H.; Boekema, E. J. The Chlorosome: A Prototype for Efficient Light Harvesting in Photosynthesis. *Photosynth. Res.* **2010**, *104*, 245–255.
- (16) Orf, G. S.; Blankenship, R. E. Chlorosome Antenna Complexes from Green Photosynthetic Bacteria. *Photosynth. Res.* **2013**, *116*, 315–331.
- (17) Montaña, G. A.; Bowen, B. P.; LaBelle, J. T.; Woodbury, N. W.; Pizziconi, V. B.; Blankenship, R. E. Characterization of *Chlorobium tepidum* Chlorosomes: A Calculation of Bacteriochlorophyll *c* per Chlorosome and Oligomer Modeling. *Biophys. J.* **2003**, *85*, 2560–2565.
- (18) Persson, S.; Sönksen, C. P.; Frigaard, N.-U.; Cox, R. P.; Roepstorff, P.; Miller, M. Pigments and Proteins in Green Bacterial Chlorosomes Studied by Matrix-Assisted Laser Desorption Ionization Mass Spectrometry. *Eur. J. Biochem.* **2000**, *267*, 450–456.
- (19) Vassilieva, E. V.; Stirewalt, V. L.; Jakobs, C. U.; Friggard, N.-U.; Inoue-Sakamoto, K.; Baker, M. A.; Sotak, A.; Bryant, D. A. Subcellular Localization of Chlorosome Proteins in *Chlorobium tepidum* and Characterization of Three New Chlorosome Proteins: CsmF, CsmH, and CsmX. *Biochemistry* **2002**, *41*, 4358–4370.
- (20) Kouyianou, K.; de Bock, P.-J.; Müller, S. A.; Nikolaki, A.; Rizos, A.; Krzyżánek, V.; Aktoudianaki, A.; Vandekerckhove, J.; Engel, A.; Gevaert, K.; Tsiotis, G. The Chlorosome of *Chlorobaculum tepidum*: Size, Mass and Protein Composition Revealed by Electron Microscopy, Dynamic Light Scattering and Mass Spectrometry-Drive Proteomics. *Proteomics* **2011**, *11*, 2867–2880.
- (21) Nozawa, T.; Ohtomo, K.; Suzuki, M.; Nakagawa, H.; Shikama, Y.; Konami, H.; Wang, Z.-Y. Structures of Chlorosomes and Aggregated BChl *c* in *Chlorobium tepidum* from Solid State High Resolution CP/MAS ¹³C NMR. *Photosynth. Res.* **1994**, *41*, 211–223.
- (22) Balaban, T. S.; Holzwarth, A. R.; Schaffner, K. CP-MAS ¹³C-NMR Dipolar Correlation Spectroscopy of ¹³C-Enriched Chlorosomes and Isolated Bacteriochlorophyll *c* Aggregates

of *Chlorobium tepidum*: The Self-Organization of Pigments is the Main Structural Feature of Chlorosomes. *Biochemistry* **1995**, *34*, 15259–15266.

- (23) Sakuragi, Y.; Frigaard, N.-U.; Shimada, K.; Matsuura, K. Association of Bacteriochlorophyll *a* with the CsmA Protein in Chlorosomes of the Photosynthetic Green Filamentous Bacterium *Chloroflexus aurantiacus*. *Biochim. Biophys. Acta* **1999**, *1413*, 172–180.
- (24) Bryant, D. A.; Vassilieva, E. V.; Frigaard, N.-U.; Li, H. Selective Protein Extraction from *Chlorobium tepidum* Chlorosomes Using Detergents. Evidence That CsmA Forms Multimers and Binds Bacteriochlorophyll *a*. *Biochemistry* **2002**, *41*, 14403–14411.
- (25) Staehelin, L. A.; Golecki, J. R.; Drews, G. Supramolecular Organization of Chlorosomes (Chlorobium Vesicles) and of Their Membrane Attachment Sites in *Chlorobium limicola*. **1980**, *589*, 30–45.
- (26) Kell, A.; Chen, J.; Jassas, M.; Tang, J. K.-H.; Jankowiak, R. Alternative Excitonic Structure in the Baseplate (BChl *a*-CsmA Complex) of the Chlorosome from *Chlorobaculum tepidum*. *J. Phys. Chem. Lett.* **2015**, *6*, 2702–2707.
- (27) Olson, J. M.; Romano, C. A. A New Chlorophyll from Green Bacteria. *Biochim. Biophys. Acta* **1962**, *59*, 726–728.
- (28) Olson, J. M. The FMO Protein. *Photosynth. Res.* **2004**, *80*, 181–187.
- (29) Milder, M. T. W.; Brüggemann, B.; van Grondelle, R.; Herek, J. L. Revisiting the Optical Properties of the FMO Protein. *Photosynth. Res.* **2010**, *104*, 257–274.
- (30) Rémygy, H.-W.; Stalhberg, H.; Fotiadis, D.; Müller, S. A.; Wolpensinger, B.; Engel, A.; Hauska, G.; Tsiotis, G. The Reaction Center Complex from the Green Sulfur Bacterium *Chlorobium tepidum*: A Structural Analysis by Scanning Transmission Electron Microscopy. *J. Mol. Biol.* **1999**, *290*, 851–858.
- (31) He, G.; Zhang, H.; King, J. D.; Blankenship, R. E. Structural Analysis of the Homodimeric Reaction Center Complex from the Photosynthetic Green Sulfur Bacterium *Chlorobaculum tepidum*. *Biochemistry* **2014**, *53*, 4924–4930.
- (32) Tang, K.-H.; Zhu, L.; Urban, V. S.; Collins, A. M.; Biswas, P.; Blankenship, R. E. Temperature and Ionic Strength Effects on the Chlorosome Light-Harvesting Antenna Complex. *Langmuir* **2011**, *27*, 4816–4828.
- (33) Fenna, R. E.; Matthews, B. W. Chlorophyll Arrangement in a Bacteriochlorophyll Protein from *Chlorobium limicola*. *Nature* **1975**, *258*, 573–577.
- (34) Fenna, R. E.; Matthews, B. W. Structure of a Bacteriochlorophyll *a*-Protein from *Prosthecochloris aestuarii*. *Brookhaven Symp. Biol.* **1976**, *28*, 170–182.

- (35) Tronrud, D. E.; Wen, J.; Gay, L.; Blankenship, R. E. The Structural Basis for the Difference in Absorbance Spectra for the FMO Antenna Protein from Various Green Sulfur Bacteria. *Photosynth. Res.* **2009**, *100*, 79–87.
- (36) Camara-Artigas, A.; Blankenship, R. E.; Allen, J. P. The Structure of the FMO Protein from *Chlorobium tepidum* at 2.2 Å Resolution. *Photosynth. Res.* **2003**, *75*, 49–55.
- (37) Ben-Shem, A.; Frolow, F.; Nelson, N. Evolution of Photosystem I – from Symmetry through Pseudosymmetry to Asymmetry. *FEBS Lett.* **2004**, *564*, 274–280.
- (38) Larson, C. R.; Seng, C. O.; Lauman, L.; Matthies, H. J.; Wen, J.; Blankenship, R. E.; Allen, J. P. The Three-Dimensional Structure of the FMO Protein from *Pelodictyon phaeum* and the Implications for Energy Transfer. *Photosynth. Res.* **2011**, *107*, 139–150.
- (39) Tronrud, D. E.; Allen, J. P. Reinterpretation of the Electron Density at the Site of the Eighth Bacteriochlorophyll in the FMO Protein from *Pelodictyon phaeum*. *Photosynth. Res.* **2012**, *112*, 71–74.
- (40) Wen, J.; Zhang, H.; Gross, M. L.; Blankenship, R. E. Native Electrospray Mass Spectrometry Reveals the Nature and Stoichiometry of Pigments in the FMO Photosynthetic Antenna Protein. *Biochemistry* **2011**, *50*, 3502–3511.
- (41) van Amerongen, H.; Valkunas, L.; van Grondelle, R. *Photosynthetic Excitons*; World Scientific: Singapore, 2000.
- (42) Savikhin, S.; Buck, D. R.; Struve, W. S. Oscillating Anisotropies in a Bacteriochlorophyll Protein: Evidence for Quantum Beating Between Exciton Levels. *Chem. Phys.* **1997**, *223*, 303–312.
- (43) Engel, G. S.; Calhoun, T. R.; Read, E. L.; Ahn, T.-K.; Mančal, T.; Cheng, Y.-C.; Blankenship, R. E.; Fleming, G. R. Evidence for Wavelike Energy Transfer Through Quantum Coherence in Photosynthetic Systems. *Nature* **2007**, *446*, 782–786.
- (44) Panitchayangkoon, G.; Hayes, D.; Fransted, K. A.; Caram, J. R.; Harel, E.; Wen, J.; Blankenship, R. E.; Engel, G. S. Long-Lived Quantum Coherence in Photosynthetic Complexes at Physiological Temperature. *Proc. Natl. Acad. Sci. U.S.A.* **2010**, *107*, 12766–12770.
- (45) Lambert, N.; Chen, Y.-N.; Cheng, Y.-C.; Li, C.-M.; Chen, G.-Y.; Nori, F. Quantum Biology. *Nat. Phys.* **2012**, *9*, 10–18.
- (46) Renger, G.; Pieper, J.; Theiss, C.; Trostmann, I.; Paulsen, H.; Renger, T.; Eichler, H. J.; Schmitt, F.-J. Water Soluble Chlorophyll Binding Protein of Higher Plants: A Most Suitable Model System for Basic Analyses of Pigment-Pigment and Pigment-Protein Interactions in Chlorophyll Protein Complexes. *J. Plant. Physiol.* **2011**, *168*, 1462–1472.

- (47) Horigome, D.; Satoh, H.; Itoh, N.; Mitsunage, K.; Oonishi, I.; Nakagawa, A.; Uchida, A. Structural Mechanism and Photoprotective Function of Water-Soluble Chlorophyll-Binding Protein. *J. Biol. Chem.* **2007**, *282*, 6525–6531.
- (48) Itoh, R.; Itoh, S.; Sugawa, M.; Oishi, O.; Tabata, K.; Okada, M.; Nishimura, M.; Yakushiji, E. Isolation of Crystalline Water-Soluble Chlorophyll Proteins with Different Chlorophyll *a* and *b* Contents from Stems and Leaves of *Lepidium virginicum*. *Plant Cell Physiol.* **1982**, *23*, 557–560.
- (49) Yakushiji, E.; Uchino, K.; Sugimura, Y.; Shiratori, I.; Takamiya, F. Isolation of Water-Soluble Chlorophyll Protein from the Leaves of *Chenopodium album*. *Biochim. Biophys. Acta* **1963**, *75*, 293–298.
- (50) Kamimura, Y.; Mori, T.; Yamasaki, Y.; Katoh, S. Isolation, Properties and a Possible Function of a Water-Soluble Chlorophyll *a/b*-Protein from Brussels Sprouts. *Plant Cell Physiol.* **1997**, *38*, 133–138.
- (51) Shinashi, K.; Satoh, H.; Uchida, A.; Nakayama, K.; Okada, M.; Oonishi, I. Molecular Characterization of a Water-Soluble Chlorophyll Protein from Main Veins of Japanese Radish. *J. Plant Physiol.* **2000**, *157*, 255–262.
- (52) Satoh, H.; Zanma, A.; Shinashi, K. Molecular Cloning and Sequence Analysis of a Water-Soluble Chlorophyll Protein cDNA from Japanese Radish. *J. Plant Physiol.* **2002**, *159*, 325–327.
- (53) Takahashi, S.; Ono, M.; Uchida, A.; Nakayama, K.; Satoh, H. Molecular Cloning and Functional Expression of a Water-Soluble Chlorophyll-Binding Protein from Japanese Wild Radish. *J. Plant Physiol.* **2013**, *170*, 406–412.
- (54) Murata, T.; Itoh, R.; Yakushiji, E. Crystallization of Water-Soluble Chlorophyll-Proteins from *Lepidium virginicum*. *Biochim. Biophys. Acta* **1980**, *593*, 167–170.
- (55) Murata, T.; Ishikawa, C. Chemical, Physiological and Spectrophotometric Properties of Crystalline Chlorophyll-Protein Complexes from *Lepidium virginicum* L. *Biochim. Biophys. Acta* **1981**, *635*, 341–347.
- (56) Itoh, R.; Itoh, S.; Sugawa, M.; Oishi, O.; Tabata, K.; Okada, M.; Nishimura, M.; Yakushiji, E. Isolation of Crystalline Water-Soluble Chlorophyll Proteins with Different Chlorophyll *a* and *b* Contents from Stems and Leaves of *Lepidium virginicum*. *Plant Cell Physiol.* **1982**, *23*, 557–560.
- (57) Satoh, H.; Nakayama, K.; Okada, M. Molecular Cloning and Functional Expression of a Water-Soluble Chlorophyll Protein, a Putative Carrier of Chlorophyll Molecules in Cauliflower. *J. Biol. Chem.* **1998**, *273*, 30568–30575.
- (58) Reinbothe, C.; Satoh, H.; Alcaraz, J.-P.; Reinbothe, S. A Novel Role of Water-Soluble Chlorophyll Proteins in the Transitory Storage of Chlorophyllide. *Plant Physiol.* **2004**, *134*, 1355–1365.

- (59) Desclos, M.; Dubousset, L.; Etienne, P.; le Caherec, F.; Satoh, H.; Bonnefoy, J.; Ourry, A.; Avice, J.-C. A Proteomic Profiling Approach to Reveal a Novel Role of *Brassica napus* Drought 22 kD/Water-Soluble Chlorophyll-Binding Protein in Young Leaves During Nitrogen Remobilization Induced by Stressful Conditions. *Plant Physiol.* **2008**, *147*, 1830–1844.
- (60) Damaraju, S.; Schlede, S.; Eckhardt, U.; Lokstein, H.; Grimm, B. Functions of the Water-Soluble Chlorophyll-Binding Protein in Plants. *J. Plant Physiol.* **2011**, *168*, 1444–1451.
- (61) Boex-Fontvieille, E.; Rustgi, S.; von Wettstein, D.; Reinbothe, S.; Reinbothe, C. Water-Soluble Chlorophyll Protein is Involved in Herbivore Resistance Activation During Greening of *Arabidopsis thaliana*. *Proc. Natl. Acad. Sci. U.S.A.* **2015**, *112*, 7303–7308.
- (62) Satoh, H.; Uchida, A.; Nakayama, K.; Okada, M. Water-Soluble Chlorophyll Protein in Brassicaceae Plants is a Stress-Induced Chlorophyll-Binding Protein. *Plant Cell Physiol.* **2001**, *42*, 906–911.
- (63) Takahashi, S.; Yanai, H.; Nakamaru, Y.; Uchida, A.; Nakayama, K.; Satoh, H. Molecular Cloning, Characterization and Analysis of the Intracellular Localization of a Water-Soluble Chl-Binding Protein from Brussels Sprouts (*Brassica oleracea* var. *gemmifera*). *Plant Cell Physiol.* **2012**, *53*, 879–891.
- (64) Murata, T.; Toda, F.; Uchino, K.; Yakushiji, E. Water-Soluble Chlorophyll Protein of *Brassica oleracea* var. *botrys* (Cauliflower). *Biochim. Biophys. Acta* **1971**, *245*, 208–215.
- (65) Horigome, D.; Satoh, H.; Uchida, A. Purification, Crystallization and Preliminary X-Ray Analysis of a Water-Soluble Chlorophyll Protein from *Brassica oleracea* L. var. *acephala* (Kale). *Acta Crystallogr. Sect. D* **2003**, *59*, 2283–2285.
- (66) Ohtsuki, T.; Ohshima, S.; Uchida, A. Purification, Crystallization and Preliminary X-Ray Diffraction Analysis of Water-Soluble Chlorophyll-Binding Protein from *Chenopodium album*. *Acta Crystallogr. Sect. F* **2007**, *63*, 740–741.
- (67) Bednarczyk, D.; Dym, O.; Prabakar, V.; Noy, D. Fine Tuning of Chlorophyll Spectra by Protein-Induced Ring Deformation. *Angew. Chemie.*, submitted for publication, 2016.
- (68) Schmidt, K.; Fufezan, C.; Krieger-Liszaky, A.; Satoh, H.; Paulsen, H. Recombinant Water-Soluble Chlorophyll Protein from *Brassica oleracea* var. *botrys* Binds Various Chlorophyll Derivatives. *Biochemistry* **2003**, *42*, 7427–7433.
- (69) Theiss, C.; Trostmann, I.; Andree, S.; Schmitt, F.-J.; Renger, T.; Eichler, H. J.; Paulsen, H.; Renger, G. Pigment-Pigment and Pigment-Protein Interactions in Recombinant Water-Soluble Chlorophyll Proteins (WSCP) from Cauliflower. *J. Phys. Chem. B* **2007**, *111*, 13325–13335.

- (70) Bednarczyk, D.; Takashi, S.; Satoh, H.; Noy, D. Assembly of Water-Soluble Chlorophyll-Binding Protein with Native Hydrophobic Chlorophylls in Water-in-Oil Emulsions. *Biochim. Biophys. Acta* **2015**, *1847*, 307–313.
- (71) Kell, A.; Bednarczyk, D.; Acharya, K.; Chen, J.; Noy, D.; Jankowiak, R. New Insight into the Water-Soluble Chlorophyll-Binding Protein from *Lepidium virginicum*. *Photochem. Photobiol.* **2016**, DOI: 10.1111/php.12581.
- (72) Knox, R. S. *Theory of Excitons*; Solid State Physics: Advances in Research and Applications, Volume 5; Seitz, F., Turnbull, D., Eds.; Academic: New York, 1963.
- (73) Davydov, A. S. *Theory of Molecular Excitons*; Plenum: New York, 1971.
- (74) Frenkel, J. On the Transformation of Light into Heat in Solids. I *Phys. Rev.* **1931**, *37*, 17–44.
- (75) Valkunas, L.; Abramavicius, D.; Mančal, T. *Molecular Excitation Dynamics and Relaxation: Quantum Theory and Spectroscopy*; Wiley-VCH: Weinheim, 2013.
- (76) Wannier, G. The Structure of Electronic Excitation Levels in Insulating Crystals. *Phys. Rev.* **1937**, *52*, 191–197.
- (77) *The Photosynthetic Reaction Center: Volume I*; Deisenhofer, J., Norris, J. R., Eds.; Academic: San Diego, 1993.
- (78) *The Photosynthetic Reaction Center: Volume II*; Deisenhofer, J., Norris, J. R., Eds.; Academic: San Diego, 1993.
- (79) Timpmann, K.; Rätsep, M.; Hunter, C. N.; Freiberg, A. Emitting Excitonic Polaron States in Core LH1 and Peripheral LH2 Bacterial Light-Harvesting Complexes. *J. Phys. Chem. B* **2004**, *108*, 10581–10588.
- (80) Trinkunas, G.; Freiberg, A. A Disordered Polaron Model for Polarized Fluorescence Excitation Spectra of LH1 and LH2 Bacteriochlorophyll Antenna Aggregates. *J. Lumin.* **2006**, *119–120*, 105–110.
- (81) Freiberg, A.; Rätsep, M.; Timpmann, K.; Trinkunas, G. Excitonic Polarons in Quasi-One-Dimensional LH1 and LH2 Bacteriochlorophyll *a* Antenna Aggregates from Photosynthetic Bacteria: A Wavelength-Dependent Selective Spectroscopy Study. *Chem. Phys.* **2009**, *357*, 102–112.
- (82) Heitler, W.; London, F. Wechselwirkung Neutraler Atome und Homöopolare Bindung nach der Quantenmechanik. *Z. Phys.* **1927**, *44*, 455–472.
- (83) Knox, R. S. Dipole and Oscillator Strengths of Chromophores in Solution. *Photochem. Photobiol.* **2003**, *77*, 492–496.

- (84) Knox, R. S.; Spring, B. Q. Dipole Strength in the Chlorophylls. *Photochem. Photobiol.* **2003**, *77*, 497–501.
- (85) Adolphs, J.; Müh, F.; Madjet, M. E.; Renger, T. Calculation of Pigment Transition Energies in the FMO Protein. *Photosynth. Res.* **2008**, *95*, 197–209, 211.
- (86) Krueger, B. P.; Scholes, G. D.; Fleming, G. R. Calculation of Couplings and Energy-Transfer Pathways between the Pigments of LH2 by the *ab initio* Transition Density Cube Method. *J. Phys. Chem. B* **1998**, *102*, 53578–5386.
- (87) Madjet, M. E.; Abdurahman, A.; Renger, T. Intermolecular Coulomb Couplings from Ab Initio Electrostatic Potentials: Application to Optical Transitions of Strongly Coupled Pigments in Photosynthetic Antennae and Reaction Centers. *J. Phys. Chem. B* **2006**, *110*, 17268–17281.
- (88) Adolphs, J.; Müh, F.; Madjet, M. E.-A.; Schmidt am Busch, M.; Renger, T. Structure-Based Calculations of Optical Spectra of Photosystem I Suggest an Asymmetric Light-Harvesting Process. *J. Am. Chem. Soc.* **2010**, *132*, 3331–3343.
- (89) Müh, F.; Madjet, M. E.-A.; Renger, T. Structure-Based Identification of Energy Sinks in Plant Light-Harvesting Complex II. *J. Phys. Chem. B* **2010**, *114*, 13517–13535.
- (90) Dirac, P. A. M. *The Principles of Quantum Mechanics*; 4th ed.; The International Series of Monographs on Physics; Marshall, W., Wilkinson, D. H., Eds.; Oxford: London, 1958; pp 136–139.
- (91) Huang, K.; Rhys, A. Theory of Light Absorption and Non-Radiative Transition in F-Centres. *Proc. R. Soc. A* **1950**, *204*, 406–423.
- (92) Franck, J. Elementary Processes of Photochemical Reactions. *Trans. Faraday Soc.* **1926**, *21*, 536–542.
- (93) Condon, E. A Theory of Intensity Distribution in Band Systems. *Phys. Rev.* **1926**, *28*, 1182–1201.
- (94) Parson, W. W. *Modern Optical Spectroscopy*; Springer-Verlag: Berlin, 2009, pp 163–170.
- (95) Sonine, N. Y. Recherches sur les Fonctions Cylindriques et le Développement des Fonctions Coninues en Séries. *Math. Ann.* **1880**, *16*, 1–80.
- (96) Jankowiak, R.; Reppert, M.; Zazubovich, V.; Pieper, J.; Reinot, T. Site Selective and Single Complex Laser-Based Spectroscopies: A Window on Excited State Electronic Structure, Excitation Energy Transfer, and Electron-Phonon Coupling of Selected Photosynthetic Complexes. *Chem. Rev.* **2011**, *111*, 4546–4598.
- (97) Bose. Plancks Gesetz und Lichtquantenhypothese. *Z. Phys.* **1924**, *26*, 178–181.

- (98) May, V.; Kühn, O. *Charge and Energy Transfer Dynamics in Molecular Systems*; 2nd ed.; Wiley-VCH: Weinheim, 2004.
- (99) Renger, T.; Marcus, R. A. On the Relation of Protein Dynamics and Exciton Relaxation in Pigment-Protein Complexes: An Estimation of the Spectral Density and a Theory for the Calculation of Optical Spectra. *J. Chem. Phys.* **2002**, *116*, 9997–10019.
- (100) Redfield, A. G. On the Theory of Relaxation Processes. *IBM J. Res. Dev.* **1957**, *1*, 19–31.
- (101) Redfield, A. G. The Theory of Relaxation Processes. *Adv. Magn. Reson.* **1965**, *1*, 1–32.
- (102) Lax, M. The Franck-Condon Principle and Its Application to Crystals. *J. Chem. Phys.* **1952**, *20*, 1752–1760.
- (103) Kubo, R.; Toyozawa, Y. Application of the Method of Generating Function to Radiative and Non-Radiative Transitions of a Trapped Electron in a Crystal. *Prog. Theor. Phys.* **1955**, *13*, 160–182.
- (104) Garab, G.; van Amerongen, H. Linear Dichroism and Circular Dichroism in Photosynthesis Research. *Photosynth. Res.* **2009**, *101*, 135–146.
- (105) Cantor, C. R.; Schimmel, P. R. *Biophysical Chemistry Part II: Techniques for the Study of Biological Structure and Function*. W. H. Freeman: San Francisco, 1980, pp 418–421.
- (106) Houssier, C.; Sauer, K. Circular Dichroism and Magnetic Circular Dichroism of the Chlorophyll and Protochlorophyll Pigments. *J. Am. Chem. Soc.* **1970**, *92*, 779–791.
- (107) Hughes, J. L.; Razeghifard, R.; Logue, M.; Oakley, A.; Wydrzynski, T.; Krausz, E. Magneto-Optic Spectroscopy of a Protein Tetramer Binding Two Exciton-Coupled Chlorophylls. *J. Am. Chem. Soc.* **2006**, *128*, 3649–3658.
- (108) Adolphs, J.; Renger, T. How Proteins Trigger Excitation Energy Transfer in the FMO Complex of Green Sulfur Bacteria. *Biophys. J.* **2006**, *91*, 2778–2797.
- (109) Renger, T.; Marcus, R. A. Photophysical Properties of PS-2 Reaction Centers and a Discrepancy in Exciton Relaxation Times. *J. Phys. Chem. B* **2002**, *106*, 1809–1819.
- (110) Renger, T.; May, V.; Kühn, O. Ultrafast Excitation Energy Transfer Dynamics in Photosynthetic Pigment–Protein Complexes. *Phys. Rep.* **2001**, *343*, 137–254.
- (111) Förster, T. Zwischenmolekulare Energiewanderung und Fluoreszenz. *Ann. Phys. (Berlin)* **1948**, *437*, 55–75.
- (112) Förster, T. Delocalized Excitation and Excitation Transfer. In *Action of Light and Organic Crystals*; Sinanoğlu, O., Ed.; Modern Quantum Chemistry: Istanbul Lectures, Part III; Academic: New York, 1965; pp 93–137.

- (113) Chenu, A.; Scholes, G. D. Coherence in Energy Transfer and Photosynthesis. *Annu. Rev. Phys. Chem.* **2015**, *66*, 69–96.
- (114) Raszewski, G.; Renger, T. Light Harvesting in Photosystem II Core Complexes is Limited by the Transfer to the Trap: Can the Core Complex Turn into a Photoprotective Mode? *J. Am. Chem. Soc.* **2008**, *130*, 4431–4446.
- (115) Renger, T.; Holzwarth, A. R. Theory of Excitation Energy Transfer and Optical Spectra of Photosynthetic Systems. In *Biophysical Techniques in Photosynthesis: Volume II*; Aartsma, T. J., Matysik, J., Eds.; Advances in Photosynthesis and Respiration, Volume 26; Govindjee, Ed.; Springer: Dordrecht, The Netherlands, 2008; pp 421–443.
- (116) Cho, M.; Vaswani, H. M.; Brixner, T.; Stenger, J.; Fleming, G. R. Exciton Analysis in 2D Electronic Spectroscopy. *J. Phys. Chem. B* **2005**, *109*, 10542–10556.
- (117) Aartsma, T. J.; Louwe, R. J. W.; Schellenberg, P. Accumulated Photon Echo Measurements of Excited State Dynamics in Pigment-Protein Complexes. In *Biophysical Techniques in Photosynthesis*; Amesz, J., Hoff, A. J., Eds.; Advances in Photosynthesis, Volume 3; Govindjee, Ed.; Kluwer: Dordrecht, The Netherlands, 1996; pp 109–122.
- (118) Vulto, S. I. E.; Streltsov, A. M.; Aartsma, T. J. Excited State Energy Relaxation in the FMO Complexes of the Green Bacterium *Prosthecochloris aestuarii* at Low Temperatures. *J. Phys. Chem. B* **1997**, *101*, 4845–4850.
- (119) Chauvet, A.; Jankowiak, R.; Kell, A.; Picorel, R.; Savikhin, S. Does the Singlet Minus Triplet Spectrum with Major Photobleaching Band Near 680–682 nm Represent an Intact Reaction Center of Photosystem II? *J. Phys. Chem. B* **2015**, *119*, 448–455.
- (120) Cho, M. Coherent Two-Dimensional Optical Spectroscopy. *Chem. Rev.* **2008**, *108*, 1331–1418.
- (121) Abramavicius, D.; Pamieri, B.; Voronine, D. V.; Šanda, F.; Mukamel, S. Coherent Multidimensional Optical Spectroscopy of Excitons in Molecular Aggregates; Quasiparticle versus Supermolecule Perspectives. *Chem. Rev.* **2009**, *109*, 2350–2408.
- (122) Mandelstam, L.; Tamm, I. The Uncertainty Relation between Energy and Time in Non-Relativistic Quantum Mechanics. *J. Phys. (USSR)* **1945**, *9*, 249–254.
- (123) Jankowiak, R.; Small, G. J. Hole-Burning Spectroscopy and Relaxation Dynamics of Amorphous Solids at Low Temperatures. *Science* **1987**, *237*, 618–625.
- (124) Jankowiak, R.; Hayes, J. M.; Small, G. J. Spectral Hole-Burning Spectroscopy in Amorphous Molecular Solids and Proteins. *Chem. Rev.* **1993**, *93*, 1471–1502.
- (125) Jankowiak, R.; Small, G. J. Disorder-Induced Relaxation Processes in Amorphous Solids at Low Temperatures. In *Disorder Effects on Relaxational Processes: Glasses, Polymers, Proteins*; Richert, R., Blumen, A., Eds.; Springer-Verlag: Berlin, 1994; pp 425–448.

- (126) Hofmann, C.; Ketelaars, M.; Matsushita, M.; Michel, H.; Aartsma, T. J.; Köhler, J. Single-Molecule Study of the Electronic Couplings in a Circular Array of Molecules: Light-Harvesting-2 Complex from *Rhodospirillum molischianum*. *Phys. Rev. Lett.* **2003**, *90*, 013004.
- (127) Berlin, Y.; Burin, A.; Friedrich, J.; Köhler, J. Low Temperature Spectroscopy of Proteins. Part II: Experiments with Single Protein Complexes. *Phys. Life Rev.* **2007**, *4*, 64–89.
- (128) *Persistent Spectral Hole-Burning: Science and Applications*; Moerner, W. E., Ed.; Topics in Current Physics, Volume 44; Springer-Verlag: Berlin, 1988.
- (129) *Zero-Phonon Lines and Spectral Hole Burning in Spectroscopy and Photochemistry*; Sild, O., Haller, K., Eds.; Springer-Verlag: Berlin, 1988.
- (130) Rancova, O.; Jankowiak, R.; Abramavicius, D. Probing Environment Fluctuations by Two-Dimensional Electronic Spectroscopy of Molecular Systems at Temperatures below 5 K. *J. Chem. Phys.* **2015**, *142*, 212428.
- (131) Herascu, N.; Kell, A.; Acharya, K.; Jankowiak, R.; Blankenship, R. E.; Zazubovich, V. Modeling of Various Optical Spectra in the Presence of Slow Excitation Energy Transfer in Dimers and Trimers with Weak Inter-Pigment Coupling: FMO as an Example. *J. Phys. Chem. B* **2014**, *118*, 2032–2040.
- (132) Jankowiak, R.; Richert, R.; Bäessler, H. Nonexponential Hole Burning in Organic Glasses. *J. Phys. Chem.* **1985**, *89*, 4569–4574.
- (133) *Disorder Effects on Relaxational Processes: Glasses, Polymers, Proteins*. Richert, R., Blumen, A., Eds.; Springer-Verlag: Berlin, 1994.
- (134) Vrandečić, K.; Rätsep, M.; Wilk, L.; Rusevich, L.; Golub, M.; Reppert, M.; Irrgang, K.-D.; Kühlbrandt, W.; Pieper, J. Protein Dynamics Tunes Excited State Positions in Light-Harvesting Complex II. *J. Phys. Chem. B* **2015**, *119*, 3920–3930.
- (135) Meldaikis, J.; Zerlauskienė, O.; Abramavicius, D.; Valkunas, L. Manifestation of Protein Conformations in the B850 Absorption Band of Light-Harvesting Complex LH2. *Chem. Phys.* **2013**, *423*, 9–14.
- (136) Müh, F.; Madjet, M. E.; Adolphs, J.; Abdurahaman, A.; Rabenstein, B.; Ishikita, H.; Knapp, E.; Renger, T. α -Helices Direct Excitation Energy Flow in the Fenna-Matthews-Olson Protein. *Proc. Natl. Acad. Sci. U.S.A.* **2007**, *104*, 16862–16867.
- (137) Renge, I.; Muring, K. Spectral Shift Mechanisms of Chlorophylls in Liquids and Solutions. *Spectrochim. Acta A* **2013**, *102*, 301–313.
- (138) Knapp, E. Lineshapes of Molecular Aggregates. Exchange Narrowing and Intersite Correlation. *Chem. Phys.* **1984**, *85*, 73–82.

- (139) Jankowiak, R. Fundamental Aspects of Fluorescence Line-Narrowing Spectroscopy. In *Shpol'skii Spectroscopy and Other Site-Selection Methods: Applications in Environmental Analysis, Bioanalytical Chemistry, and Chemical Physics*; Gooijer, C., Ariese, F., Hofstraat, J. W., Eds.; Chemical Analysis: A Series of Monographs on Analytical Chemistry and Its Applications, Volume 156, Wiley-Interscience: New York, 2000; pp 119–145.
- (140) Reppert, M.; Naibo, V.; Jankowiak, R. Modeling Study of Non-Line-Narrowed Hole-Burned Spectra in Weakly Coupled Dimers and Multi-Chromophoric Molecular Assemblies. *Chem. Phys.* **2010**, *367*, 27–35.
- (141) Reppert, M. Modeling of Resonant Hole-Burning Spectra in Excitonically Coupled Systems: The Effects of Energy-Transfer Broadening. *J. Phys. Chem. Lett.* **2011**, *2*, 2716–2721.
- (142) Lin, C.; Reppert, M.; Feng, X.; Jankowiak, R. *J. Chem. Phys.* **2014**, *141*, 035101.
- (143) Zazubovich, V. Fluorescence Line Narrowing and Δ -FLN Spectra in the Presence of Excitation Energy Transfer between Weakly Coupled Chromophores. *J. Phys. Chem. B* **2014**, *118*, 13535–13543.
- (144) Kihara, S.; Hartzler, D. A.; Orf, G. S.; Blankenship, R. E.; Savikhin, S. The Fates of the Triplet Excitations in the Fenna–Matthews–Olson Complex. *J. Phys. Chem. B* **2015**, *119*, 5765–5772.
- (145) Hayes, J. M.; Jankowiak, R.; Small, G. J. Two-Level-System Relaxation in Amorphous Solids as Probed by Nonphotochemical Hole-Burning in Electronic Transitions. In *Persistent Spectral Hole-Burning: Science and Applications*; Moerner, W. E., Ed.; Topics in Current Physics, Volume 44; Springer-Verlag: Berlin, 1988; pp 153–202.
- (146) Hayes, J. M.; Small, G. J. Photochemical Hole Burning and Strong Electron–Phonon Coupling: Primary Donor States of Reaction Centers of Photosynthetic Bacteria. *J. Phys. Chem.* **1986**, *90*, 4928–4931.
- (147) Lee, I.-J.; Small, G. J.; Hayes, J. M. Photochemical Hole Burning of Porphine in Amorphous Matrixes. *J. Phys. Chem.* **1990**, *94*, 3376–3379.
- (148) Shu, L.; Small, G. J. On the Mechanism of Nonphotochemical Hole Burning of Optical Transitions in Amorphous Solids. *Chem. Phys.* **1990**, *141*, 447–455.
- (149) Shu, L.; Small, G. J. Mechanism of Nonphotochemical Hole Burning: Cresyl Violet in Polyvinyl Alcohol Films. *J. Opt. Soc. Am. B* **1992**, *9*, 724–732.
- (150) Hayes, J. M.; Small, G. J. Non-Photochemical Hole Burning and Impurity Site Relaxation Processes in Organic Glasses. *Chem. Phys.* **1978**, *27*, 151–157.
- (151) Hayes, J. M.; Small, G. J. Mechanisms of Non-Photochemical Hole-Burning in Organic Glasses. *Chem. Phys. Lett.* **1978**, *54*, 435–438.

- (152) Kenney, M. J.; Jankowiak, R.; Small, G. J. Dispersive Kinetics of Nonphotochemical Hole Growth for Oxazine 720 in Glycerol, Polyvinyl Alcohol and Their Deuterated Analogues. *Chem. Phys.* **1990**, *146*, 47–61.
- (153) Turukhin, A. V.; Gorokhovskiy, A. A. Determination of Quantum Efficiency of Persistent Spectral Hole Burning Using Dispersive Kinetics. *Chem. Phys. Lett.* **2000**, *317*, 109–115.
- (154) Bogner, U.; Schwarz, R. Laser-Induced Changes in the Sideband Shape of Selectively Excited Dyes in Noncrystalline Organic Solids at 1.3 K. *Phys. Rev. B* **1981**, *24*, 2846–2849.
- (155) Jankowiak, R.; Cooper, R. S.; Zamzow, D.; Small, G. J. Fluorescence Line Narrowing–Nonphotochemical Hole Burning Spectrometry: Femtomole Detection and High Selectivity for Intact DNA–PAH Adducts. *Chem. Res. Toxicol.* **1988**, *1*, 60–68.
- (156) Rätsep, M.; Freiberg, A. Resonant Emission from the B870 Exciton State and Electron – Phonon Coupling in the LH2 Antenna Chromoprotein. *Chem. Phys. Lett.* **2003**, *377*, 371–376.
- (157) Jaaniso, R. Determination of Homogeneous Spectra and the Inhomogeneous Distribution Function by Hole Burning Method. *Proc. Est. Acad. Sci. Phys. Math.* **1985**, *34*, 277.
- (158) Fünfschilling, J.; Glatz, D.; Zschokke-Gränacher, I. Hole-Burning Spectroscopy as a Tool to Eliminate Inhomogeneous Broadening. *J. Lumin.* **1986**, *36*, 85–92.
- (159) Reppert, M.; Naibo, V.; Jankowiak, R. Accurate Modeling of Fluorescence Line Narrowing Difference Spectra: Direct Measurement of the Single-Site Fluorescence Spectrum. *J. Chem. Phys.* **2010**, *133*, 014506.
- (160) Debye, P. Interferenz von Röntgenstrahlen und Wärmebewegung. *Ann. Phys. (Berlin)* **1913**, *1*, 49–92.
- (161) Waller, I. Zur Frage der Einwirkung der Wärmebewegung auf die Interferenz von Röntgenstrahlen. *Z. Phys.* **1923**, *17*, 398–408.
- (162) Renger, T.; Müh, F. Understanding Photosynthetic Light-Harvesting: A Bottom Up Theoretical Approach. *Phys. Chem. Chem. Phys.* **2013**, *15*, 3348–3371.
- (163) Rätsep, M.; Freiberg, A. Electron-Phonon and Vibronic Couplings in the FMO Bacteriochlorophyll *a* Antenna Complex Studied by Difference Fluorescence Line Narrowing. *J. Lumin.* **2007**, *127*, 251–259.
- (164) Rätsep, M.; Pieper, J.; Irrgang, K.-D.; Freiberg, A. Excitation Wavelength-Dependent Electron-Phonon and Electron-Vibrational Coupling in the CP29 Antenna Complex of Green Plants. *J. Phys. Chem. B* **2008**, *112*, 110–118.
- (165) Pieper, J.; Rätsep, M.; Trostmann, I.; Paulsen, H.; Renger, G.; Freiberg, A. Excitonic Energy Level Structure and Pigment-Protein Interactions in the Recombinant Water-

Soluble Chlorophyll Protein. I. Difference Fluorescence Line-Narrowing. *J. Phys. Chem. B* **2011**, *115*, 4042–4052.

- (166) Olbrich, C.; Strümpfer, J.; Schulten, K.; Kleinekathöfer, U. Theory and Simulation of the Environmental Effects on FMO Electronic Transitions. *J. Phys. Chem. Lett.* **2011**, *2*, 1771–1776.
- (167) Olbrich, C.; Jansen, T. L. C.; Liebers, J.; Aghtar, M.; Strümpfer, J.; Schulten, K.; Knoester, J.; Kleinekathöfer, U. From Atomistic Modeling to Excitation Transfer and Two-Dimensional Spectra of the FMO Light-Harvesting Complex. *J. Phys. Chem. B* **2011**, *115*, 8609–8621.
- (168) Shim, S.; Rebentrost, P.; Valleau, S.; Aspuru-Guzik, A. Atomistic Study of the Long-Lived Quantum Coherences in the Fenna-Matthews-Olson Complex. *Biophys. J.* **2012**, *102*, 649–660.
- (169) Valleau, S.; Eisfeld, A.; Aspuru-Guzik, A. On the Alternatives for Bath Correlators and Spectral Densities from Mixed Quantum-Classical Simulations. *J. Chem. Phys.* **2012**, *137*, 224103.
- (170) Mukamel, S. *Principles Nonlinear Optical Spectroscopy*; Oxford University Press: Oxford, 1995; pp 214–234.
- (171) Toutounji, M. M.; Small, G. J. The Underdamped Brownian Oscillator Model With Ohmic Dissipation: Applicability to Low-Temperature Optical Spectra. *J. Chem. Phys.* **2002**, *117*, 3848–3855.
- (172) Butkus, V.; Valkunas, L.; Abramavicius, D. Molecular Vibrations-Induced Quantum Beats in Two-Dimensional Electronic Spectroscopy. *J. Chem. Phys.* **2012**, *137*, 044513.
- (173) Ritschel, G.; Roden, J.; Strunz, W. T.; Eisfeld, A. An Efficient Method to Calculate Excitation Energy Transfer in Light-Harvesting Systems: Application to the Fenna-Matthews-Olson Complex. *New J. Phys.* **2011**, *13*, 113034.
- (174) Kolli, A.; O'Reilly, E. J.; Scholes, G. D.; Olaya-Castro, A. The Fundamental Role of Quantized Vibrations in Coherent Light Harvesting by Cryptophyte Algae. *J. Chem. Phys.* **2012**, *137*, 174109.
- (175) Renger, T.; Trostmann, I.; Theiss, C.; Madjet, M. E.; Richter, M.; Paulsen, H.; Eichler, H. J.; Knorr, A.; Renger, G. Refinement of a Structural Model of a Pigment-Protein Complex by Accurate Optical Line Shape Theory and Experiments. *J. Phys. Chem. B* **2007**, *111*, 10487–10501.
- (176) Renger, T.; Madjet, M. E.; Knorr, A.; Müh, F. How the Molecular Structure Determines the Flow of Excitation Energy in Plant Light-Harvesting Complex II. *J. Plant Physiol.* **2011**, *168*, 1497–1509.

- (177) Jang, S.; Silbey, R. J. Single Complex Line Shapes of the B850 Band of LH2. *J. Chem. Phys.* **2003**, *118*, 9324–9336.
- (178) Jang, S.; Newton, M. D.; Silbey, R. J. Multichromophoric Förster Resonance Energy Transfer from B800 to B850 in the Light Harvesting Complex 2: Evidence for Subtle Energetic Optimization by Purple Bacteria. *J. Phys. Chem. B* **2007**, *111*, 6807–6814.
- (179) Jang, S.; Silbey, R. J.; Junz, R.; Hofmann, C.; Köhler, J. Is There Elliptic Distortion in the Light Harvesting Complex 2 of Purple Bacteria? *J. Phys. Chem. B* **2011**, *115*, 12947–12953.
- (180) Kumar, P.; Jang, S. Emission Lineshapes of the B850 Band of the Light-Harvesting 2 (LH2) Complex in Purple Bacteria: A Second Order Time-Nonlocal Quantum Master Equation Approach. *J. Chem. Phys.* **2013**, *138*, 135101.
- (181) Jang, S.; Cao, J.; Silbey, R. J. On the Temperature Dependence of Molecular Line Shapes Due to Linearly Coupled Phonon Bands. *J. Phys. Chem. B* **2002**, *106*, 8313–8317.
- (182) Renger, T. Theory of Optical Spectra Involving Charge Transfer States: Dynamic Localization Predicts a Temperature Dependent Optical Band Shift. *Phys. Rev. Lett.* **2004**, *93*, 188101.
- (183) Kreisbeck, C.; Kramer, T. Long-Lived Electronic Coherence in Dissipative Exciton Dynamics of Light-Harvesting Complexes. *J. Phys. Chem. Lett.* **2012**, *3*, 2828–2833.
- (184) Chen, L.; Zheng, R.; Jing, Y.; Shi, Q. Simulation of the Two-Dimensional Electronic Spectra of the Fenna-Matthews-Olson Complex Using the Hierarchical Equations of Motion Method. *J. Chem. Phys.* **2011**, *134*, 194508.
- (185) Hein, B.; Kreisbeck, C.; Kramer, T.; Rodríguez, M. Modeling of Oscillations in Two-Dimensional Echo-Spectra of the Fenna-Matthews-Olson Complex. *New J. Phys.* **2012**, *14*, 023018.
- (186) Novoderezhkin, V. I.; Andrizhiyevskaya, B. G.; Dekker, J. P.; van Grondelle, R. Pathways and Timescales of Primary Charge Separation in the Photosystem II Reaction Center as Revealed by a Simultaneous Fit of Time-Resolved Fluorescence and Transient Absorption. *Biophys. J.* **2005**, *89*, 1464–1481.
- (187) Renger, T.; Klinger, A.; Steinecker, F.; Schmidt am Busch, M.; Numata, J.; Müh, F. Normal Mode Analysis of the Spectral Density of the Fenna-Matthews-Olson Light-Harvesting Protein: How the Protein Dissipates the Excess Energy of Excitons. *J. Phys. Chem. B* **2012**, *116*, 14565–14580.
- (188) Feng, X.; Kell, A.; Pieper, J.; Jankowiak, R. Modeling of the Optical Spectra of the Light-Harvesting CP29 Antenna Complex of Photosystem II – Part II. *J. Phys. Chem. B* **2013**, *117*, 6593–6602.
- (189) Renger, T.; Madjet, M. E.; Müh, F.; Trostmann, I.; Schmitt, F.-J.; Theiss, C.; Paulsen, H.; Eichler, H. J.; Knorr, A.; Renger, G. Thermally Activated Superradiance and Intersystem

Crossing in the Water-Soluble Chlorophyll Binding Protein. *J. Phys. Chem. B* **2009**, *113*, 9948–9957.

- (190) Nalbach, P.; Eckel, J.; Thorwart, M. Quantum Coherent Biomolecular Energy Transfer with Spatially Correlated Fluctuations. *New. J. Phys.* **2010**, *12*, 065043.
- (191) Mohseni, M.; Rebentrost, P.; Lloyd, S.; Aspuru-Guzik, A. Environment-Assisted Quantum Walks in Photosynthetic Energy Transfer. *J. Chem. Phys.* **2008**, *129*, 174106.
- (192) Kreisbeck, C.; Kramer, T.; Rodríguez, M.; Hein, B. High-Performance Solution of Hierarchical Equations of Motion for Studying Energy Transfer in Light-Harvesting Complexes. *J. Chem. Theory Comput.* **2011**, *7*, 2166–2174.
- (193) Abramavicius, D.; Voronine, D. V.; Mukamel, S. Unraveling Coherent Dynamics and Energy Dissipation in Photosynthetic Complexes by 2D Spectroscopy. *Biophys. J.* **2008**, *94*, 3613–3619.
- (194) Ishizaki, A.; Fleming, G. R. Theoretical Examination of Quantum Coherence in a Photosynthetic System at Physiological Temperature. *Proc. Natl. Acad. Sci. U.S.A.* **2009**, *106*, 17255–17260.
- (195) Vlaming, S. M.; Silbey, R. J. Correlated Intermolecular Coupling Fluctuations in Photosynthetic Complexes. *J. Chem. Phys.* **2012**, *136*, 055102.
- (196) Jankowiak, R. Probing Electron-Transfer Times in Photosynthetic Reaction Centers by Hole-Burning Spectroscopy. *J. Phys. Chem. Lett.* **2012**, *3*, 1684–1694.
- (197) Wen, J.; Zhang, H.; Gross, M. L.; Blankenship, R. E. Membrane Orientation of the FMO Antenna Protein from *Chlorobaculum tepidum* as Determined by Mass Spectrometry-Based Footprinting. *Proc. Natl. Acad. Sci. U.S.A.* **2009**, *106*, 6134–6139.
- (198) Wen, J.; Harada, J.; Buyle, K.; Yuan, K.; Tamiaki, H.; Oh-Oka, H.; Loomis, R. A.; Blankenship, R. E. Characterization of an FMO Variant of *Chlorobaculum tepidum* Carrying Bacteriochlorophyll *a* Esterified by Geranylgeraniol. *Biochemistry* **2010**, *49*, 5455–5463.
- (199) Feng, X.; Neupane, B.; Acharya, K.; Zazubovich, V.; Picorel, R.; Seibert, M.; Jankowiak, R. Spectroscopic Study of the CP43' Complex and the PSI-CP43' Supercomplex of the Cyanobacterium *Synechocystis* PCC 6803. *J. Phys. Chem. B* **2011**, *115*, 13339–13349.
- (200) Vulto, S. I. E.; de Baat, M. A.; Louwe, R. J. W.; Permentier, H. P.; Neef, T.; Miller, M.; van Amerongen, H.; Aartsma, T. J. Exciton Simulations of Optical Spectra of the FMO Complex from the Green Sulfur Bacterium *Chlorobium tepidum* at 6 K. *J. Phys. Chem. B* **1998**, *102*, 9577–9582.
- (201) Kell, A.; Acharya, K.; Zazubovich, V.; Jankowiak, R. On the Controversial Nature of the 825 nm Exciton Band in the FMO Protein Complex. *J. Phys. Chem. Lett.* **2014**, *5*, 1450–1456.

- (202) Olbrich, C.; Strmüpfel, J.; Schulten, K.; Kleinekathöfer, U. Quest for Spatially Correlated Fluctuations in the FMO Light-Harvesting Complex. *J. Phys. Chem. B* **2011**, *115*, 758–764.
- (203) Caycedo-Soler, F.; Chin, A. W.; Almeida, J.; Huelga, S. F.; Plenio, M. B. The Nature of the Low Energy Band of the Fenna-Matthews-Olson Complex: Vibronic Signatures. *J. Chem. Phys.* **2012**, *136*, 155102.
- (204) Francke, C.; Otte, S. C. M.; Miller, M.; Amesz, J.; Olson, J. M. Energy Transfer from Carotenoid and FMO-Protein in Subcellular Preparations from Green Sulfur Bacteria. Spectroscopic Characterization of an FMO-Reaction Center Core Complex at Low Temperature. *Photosynth. Res.* **1996**, *50*, 71–77.
- (205) Neupane, B.; Dang, N. C.; Acharya, K.; Reppert, M.; Zazubovich, V. Picorel, R.; Seibert, M.; Jankowiak, R. Insight into the Electronic Structure of the CP47 Antenna Protein Complex of Photosystem II: Hole Burning and Fluorescence Study. *J. Am. Chem. Soc.* **2010**, *132*, 4214–4229.
- (206) Hofmann, H.; Nettles, D.; Schuler, B. Single-Molecule Spectroscopy of the Unexpected Collapse of an Unfolded Protein at Low pH. *J. Chem. Phys.* **2013**, *139*, 121930.
- (207) Bina, D.; Blankenship, R. E. Chemical Oxidation of the FMO Antenna Protein from *Chlorobaculum tepidum*. *Photosynth. Res.* **2013**, *116*, 11–19.
- (208) Francke, C.; Amesz, J. Isolation and Pigment Composition of the Antenna System of Four Species of Green Sulfur Bacteria. *Photosynth. Res.* **1997**, *52*, 137–146.
- (209) Kell, A.; Feng, X.; Reppert, M.; Jankowiak, R. On the Shape of the Phonon Spectral Density in Photosynthetic Complexes. *J. Phys. Chem. B* **2013**, *117*, 7317–7323.
- (210) Johnson, S. G.; Small, G. J. Excited-State Structure and Energy-Transfer Dynamics of the Bacteriochlorophyll *a* Antenna Complex from *Prosthecochloris aestuarii*. *J. Phys. Chem.* **1991**, *95*, 471–479.
- (211) Wendling, M.; Pullerits, T.; Przyjalowski, M. A.; Vulto, S. I. E.; Aartsma, T. J.; van Grondelle, R.; van Amerongen, H. Electron–Vibrational Coupling in the Fenna–Matthews–Olson Complex of *Prosthecochloris aestuarii* Determined by Temperature-Dependent Absorption and Fluorescence Line-Narrowing Measurements. *J. Phys. Chem. B* **2000**, *104*, 5825–5831.
- (212) Pachón, L. A.; Brumer, P. Physical Basis for Long-Lived Electronic Coherence in Photosynthetic Light-Harvesting Systems. *J. Phys. Chem. Lett.* **2011**, *2*, 2728–2732.
- (213) Ritschel, G.; Roden, J.; Stunz, W. T.; Aspuru-Guzik, A.; Eisfeld, A. Absence of Quantum Oscillations and Dependence on Site Energies in Electronic Excitation Energy Transfer in the Fenna–Matthews–Olson Trimer. *J. Phys. Chem. Lett.* **2011**, *2*, 2912–2917.

- (214) Christensson, N.; Kauffmann, H. F.; Pullerits, T.; Mančal, T. Origin of Long-Lived Coherences in Light-Harvesting Complexes. *J. Phys. Chem. B* **2012**, *116*, 7449–7454.
- (215) Kreisbeck, C.; Kramer, T.; Aspuru-Guzik, A. Disentangling Electronic and Vibronic Coherences in Two-Dimensional Echo Spectra. *J. Phys. Chem. B* **2013**, *117*, 9380–9385.
- (216) Nalbach, P.; Braun, D.; Thorwart, M. Exciton Transfer Dynamics and Quantumness of Energy Transfer in the Fenna-Matthews-Olson Complex. *Phys. Rev. E* **2011**, *84*, 041926.
- (217) Sarovar, M.; Cheng, Y.-C.; Whaley, K. B. Environmental Correlation Effects on Excitation Energy Transfer in Photosynthetic Light Harvesting. *Phys. Rev. E* **2011**, *83*, 011906.
- (218) Bhattacharyya, P.; Sebastian, K. L. Adiabatic Eigenfunction-Based Approach for Coherent Excitation Transfer: An Almost Analytical Treatment of the Fenna-Matthews-Olson Complex. *Phys. Rev. E* **2013**, *87*, 062712.
- (219) Rebentrost, P.; Mohseni, M.; Aspuru-Guzik, A. Role of Quantum Coherence and Environmental Fluctuations in Chromophoric Energy Transport. *J. Phys. Chem. B* **2009**, *113*, 9942–9947.
- (220) Schmidt am Busch, M.; Müh, F.; Madjet, M. E.-A.; Renger, T. The Eighth Bacteriochlorophyll Completes the Excitation Energy Funnel in the FMO Protein. *J. Phys. Chem. Lett.* **2011**, *2*, 93–98.
- (221) Huo, P.; Coker, D. F. Iterative Linearized Density Matrix Propagation for Modeling Coherent Excitation Energy Transfer in Photosynthetic Light Harvesting. *J. Chem. Phys.* **2010**, *133*, 184108.
- (222) Wu, J.; Liu, F.; Shen, Y.; Cao, J.; Silbey, R. J. Efficient Energy Transfer in Light-Harvesting Systems, I: Optimal Temperature, Reorganization Energy and Spatial–Temporal Correlations. *New J. Phys.* **2010**, *12*, 105012.
- (223) Moix, J.; Wu, J.; Huo, P.; Coker, D.; Cao, J. Efficient Energy Transfer in Light-Harvesting Systems, III: The Influence of the Eighth Bacteriochlorophyll on the Dynamics and Efficiency in FMO. *J. Phys. Chem. Lett.* **2011**, *2*, 3045–3052.
- (224) Wu, J.; Liu, F.; Ma, J.; Silbey, R. J.; Cao, J. Efficient Energy Transfer in Light-Harvesting Systems: Quantum-Classical Comparison, Flux Network, and Robustness Analysis. *J. Chem. Phys.* **2012**, *137*, 174111.
- (225) Mostame, S.; Rebentrost, P.; Eisfeld, A.; Kerman, A. J.; Tsomokos, D. I.; Aspuru-Guzik, A. Quantum Simulator of an Open Quantum System Using Superconducting Qubits: Exciton Transport in Photosynthetic Complexes. *New J. Phys.* **2012**, *14*, 105013.
- (226) Matsuzaki, S.; Zazubovich, V.; Rätsep, M.; Hayes, J. M.; Small, G. J. Energy Transfer Kinetics and Low Energy Vibrational Structure of the Three Lowest Energy Q_y-States of the Fenna-Matthews-Olson Antenna Complex. *J. Phys. Chem. B* **2000**, *104*, 9564–9572.

- (227) Rätsep, M.; Freiberg, A. Unusual Temperature Quenching of Bacteriochlorophyll *a* Fluorescence in FMO Antenna Protein Trimers. *Chem. Phys. Lett.* **2007**, *434*, 306–311.
- (228) Savikhin, S.; Zhou, W.; Blankenship, R. E.; Struve, W. S. Femtosecond Energy Transfer and Spectral Equilibration in Bacteriochlorophyll *a*-Protein Antenna Trimers from the Green Bacterium *Chlorobium tepidum*. *Biophys. J.* **1994**, *66*, 110–114.
- (229) Savikhin, S.; Struve, W. S. Ultrafast Energy Transfer in FMO Trimers from the Green Bacterium *Chlorobium tepidum*. *Biochemistry* **1994**, *33*, 11200–11208.
- (230) Gulbinas, V.; Valkunas, L.; Kuciauskas, D.; Katilius, E.; Liuolia, V.; Zhou, W.; Blankenship, R. E. Singlet–Singlet Annihilation and Local Heating in FMO Complexes. *J. Phys. Chem.* **1996**, *100*, 17950–17956.
- (231) Louwe, R. J. W.; Aartsma, T. J. On the Nature of Energy Transfer at Low Temperatures in the BChl *a* Pigment-Protein Complex of Green Sulfur Bacteria. *J. Phys. Chem. B* **1997**, *101*, 7221–7226.
- (232) Louwe, R. J. W.; Vrieze, J.; Aartsma, T. J.; Hoff, A. J. Toward an Integral Interpretation of the Optical Steady-State Spectra of the FMO-Complex of *Prosthecochloris aestuarii*. 1. An Investigation with Linear-Dichroic Absorbance-Detected Magnetic Resonance. *J. Phys. Chem. B* **1997**, *101*, 11273–11279.
- (233) Pearlstein, R. M. Theory of the Optical Spectra of the Bacteriochlorophyll *a* Antenna Protein Trimer from *Prosthecochloris aestuarii*. *Photosynth. Res.* **1992**, *31*, 213–226.
- (234) Hayes, J. M.; Ruehlaender, M.; Soukoulis, C.; Small, G. J. Monte Carlo Simulation of Energy Transfer Rates: Application to Downward Energy Transfer within the 825 nm Absorption Band of the FMO Complex of *Prosthecochloris aestuarii*. *J. Lumin.* **2002**, *98*, 249–255.
- (235) Kell, A.; Blankenship, R. E.; Jankowiak, R. New Insight into the Fenna-Matthews-Olson Trimer Complex from *Chlorobaculum tepidum*. *J. Am. Chem. Soc.*, submitted for publication, 2016.
- (236) Schröder, M.; Kleinekathöfer, U.; Schreiber, M. Calculation of Absorption Spectra for Light-Harvesting Systems Using Markovian Approaches as Well as Modified Redfield Theory. *J. Chem. Phys.* **2006**, *124*, 084903.
- (237) Ishizaki, A.; Fleming, G. R. On the Adequacy of the Redfield Equation and Related Approaches to the Study of Quantum Dynamics in Electronic Energy Transfer. *J. Chem. Phys.* **2009**, *130*, 234110.
- (238) Ishizaki, A.; Fleming, G. R. Unified Treatment of Quantum Coherent and Incoherent Hopping Dynamics in Electronic Energy Transfer: Reduced Hierarchy Equation Approach. *J. Chem. Phys.* **2009**, *130*, 234111.

- (239) Novoderezhkin, V. I.; van Grondelle, R. Physical Origins and Models of Energy Transfer in Photosynthetic Light-Harvesting. *Phys. Chem. Chem. Phys.* **2010**, *12*, 7352–7365.
- (240) Kell, A.; Acharya, K.; Blankenship, R. E.; Jankowiak, R. On Destabilization of the Fenna-Matthews-Olson Complex of *Chlorobaculum tepidum*. *Photosynth. Res.* **2014**, *120*, 323–329.
- (241) Grozdanov, D.; Herascu, N.; Reinot, T.; Jankowiak, R.; Zazubovich, V. Low-Temperature Protein Dynamics of the B800 Molecules in the LH2 Light-Harvesting Complex: Spectral Hole Burning Study and Comparison with Single Photosynthetic Complex Spectroscopy. *J. Phys. Chem. B* **2010**, *114*, 3426–3438.
- (242) Hofmann, C.; Aartsma, T. J.; Michel, H.; Köhler, J. Direct Observation of Tiers in the Energy Landscape of a Chromoprotein: A Single-Molecule Study. *Proc. Natl. Acad. Sci. U.S.A.* **2003**, *100*, 15534–15538.
- (243) Rätsep, M.; Blankenship, R. E.; Small, G. J. Energy Transfer and Spectral Dynamics of the Three Lowest Energy Q_y -States of the Fenna-Matthews-Olson Antenna Complex. *J. Phys. Chem. B* **1999**, *103*, 5736–5741.
- (244) Freiberg, A.; Lin, S.; Timpmann, K.; Blankenship, R. E. Exciton Dynamics in FMO Bacteriochlorophyll Protein at Low Temperatures. *J. Phys. Chem. B* **1997**, *101*, 7211–7220.
- (245) MacGowan, S. A.; Senge, M. O. Contribution of Bacteriochlorophyll Conformation to the Distribution of Site-Energies in the FMO Protein. *Biochim. Biophys. Acta* **2016**, *1857*, 427–442.
- (246) Anda, A.; Hansen, T.; de Vico, L. Multireference Excitation Energies for Bacteriochlorophylls A within Light Harvesting System 2. *J. Chem. Theory Comput.* **2016**, *12*, 1305–1313.
- (247) Xu, J.; Zhang, H.-D.; Xu, R.-X.; Yan, Y. J. Correlated Driving and Dissipation in Two-Dimensional Spectroscopy. *J. Chem. Phys.* **2013**, *138*, 024106.
- (248) Sharp, L. Z.; Egorova, D.; Domcke, W. Efficient and Accurate Simulations of Two-Dimensional Electronic Photon-Echo Signals: Illustration for a Simple Model of the Fenna-Matthews-Olson Complex. *J. Chem. Phys.* **2010**, *132*, 014501.
- (249) Liang, X.-T. Simulating Signatures of Two-Dimensional Electronic Spectra of the Fenna-Matthews-Olson Complex: By Using a Numerical Path Integral. *J. Chem. Phys.* **2014**, *141*, 044116.
- (250) Nelder, J. A.; Mead, R. A Simplex Method for Function Minimization. *Comput. J.* **1965**, *7*, 308–313.

- (251) Olson, J. M.; Ke, B.; Thompson, K. H. Exciton Interaction Among Chlorophyll Molecules in Bacteriochlorophyll *a* Proteins and Bacteriochlorophyll *a* Reaction Center Complexes from Green Bacteria. *Biochim. Biophys. Acta* **1976**, *430*, 524–537, 763.
- (252) Reinot, T.; Chen, J.; Kell, A.; Robben, K. C.; Jassas, M.; Zazubovich, V.; Jankowiak, R. On the Conflicting Estimations of Pigment Site Energies in Photosynthetic Complexes: A Case Study of the CP47 Complex. *Anal. Chem. Insights*, submitted for publication, 2016.
- (253) Orf, G. S.; Niedzwiedzki, D. M.; Blankenship, R. E. Intensity Dependence of the Excited State Lifetimes and Triplet Conversion Yield in the Fenna–Matthews–Olson Antenna Protein. *J. Phys. Chem. B* **2014**, *118*, 2058–2069.
- (254) Savikhin, S.; Buck, D. R.; Struve, W. S. Toward Level-to-Level Energy Transfers in Photosynthesis: The Fenna–Matthews–Olson Protein. *J. Phys. Chem. B* **1998**, *102*, 5556–5565.
- (255) Vulto, S. I. E.; Neerken, S.; Louwe, R. J. W.; de Baat, M. A.; Amesz, J.; Aartsma, T. J. Excited-State Structure and Dynamics in FMO Antenna Complexes from Photosynthetic Green Sulfur Bacteria. *J. Phys. Chem. B* **1998**, *102*, 10630–10635.
- (256) Angell, C. A. Liquid Fragility and the Glass Transition in Water and Aqueous Solutions. *Chem. Rev.* **2002**, *102*, 2627–2649.
- (257) Ringe, D.; Petsko, G. A. The ‘Glass Transition’ in Protein Dynamics: What It Is, Why It Occurs, and How to Exploit It. *Biophys. Chem.* **2003**, *105*, 667–680.
- (258) Huh, J.; Saikin, S. K.; Brookes, J. C.; Valleau, S.; Fujita, T.; Aspuru-Guzik, A. Atomistic Study of Energy Funneling in the Light-Harvesting Complex of Green Sulfur Bacteria. *J. Am. Chem. Soc.* **2014**, *136*, 2048–2057.
- (259) He, G.; Niedzwiedzki, D. M.; Orf, G. S.; Zhang, H.; Blankenship, R. E. Dynamics of Energy and Electron Transfer in the FMO-Reaction Center Core Complex from the Phototrophic Green Sulfur Bacterium *Chlorobaculum tepidum*. *J. Phys. Chem. B* **2015**, *119*, 8321–8329.
- (260) Pšenčík, J.; Polívka, T.; Němec, P.; Dian, J.; Kudrna, J.; Malý, P.; Hála, J. Fast Energy Transfer and Exciton Dynamics in Chlorosomes of the Green Sulfur Bacterium *Chlorobium tepidum*. *J. Phys. Chem. A* **1998**, *102*, 4392–4398.
- (261) Rivera, E.; Montemayor, D.; Masia, M.; Coker, D. F. Influence of Site-Dependent Pigment–Protein Interactions on Excitation Energy Transfer in Photosynthetic Light Harvesting. *J. Phys. Chem. B* **2013**, *117*, 5510–5521.
- (262) Chandrasekaran, S.; Aghtar, M.; Valleau, S.; Aspuru-Guzik, A.; Keinekathöfer, U. Influence of Force Fields and Quantum Chemistry Approach on Spectral Densities of BChl *a* in Solution and in FMO Proteins. *J. Phys. Chem. B* **2015**, *119*, 9995–10004.

- (263) Schmitt, F.-J.; Trostmann, I.; Theiss, C.; Pieper, J.; Renger, T.; Fuesers, J.; Hubrich, E. H.; Paulsen, H.; Eichler, H. J.; Renger, G. Excited State Dynamics in Recombinant Water-Soluble Chlorophyll Proteins (WSCP) from Cauliflower Investigated by Transient Fluorescence Spectroscopy. *J. Phys. Chem. B* **2008**, *112*, 13951–13961.
- (264) Pieper, J.; Rätsep, M.; Trostmann, I.; Schmitt, F.-J.; Theiss, C.; Paulsen, H.; Eichler, H. J.; Freiberg, A.; Renger, G. Excitonic Energy Level Structure and Pigment-Protein Interactions in the Recombinant Water-Soluble Chlorophyll Protein. II. Spectral Hole-Burning Experiments. *J. Phys. Chem. B* **2011**, *115*, 4053–4065.
- (265) Murata, T.; Murata, N. Water-Soluble Chlorophyll-Proteins from *Brassica nigra* and *Lepidium virginicum* L. *Carnegie Inst. Wash. Yearbook* **70**, 504–507.
- (266) Alster, J.; Lokstein, H.; Dostál, J.; Uchida, A.; Zigmantas, D. 2D Spectroscopy Study of Water-Soluble Chlorophyll-Binding Protein from *Lepidium virginicum*. *J. Phys. Chem. B* **2014**, *118*, 3524–3531.
- (267) Suendo, V.; Viridi, S. Ab Initio Calculation of UV-Vis Absorption Spectra of a Single Chlorophyll *a* Molecule: Comparison Study between RHF/CIS, TDDFT, and Semi-Empirical Methods. *ITB J. Sci.* **2012**, *44*, 93–112.
- (268) Zazubovich, V.; Jankowiak, R. On the Energy Transfer between Quasi-Degenerate States with Uncorrelated Site Distribution Functions: An Application to the CP43 Complex of Photosystem II. *J. Lumin.* **2007**, *127*, 245–250.
- (269) Dashdorj, N.; Zhang, H.; Kim, H.; Yan, J.; Cramer, W. A.; Savikhin, S. The Single Chlorophyll *a* Molecule in the Cytochrome *b₆f* Complex: Unusual Optical Properties Protect the Complex against Singlet Oxygen. *Biophys. J.* **2005**, *88*, 4178–4187.
- (270) Magata, N.; Chosrowjan, H.; Shibata, Y.; Tanaka, F.; Nishina, Y.; Shiga, K. Dynamics and Mechanisms of Ultrafast Fluorescence Quenching Reactions of Flavin Chromophores in Protein Nanospace. *J. Phys. Chem. B* **2000**, *104*, 10667–10677.
- (271) Hayes, D.; Engel, G. S. Extracting the Excitonic Hamiltonian of the Fenna-Matthews-Olson Complex Using Three-Dimensional Third-Order Electronic Spectroscopy. *Biophys. J.* **2011**, *100*, 2043–2052.
- (272) Scholes, G. D.; Curutchet, C.; Mennucci, B.; Cammi, R.; Tomasi, J. How Solvent Controls Electronic Energy Transfer and Light Harvesting. *J. Phys. Chem. B* **2007**, *111*, 6978–6982.

Appendix A

Supporting Information for “On the Shape of the Phonon Spectral Density in Photosynthetic Complexes”

A.1. Definitions

Spectral Density

$$J(\tilde{\nu}) = \sum_i s_i \delta(\tilde{\nu} - \tilde{\nu}_i) \quad (\text{A.1})$$

Anti-Symmetric Component

$$C''(\tilde{\nu}) = \tilde{\nu}^2 J(\tilde{\nu}) \quad (\text{A.2})$$

Huang-Rhys Factor

$$S = \int_0^\infty J(\tilde{\nu}) d\tilde{\nu} \quad (\text{A.3})$$

Reorganization Energy

$$E_\lambda = \int_0^\infty \tilde{\nu} J(\tilde{\nu}) d\tilde{\nu} \quad (\text{A.4})$$

Lognormal Distribution

$$J(\tilde{\nu}) = \frac{S}{\tilde{\nu} \sigma \sqrt{2\pi}} e^{-\frac{[\ln(\tilde{\nu}/\tilde{\nu}_e)]^2}{2\sigma^2}} \quad (\text{A.5})$$

A.2. Often Used Spectral Densities

Gaussian-Lorentzian

$$J(\tilde{\nu}) \propto \begin{cases} e^{-\frac{(\tilde{\nu}-\tilde{\nu}_m)^2}{2\sigma_G^2}}, & \tilde{\nu} \leq \tilde{\nu}_m \\ \frac{1}{(\tilde{\nu} - \tilde{\nu}_m)^2 + \left(\frac{\Gamma_L}{2}\right)^2}, & \tilde{\nu} \geq \tilde{\nu}_m \end{cases} \quad (\text{A.6})$$

$$\sigma_G = \frac{\Gamma_G}{2\sqrt{2 \ln 2}}$$

B777

$$J(\tilde{\nu}) = \frac{S_0}{s_1 + s_2} \sum_{i=1,2} \frac{s_i}{7! 2\tilde{\nu}_i^4} \tilde{\nu}^3 e^{-(\tilde{\nu}/\tilde{\nu}_i)^{1/2}} \quad (\text{A.7})$$

$$s_1 = 0.8, \quad s_2 = 0.5, \quad \tilde{\nu}_1 = 0.56 \text{ cm}^{-1} (0.069 \text{ meV}), \quad \tilde{\nu}_2 = 1.9 \text{ cm}^{-1} (0.24 \text{ meV})$$

Overdamped Brownian Oscillator

$$J(\tilde{\nu}) = \frac{2E_\lambda \gamma}{\pi \tilde{\nu} (\tilde{\nu}^2 + \gamma^2)} \quad (\text{A.8})$$

Sub-Ohmic ($\alpha = 1/2$)

$$J(\tilde{\nu}) = \frac{E_\lambda}{\sqrt{\pi}} \left(\frac{1}{\tilde{\nu}_c \tilde{\nu}^3} \right)^{\frac{1}{2}} e^{-\frac{\tilde{\nu}}{\tilde{\nu}_c}} \quad (\text{A.9})$$

$$S = \infty$$

$$\int_0^\infty \tilde{\nu}^2 J(\tilde{\nu}) d\tilde{\nu} = \frac{E_\lambda \tilde{\nu}_c}{2}$$

Ohmic ($\alpha = 1$)

$$J(\tilde{v}) = \frac{E_\lambda}{\tilde{v}_c \tilde{v}} e^{-\frac{\tilde{v}}{\tilde{v}_c}} \quad (\text{A.10})$$

$$S = \infty$$

$$\int_0^\infty \tilde{v}^2 J(\tilde{v}) d\tilde{v} = E_\lambda \tilde{v}_c$$

Super-Ohmic ($\alpha = 2$)

$$J(\tilde{v}) = \frac{S}{\tilde{v}_c} e^{-\frac{\tilde{v}}{\tilde{v}_c}} \quad (\text{A.11})$$

$$E_\lambda = S \tilde{v}_c$$

$$\int_0^\infty \tilde{v}^2 J(\tilde{v}) d\tilde{v} = 2S \tilde{v}_c^2$$

Super-Ohmic ($\alpha = 3$)

$$J(\tilde{v}) = \frac{S \tilde{v}}{\tilde{v}_c^2} e^{-\frac{\tilde{v}}{\tilde{v}_c}} \quad (\text{A.12})$$

$$E_\lambda = 2S \tilde{v}_c$$

$$\int_0^\infty \tilde{v}^2 J(\tilde{v}) d\tilde{v} = 6S \tilde{v}_c^2$$

Table A.1 General expressions for different curve characteristics for both $J(\tilde{\nu})$ and $C''(\tilde{\nu})$ of spectral density functions.

Type	Function	Integrated Area	E_λ	Peak Position	Amplitude at Peak Position
G-L	$J(\tilde{\nu})^a$	S	∞	$\tilde{\nu}_m$	$\frac{4S}{I_G + I_L}$
	$C''(\tilde{\nu})^b$	∞	----	$\tilde{\nu}_m + \frac{\Gamma_L^2}{4\tilde{\nu}_m}$	$\left(\frac{S}{I_G + I_L}\right) \left(\frac{16\tilde{\nu}_m^2}{\Gamma_L^2 + 4\tilde{\nu}_m^2}\right)$
B777	$J(\tilde{\nu})$	S_0	$\frac{72S_0}{s_1 + s_2} (s_1\tilde{\nu}_1 + s_2\tilde{\nu}_2)$	$36\tilde{\nu}_i$	$\frac{162S_0s_i}{35e^6\tilde{\nu}_i(s_1 + s_2)}$
	$C''(\tilde{\nu})$	$\frac{7920S_0}{s_1 + s_2} (s_1\tilde{\nu}_1^2 + s_2\tilde{\nu}_2^2)$	----	$100\tilde{\nu}_i$	$\frac{(6.25 \times 10^7)S_0s_i\tilde{\nu}_i}{63e^{10}(s_1 + s_2)}$
OBO	$J(\tilde{\nu})^c$	∞	E_λ	0	∞
	$C''(\tilde{\nu})$	∞	----	γ	$\frac{E_\lambda}{\pi}$
Ohm	$J(\tilde{\nu})^d$	S	$S\tilde{\nu}_c\Gamma(\alpha)$	$(\alpha - 2)\tilde{\nu}_c$	$\frac{S}{\tilde{\nu}_c} \left(\frac{\alpha - 2}{e}\right)^{\alpha - 2}$
	$C''(\tilde{\nu})$	$S\tilde{\nu}_c^2\Gamma(\alpha + 1)$	----	$\alpha\tilde{\nu}_c$	$S\tilde{\nu}_c \left(\frac{\alpha}{e}\right)^\alpha$
Log	$J(\tilde{\nu})$	S	$S\tilde{\nu}_c e^{\frac{\sigma^2}{2}}$	$\tilde{\nu}_c e^{-\sigma^2}$	$\frac{S}{\tilde{\nu}_c \sigma \sqrt{2\pi}} e^{\frac{\sigma^2}{2}}$
	$C''(\tilde{\nu})$	$S\tilde{\nu}_c^2 e^{2\sigma^2}$	----	$\tilde{\nu}_c e^{\sigma^2}$	$\frac{S\tilde{\nu}_c}{\sigma \sqrt{2\pi}} e^{\frac{\sigma^2}{2}}$

^a I_G and I_L are the integrated areas of the half-Gaussian and half-Lorentzian profiles, respectively.

^bEquations for peak position and amplitude of the G-L $C''(\tilde{\nu})$ could also be given in terms of σ_G (or Γ_G), but these representations are more complex and, for simplicity, are not given here.

^cThe OBO $J(\tilde{\nu})$ has no peak position, but instead is a decay curve with $J(\tilde{\nu}) \rightarrow \infty$ as $\tilde{\nu} \rightarrow 0$.

^dNon super-Ohmic $J(\tilde{\nu})$ have infinite areas and are normalized using E_λ . $\Gamma(\alpha)$ is the Gamma function.

Appendix B

Supporting Information for “Effect of Spectral Density Shapes on the Excitonic Structure and Dynamics of the Fenna-Matthews-Olson Trimer from *Chlorobaculum tepidum*”

B.1. Qualitative Fits to Literature Data

Figure B.1 shows T–S, CD and LD spectra calculated using the parameters from Table 5.1 compared to the low-temperature, experimental data.²⁰⁰ The comparisons can only provide a qualitative assessment of the simulation parameters, as the absorption spectrum of ref 200 is blueshifted compared to the absorption spectrum fitted in the main text. The implications of such shifts are described in more detail elsewhere.²⁴⁰ Even so, the main features are reproduced, although some bands are shifted. For example, the low-energy bleach in the T–S spectrum is more redshifted for the simulated curve (a'), consistent with the above-mentioned shifts of the 825 nm absorption band. Interestingly, the low-energy fits of CD and LD are much better. In order to have a more meaningful comparison, multiple spectra (i.e., absorption, fluorescence, HB, T–S, and CD) need to be measured on a single sample in a relatively short timeframe so as to prevent destabilization of the protein. However, given uncertainties in the el-ph coupling parameters of high-energy pigments, the simulated spectra in Figure B.1 fit the experimental data reasonably well.

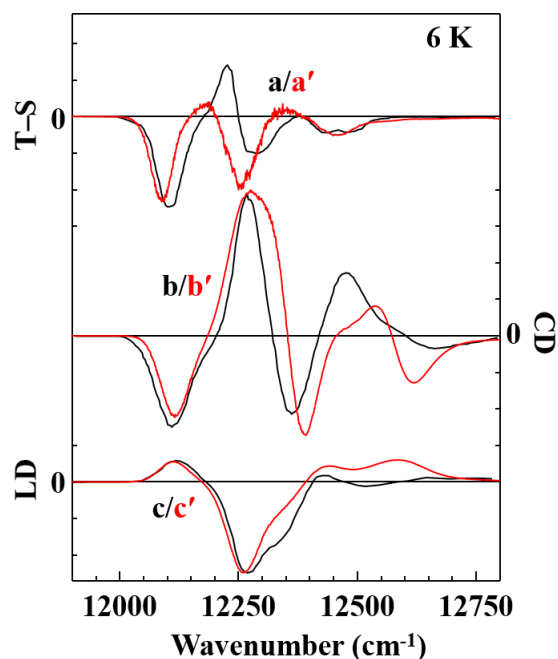


Figure B.1 6 K experimental²⁰⁰ (black) and simulated (red) T–S (a/a'), CD (b/b') and LD (c/c') spectra. Curves are simulated using parameters reported in the main text.

In addition to the low-temperature data shown in Figure B.1, low-temperature triplet energy transfer has recently been studied for FMO.^{144,253} The resulting 20 K decay associated difference spectra (DADS) LD are shown in Figure B.2, with calculated ΔA spectra for the same triplet energy transfers as reported in ref 144. That is, ΔA_3 is curve a' from Figure B.1, while $\Delta A_{i \rightarrow 3} = \Delta A_i - \Delta A_3$, where $i = 4, 5$ or 6 corresponds to the calculated bleach assuming BChl a i is in the triplet state. As with the T–S spectrum of ref 200, the low-energy bleach of the simulated ΔA_3 spectrum is redshifted compared to experiment (see red dots), reflecting different spectral positions of the 825 nm absorption band. Overall the simulated ΔA curves using the parameters of this work agree with the conclusions of ref 144; mainly, simulated bleaching due to triplet energy transfer along the BChl a $5/6 \rightarrow 4 \rightarrow 3$ pathway is consistent with experimental DADS.

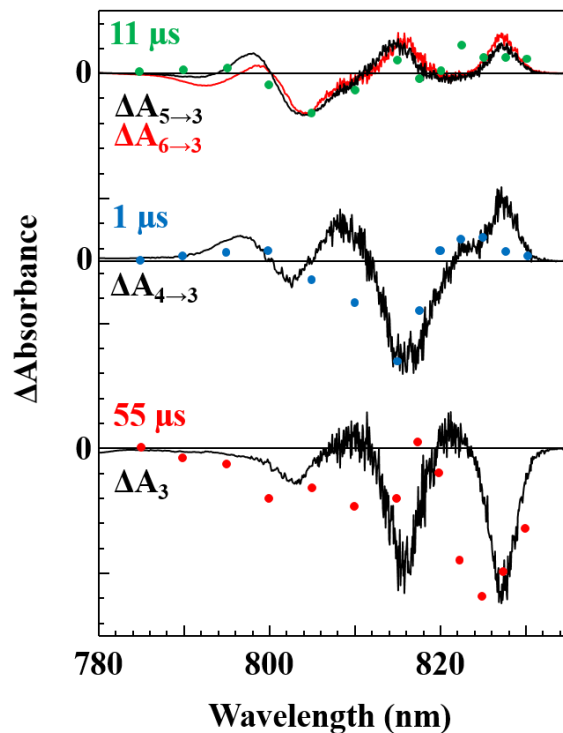


Figure B.2 Calculated ΔA spectra (solid lines) assuming the triplet state resides on various BChl *a* compared to experimental DADS (data points).¹⁴⁴ ΔA_3 corresponds to the long-lived T–S spectrum, while $\Delta A_{i \rightarrow 3}$ is the bleach resulting from triplet energy transfer from BChl *a* *i* to BChl *a* 3.

B.2. Different Models of Static and Dynamic Disorder

As mentioned in the main text, two additional models of static and dynamic disorder were used to simulate the experimental low-temperature data (parameters not shown for brevity). Figure B.3 shows a model with site-independent el-ph coupling and site-dependent inhomogeneous broadening. That is, the same lognormal spectral density ($\tilde{\nu}_c = 38 \text{ cm}^{-1}$, $\sigma = 0.7$, $S = 0.3$) is used for all pigments, while the FWHM of the site-distribution functions can vary. The simulated spectra are presented in frame A of Figure B.3, with frame B showing the corresponding occupation probabilities over 5 ps (initial excitation probabilities normalized to unity). While the simulated absorption, fluorescence and nonresonant HB spectra fit the experimental curves well (frame A), clearly the resulting population dynamics are not consistent with time-resolved

spectra,^{244,254,255} where the excitation energy is mostly located on the lowest energy exciton state within 2–10 ps. The latter indicates that the weak el-ph coupling determined experimentally for the lowest exciton state (mainly localized on BChl *a* 3) is not applicable to all higher energy states; as the slow dynamics are due to the narrow spectral density, which determines what phonon modes are available to participate in energy transfer. That is, stronger el-ph coupling is a necessary condition in order to properly describe the exciton population dynamics of FMO.

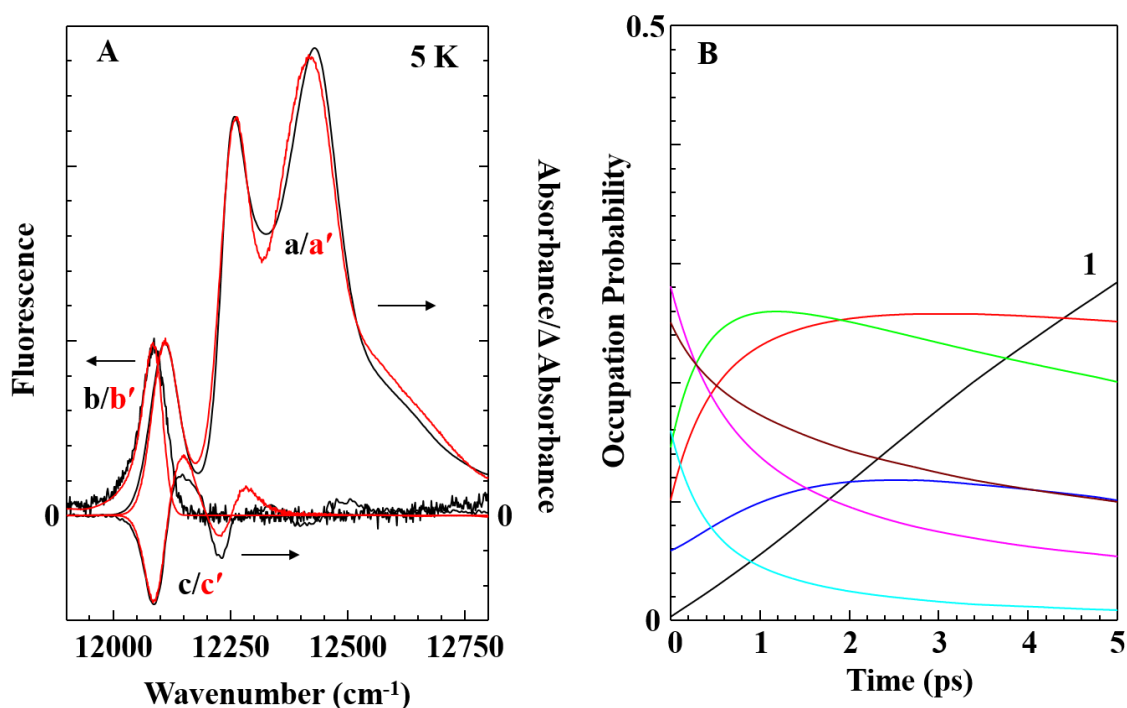


Figure B.3 Frame A: FMO trimer simulated spectra (red) compared to experiment (black).²⁴⁰ Spectra are simulated assuming the spectral density is site-independent, while inhomogeneous width varies for each site. Frame B: Exciton populations for the first 5 ps after excitation by a 50 fs laser pulse at 12 626 cm⁻¹. The lowest energy exciton state is indicated as state 1.

Due to the issues presented in Figure B.3, the experimental data were again fit using Redfield theory, only with the high-energy pigments (i.e., all but BChl *a* 3) having strong el-ph coupling ($S = 2.2$). The fits are shown in Figure B.4, and for simplicity all pigments have the same inhomogeneous broadening (FWHM = 75 cm⁻¹). The presence of stronger el-ph coupling increases

the exciton relaxation rates more similar to experimental data than Figure B.3 (data not shown). However, the increased S value enhances the temperature-dependent broadening of the absorption spectrum (Figure B.4). While the experimental spectra show only small temperature effects (even at 150 K the three bands can still be somewhat resolved), the simulated curves change more noticeably at higher temperatures. For example, the calculated spectrum at 50 K is similar to the experimental 150 K spectrum. Such a discrepancy indicates that FMO has weak el-ph coupling, consistent with literature data,^{108,163,211} and only a broader spectral density shape can improve exciton dynamics (see main text).

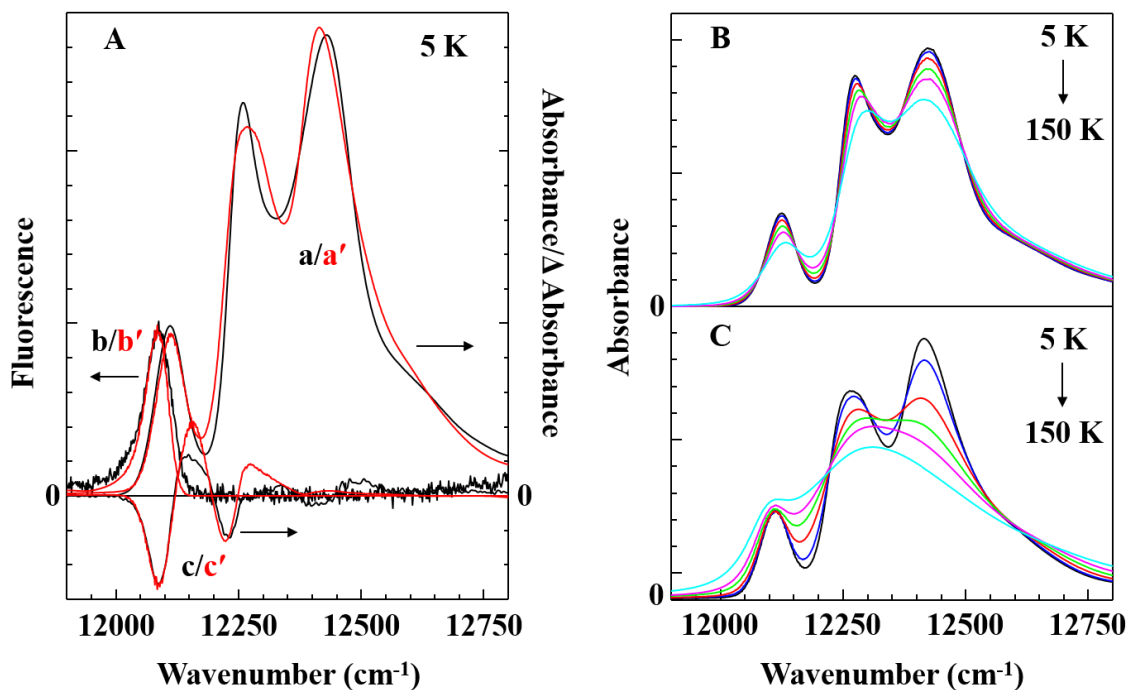


Figure B.4 Frame A: FMO trimer simulated spectra (red) compared to experiment (black).²⁴⁰ Spectra are simulated assuming the spectral density is site-dependent, while inhomogeneous width is the same for each site (75 cm⁻¹). Frame B: Experimental temperature-dependent absorption measured at 5, 25, 50, 75, 100 and 150 K. Frame C: Calculated temperature dependence using the same parameters as frame A. Calculated for 5, 25, 50, 75, 100 and 150 K.

B.3. Simulations of Optical Spectra Using Several Literature Hamiltonians

Various pigment site energy assignments have been proposed in the literature to describe linear^{108,116,200,271} and nonlinear^{116,271} optical spectra obtained for FMO complexes. In addition, different shapes of the phonon spectral density have been used^{108,116} which strongly affect the fits of optical spectra and calculated dynamics. Besides, the spectral density shapes used to model FMO spectra and dynamics in refs 108 and 116 were different from the shape extracted from experimentally measured Δ FLN spectra.^{163,209} Therefore, a straightforward comparison of parameters reported in different papers is impossible. Nevertheless, below are shown simulated absorption, fluorescence and persistent nonresonant HB spectra for several literature Hamiltonians to demonstrate that literature Hamiltonians do not satisfactorily fit the optical spectra. We anticipate that this comparison will stimulate further research to establish parameters that will describe all linear and nonlinear optical spectra including exciton relaxation and long-lived coherences.^{43,44}

When the intermonomer coupling constants (within the trimer) are set to zero, simulated absorption spectra of the FMO monomer and trimer are identical. However, for other types of optical spectra (e.g., fluorescence, nonresonant HB) the signal arises from the lowest energy state of the entire FMO trimer after intermonomer EET has occurred. This has been observed experimentally in T-S²⁰⁰ and nonresonant HB spectra.²⁰¹ Therefore, the simple exciton simulations of Vulto et al.²⁰⁰ cannot be used to simulate various optical spectra reported in the literature. This is noted in ref 200, where it was observed that the T-S bleach did not correspond to the lowest energy absorption band maximum. Thus, simulations utilizing the Hamiltonian (Table B.1) and simple model of ref 200, where dynamic disorder, exchange narrowing and intermonomer EET

were neglected, cannot be used to describe the experimental fluorescence and HB spectra presented in the main text of this work.²⁴⁰

Table B.1 Hamiltonian from simple exciton theory²⁰⁰

BChl <i>a</i>	1	2	3	4	5	6	7
1	12 400	-106	8	-5	6	-8	-4
2		12 600	28	6	2	13	1
3			12 140	-62	-1	-9	17
4				12 280	-70	-19	-57
5					12 500	94	-2
6						12 500	32
7							12 430

In ref 116, 77 K absorption and 2DES data were simulated using modified Förster/Redfield theory. The off-diagonal elements in Table B.2 are identical to Table B.1 except that a cutoff frequency of 30 cm^{-1} is introduced (that is, all electronic coupling constants less than 30 cm^{-1} were set to zero) and $V_{56} = 40 \text{ cm}^{-1}$. Coupling to the bath was described by an Ohmic spectral density^{98,209} with $E_\lambda = 35 \text{ cm}^{-1}$ and $\tilde{\nu}_c = 50 \text{ cm}^{-1}$;¹¹⁶ see also ref 209 where a critical evaluation of various shapes of phonon spectral densities was discussed.

Table B.2 Hamiltonian from Modified Redfield/Förster theory¹¹⁶

BChl <i>a</i>	1	2	3	4	5	6	7
1	12 420	-106	0	0	0	0	0
2		12 560	0	0	0	0	0
3			12 140	-62	0	0	0
4				12 315	-70	0	-57
5					12 460	40	0
6						12 500	32
7							12 400

Figure B.5 shows simulated absorption, fluorescence and persistent, nonresonant HB spectra based on the Hamiltonian presented in Table B.2 and parameters given in ref 116. In this case, in contrast to ref 200, a significantly smaller (by a factor of 1.7) static disorder was used, i.e., $\text{FWHM} = 47 \text{ cm}^{-1}$. For the HB spectrum, the postburn site energies are blueshifted by 60 cm^{-1} (see main text of this work). This shift is included to account for the likely protein energy landscape

tier. It has been shown before via single photosynthetic complex²⁴² and HB studies^{96,131,241} that in many protein complexes the protein energy landscape tiers (revealed by nonresonant HB) are on the orders of 30 to 60 cm^{-1} (these are more likely to occur) and 100 to 200 cm^{-1} (less likely). For example, we have shown that in FMO complexes shifts of about 60 cm^{-1} best describe the persistent NPHB spectra.

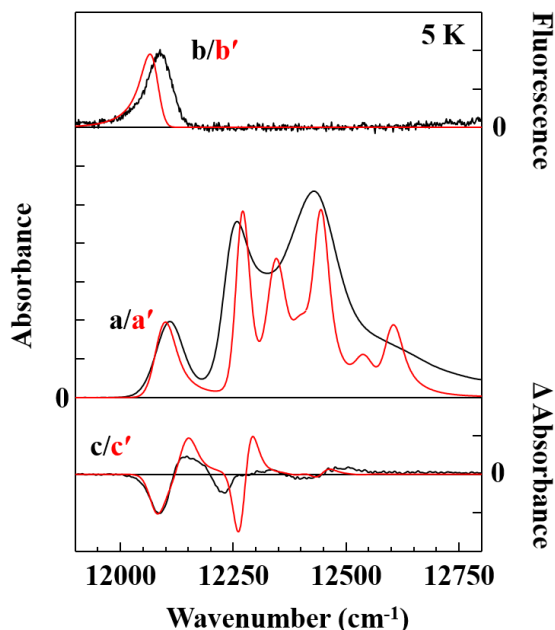


Figure B.5 5 K experimental²⁴⁰ (black) and simulated (red) absorption (a/a'), emission (b/b') and nonresonant HB (c/c') spectra. Parameters are taken from Table B.2.

While the position of the lowest energy absorption band and hole are well-fit in Figure B.5, the emission peak position is redshifted due to the large E_λ used (note that the Stokes shift is proportional to E_λ). It has been shown previously^{131,201,209,240} and in this work that $E_\lambda \sim 15 \text{ cm}^{-1}$ for the lowest energy state. Additionally, the FWHM of inhomogeneous broadening cannot describe the width of absorption bands at 5 K. For simulations at 77 K, the temperature dependence of the spectral density plays a significant role in lineshape broadening and overcomes the small static disorder and exchange narrowing; however, at 5 K the temperature-dependent terms are

negligible and the combination of a small FWHM for inhomogeneous broadening and exchange narrowing of delocalized states creates the narrow bands observed in Figure B.5. Since the lowest energy state is highly localized on BChl *a* 3, there is no apparent narrowing and the simulated width is comparable to experiment but the shapes of the simulated spectra (within Redfield theory) strongly deviate from the experimental spectra.

The Hamiltonian of Table B.3¹⁰⁸ was determined by using a non-Markovian reduced density matrix approach to Redfield theory⁹⁹ (which includes homogeneous broadening, E_λ shifts, lifetime broadening and exchange narrowing) to fit 6 K absorption, CD and LD spectra of ref 200. The site energies were free parameters which were optimized by a genetic search algorithm¹⁰⁸ for both the FMO monomer and trimer. Electronic coupling constants were calculated using the point dipole approximation with a local field factor $f = 0.8$ ($\mu_{eff} = 29.8 \text{ D}^2$). The spectral density employed was calculated from fits of 1.6 K FLN spectra of the B777 complex⁹⁹ and is compared directly to the 4 K FLN spectrum of FMO from *Pr. aestuarii* ($\lambda_{ex} = 829.2 \text{ nm}$).²¹¹ However, a more accurate comparison is to calculate FLN spectra using a specific spectral density and compare to experiment, as was done in determining the shape of the B777 spectral density,⁹⁹ or compare the calculated single-site fluorescence spectrum to an experimental Δ FLN spectrum.¹⁵⁹ $S = 0.5$ and a single vibrational mode is included at 180 cm^{-1} with $S_{vib} = 0.22$. The FWHM of static disorder is 100 cm^{-1} for all sites, which is again very different from that used in refs 116 and 200 (vide supra). Comparison to experimental 5 K spectra is shown in Figure B.6.

Table B.3 Hamiltonian from Redfield theory¹⁰⁸

BChl <i>a</i>	1	2	3	4	5	6	7
1	12 410	-87.7	5.5	-5.9	6.7	-13.7	-9.9
2		12 530	30.8	8.2	0.7	11.8	4.3
3			12 210	-53.5	-2.2	-9.6	6.0
4				12 320	-70.7	-17.0	-63.3
5					12 480	81.1	-1.3
6						12 630	39.7
7							12 440

Overall the simulated spectra of Figure B.6 are blueshifted compared to experiment. This is in agreement with ref 271, which concluded the Hamiltonian in Table B.3 had blueshifted site energies which cannot explain third-order three-dimensional electronic spectroscopy (3DES) (vide infra). One difference noticeable in the simulated absorption spectra of Figure B.6 and ref 108 (see Figure 9) is the relative intensities of the two main bands at $\sim 12\,260$ and $\sim 12\,430\text{ cm}^{-1}$. In part, this discrepancy is due to the spectral density used in calculations. The red curve in Figure B.6 is calculated using the spectral density as presented in eq 26 of ref 108; however, in the Supporting Information of ref 108 it is revealed that an approximate form (three-term super-Ohmic²⁰⁹) is used in calculations of that work in order to produce an analytical solution to integral equations. The grey curve in Figure B.6 is calculated using the super-Ohmic function reported in the Supporting Information of ref 108.

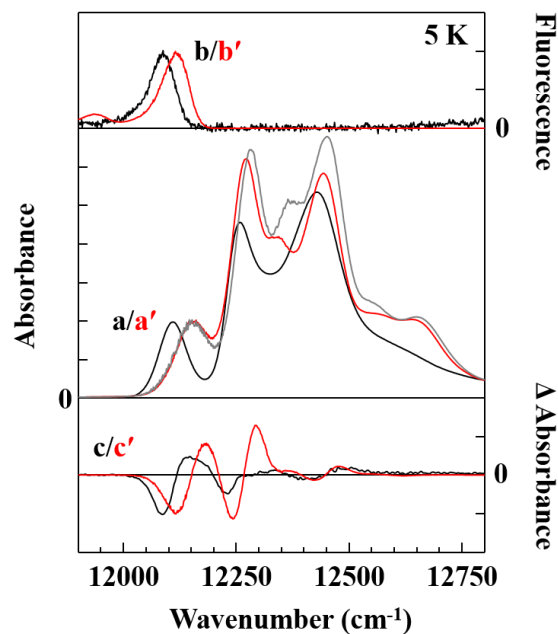


Figure B.6 5 K experimental²⁴⁰ (black) and simulated (red) absorption (a/a'), emission (b/b') and nonresonant HB (c/c') spectra. Parameters taken from Table B.3. The grey curve is the absorption spectrum calculated with the spectral density approximate function from the supporting information in ref 108.

The following section presents calculated spectra using a Hamiltonian found by fitting 77 K 3D spectra,²⁷¹ which provided Hamiltonian parameters in the excitonic representation. The site representation Hamiltonian (Table B.4) was found by applying a genetic algorithm to fit the 77 K linear absorption spectrum. Electronic coupling constants were calculated using the point dipole approximation with an exponential scaling factor $s(R_{mn})$ ²⁷² and assuming the Q_y transition dipole is rotated by 9° with respect to the y-axis of the chlorin ring.²⁷¹ Diagonal elements (site energies) were optimized by comparison to the excitonic Hamiltonian after diagonalization. In the calculated spectra of ref 271, dynamic disorder was neglected (i.e., simulation was a sum of Gaussian bands). The same value of static disorder as ref 108 (i.e., FWHM = 100 cm^{-1}) is used for all sites. Simulated spectra are shown in Figure B.7 compared to experimental data.

Table B.4 Hamiltonian from 3DES²⁷¹

BChl <i>a</i>	1	2	3	4	5	6	7
1	12 468	-53	5	-4	4	-6	-5
2		12 466	17	6	1	6	5
3			12 129	-38	-3	-7	25
4				12 410	-60	-8	-48
5					12 320	33	-8
6						12 593	38
7							12 353

Qualitatively, the shape of simulated spectra in Figure B.7 matches experiment well, especially the position of the lowest energy absorption band, emission peak and nonresonant hole. However, due to the large site energy difference between BChl *a* 3 and 4, the satellite hole at 12 227 cm^{-1} is not observed in the simulated HB spectrum. Interestingly, V_{37} in Table B.4 is ~ 20 times larger than reported in Table 5.1. Since the off-diagonal elements of both Hamiltonians are calculated from structure coordinates, the difference should be caused by rotation of the Q_y transition dipole away from the molecular *y*-axis of BChl *a* by 9° in ref 271.

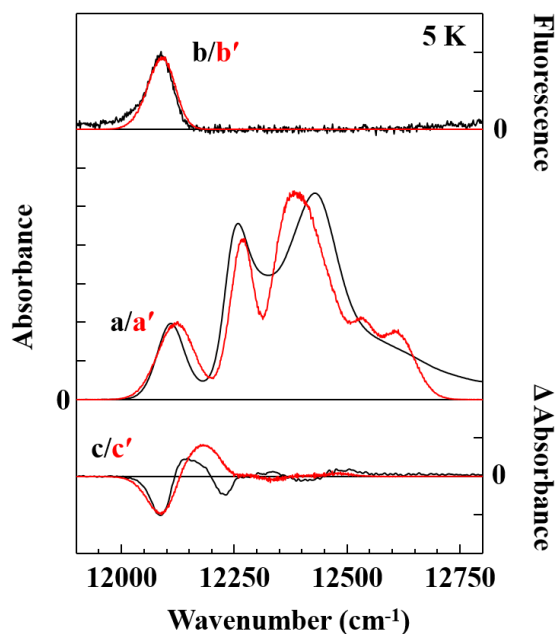


Figure B.7 5 K experimental²⁴⁰ (black) and simulated (red) absorption (a/a'), emission (b/b') and nonresonant HB (c/c') spectra. Parameters taken from Table B.4.

Clearly, the complexity of theory strongly affects the quality of simulated spectra in comparison to experimental data. The comparisons shown in Figures B.5–B.7 indicate that proper inclusion of static and dynamic disorder (established experimentally for FMO complexes) is necessary in order to provide reliable site energies for describing experimental optical spectra of FMO. In particular, the functional form of the spectral density is very important, as shown previously.²⁰⁹ Table B.5 shows the site energies for the BChl *a* pigments of FMO proposed in this work and several Hamiltonians from the literature.^{108,116,200,271} Overall the energy sets have similar trends, e.g., BChl *a* 2 has a higher site energy than BChl *a* 1. Important to notice is that only in ref 271 is BChl *a* 4 not the second lowest in energy. As seen in Figure B.7, such an assignment is inconsistent with HB data (even with larger V_{37}), which requires a smaller energy gap between BChl *a* 3 and 4 than 281 cm^{-1} as reported in column 6 of Table B.5. For additional comparisons, the experimental exciton energies from 2DES¹¹⁶ and 3DES²⁷¹ are shown in Table B.6 along with the trimer and monomer values calculated using the Hamiltonian in Table 5.1 and parameters described in Chapter 5.

Table B.5. Comparison of FMO site energies from this work and various literature Hamiltonians

BChl <i>a</i>	This work	Ref 200	Ref 116	Ref 108	Ref 271
1	12 405 (4)	12 400 (3)	12 420 (4)	12 410 (3)	12 468 (6)
2	12 505 (7)	12 600 (7)	12 560 (7)	12 530 (6)	12 466 (5)
3	12 150 (1)	12 140 (1)	12 140 (1)	12 210 (1)	12 129 (1)
4	12 300 (2)	12 280 (2)	12 315 (2)	12 320 (2)	12 410 (4)
5	12 470 (6)	12 500 (5)	12 460 (5)	12 480 (5)	12 320 (2)
6	12 575 (8)	12 500 (5)	12 500 (6)	12 630 (7)	12 593 (7)
7	12 375 (3)	12 430 (4)	12 400 (3)	12 440 (4)	12 353 (3)
8	12 430 (5)	–	–	–	–

Table B.6. Comparison of FMO exciton energies from this work and multidimensional spectroscopy

BChl <i>a</i>	Trimer (cm⁻¹)	Monomer (cm⁻¹)	2DES (cm⁻¹)¹¹⁶	3DES (cm⁻¹ ± SD)²⁷¹
1	12 085			
2	12 109		12 113	12 121 ± 15
3	12 133	12 125		
4	12 226			
5	12 252			
6	12 273	12 267	12 272	12 274 ± 20
7	12 298			
8	12 318			
9	12 336	12 338		
10	12 353		12 356	12 350 ± 16
11	12 368			
12	12 382	12 387		
13	12 397			
14	12 411		12 410	12 415 ± 12
15	12 426	12 432		
16	12 441		12 443	
17	12 457			12 454 ± 17
18	12 479	12 475		
19	12 517			12 520 ± 19
20	12 543		12 543	
21	12 565	12 557		
22	12 588			
23	12 611		12 611	12 606 ± 25
24	12 642	12 627		

Appendix C

Supporting Information for “New Insight into the Water-Soluble Chlorophyll-Binding Protein from *Lepidium virginicum*”

Table C.1 The gene sequence of LvWSCP in vector used for overexpression and synthetic gene sequence.

pETTRX–Profinity-2T–LvWSCP

```
1/1          31/11          61/21
|           |           |
ATG AGC GAT AAA ATT ATT CAC CTG ACT GAC GAC AGT TTT GAC ACG GAT GTA CTC
AAA GCG GAC GGG GCG ATC CTC GTC GAT TTC TGG GCA
M S D K I I H L T D D S F D T D V L K A D G A I L V D F W A

91/31          121/41          151/51
|           |           |
GAG TGG TGC GGT CCG TGC AAA ATG ATC GCC CCG ATT CTG GAT GAA ATC GCT GAC
GAA TAT CAG GGC AAA CTG ACC GTT GCA AAA CTG AAC
E W C G P C K M I A P I L D E I A D E Y Q G K L T V A K L N

181/61          211/71          241/81
|           |           |
ATC GAT CAA AAC CCT GGC ACT GCG CCG AAA TAT GGC ATC CGT GGT ATC CCG ACT
CTG CTG CTG TTC AAA AAC GGT GAA GTG GCG GCA ACC
I D Q N P G T A P K Y G I R G I P T L L L F K N G E V A A T

271/91          301/101          331/111
|           |           |
AAA GTG GGT GCA CTG TCT AAA GGT CAG TTG AAA GAG TTC CTC GAC GCT AAC CTG
GCC act agt ggt tct ggt cat cac cat cac cat cac
K V G A L S K G Q L K E F L D A N L A T S G S G H H H H H H

361/121          391/131          421/141
|           |           |
tcc gcg ggt GGC GGC AAA TCT AAC GGT GAG AAG AAG TAC ATT GTT GGT TTC AAG CAA
GGC TTT AAG AGC TGT GCG AAG AAA GAG GAT GTG
S A G G G K S N G E K K Y I V G F K Q G F K S C A K K E D V

451/151          481/161          511/171
|           |           |
ATC TCC GAG AAA GGT GGT AAG CTG CAG AAA TGC TTC AAA TAC GTC GAC GCG GCG
AGC GCA ACC CTG AAT GAG AAA GCA GTG GAA GAA CTG
I S E K G G K L Q K C F K Y V D A A S A T L N E K A V E E L
```

